

ACQUISITION AND TIME DELAY ESTIMATES
OF CANINE GASTRIC NERVE SIGNALS

By

JAMES JIANN-LIUH YU

A Thesis

Submitted to the School of Graduate Studies

in Partial Fulfilment of the requirements

For the Degree

Doctor of Philosophy

McMaster University



(FEBRUARY 1986)

ACQUISITION AND TIME DELAY ESTIMATES
OF CANINE GASTRIC NERVE SIGNALS

DOCTOR OF PHILOSOPHY (1986)
(Electrical and Computer Engineering)

McMASTER UNIVERSITY
Hamilton, Ontario

TITLE: Acquisition and Time Delay Estimates of Canine Gastric
Nerve signals

AUTHOR: James Jiann-Liuh Yu, B.Sc. (University of Alberta)
M.Sc. (University of Saskatchewan)

SUPERVISORS: Professor N.K. Sinha
Professor E.E. Daniel

NUMBER OF PAGES: xviii, 233

ABSTRACT

Approaches to the investigation of myogenic and hormonal controls in the mediation of gut motility are well understood, however methods to analyze neural control remain to be developed. I have developed a cannula system with nerve cuff electrodes, subserosal bipolar electrodes, and extraluminal strain gauges to simultaneously monitor the vagal nerve, myoelectric (ECA), and contractile activities in chronic dogs. The cuff electrodes were used to both stimulate and record nerve signals. Five healthy dogs were implanted with such cannula on the gastric area, with the cuff electrodes placed on the branches of the anterior nerve of Latarjet. The condition of the cuff electrodes were monitored by impedance measurements, while that of the nerves under the cuff electrodes were studied by electron microscopy (EM). Three Time Delay Estimation (TDE) algorithms: General Cross Correlation (GCC), Smooth Coherence Of Transform (SCOT), and Maximum Likelihood (ML) methods were simulated with three types of signals as inputs: Band limited Gaussian White Noise (GWN), Sine wave (SINE), and Impulses of random intervals (IMP). Results of the analysis of the recorded neural signals show that the three algorithms can be used to study the sensory and motor patterns of the compound nerve signals with the SCOT and ML methods being superior than the GCC method. The results from the EM studies suggested that the cuff electrode caused loss of the myelinated

axons and the larger diameter unmyelinated axons. Based on the results of this study, relevant physiological interpretations were also discussed.

ACKNOWLEDGEMENT

I am deeply grateful to Prof. N.K. Sinha for his guidance and support during this work. My special appreciation goes to Prof. E.E. Daniel for his advice, guidance, encouragement, and stimulating discussions, especially concerning gastrointestinal motility. His extensive knowledge and attitude towards scientific investigation has been an inspiration to me. Appreciation is also due to Dr. S.N. Reddy for suggestions concerning signal processing and support during the course of preparing this thesis.

My special thanks to Colin Wu for being always available as a good friend and for his ideas and discussions on graphic programming which is an important part of this work.

Without being exhaustive, I would like to thank the following for their support during this work: Dr. S. Sarna for his initiation of this project, Dr. L. Belbeck for his help in surgery, Dr. I. Berezin for her beautiful EM work, Drs. J. Fox and S. Collins for their advice, Mr. G. Shine for his ideas in electronic design, Mr. C. Ikeson for his help in various technical problems, and all my friends in the 4N75 Lab. for their support. In addition I would like to thank the Sullivans and McTaggarts for their friendship and prayers.

Finally, my wife, Brenda, for her endless patient, love, and prayers through out all these years, without whom I could not have completed this work.

TABLE OF CONTENTS

PAGE

ABSTRACT.....	iii
ACKNOWLEDGEMENTS.....	v
TABLE OF CONTENTS.....	vi
LIST OF ILLUSTRATIONS.....	xi
LIST OF ABBREVIATIONS.....	xviii
CHAPTER I INTRODUCTION.....	1
1.1 Introduction.....	1
1.2 Objectives of the research.....	5
1.3 Organization of the thesis.....	5
CHAPTER II REVIEW OF THE CONTROL OF THE GASTROINTESTINAL (GI) SYSTEM ..	7
2.1 Introduction.....	7
2.2 General anatomy and functions of the GI system.....	7
2.2.1 Mouth and esophagus.....	9
2.2.2 Stomach.....	9
2.2.3 Small intestine.....	11
2.2.4 Large intestine (colon).....	12
2.2.5 Rectum and anus.....	12
2.3 General principles of GI motility.....	13
2.3.1 Smooth muscle.....	13
2.3.2 Control of GI motility.....	16
2.3.2.1 Myogenic control.....	16
2.3.2.2 Hormonal control.....	18
2.3.2.3 Neural control.....	19
2.3.2.3.1 Extrinsic neural network.....	21
2.3.2.3.2 Intrinsic neural network.....	23
2.4 Methods of investigating gastric motility.....	24

TABLE OF CONTENTS

	PAGE
2.4.1 Myogenic activities.....	25
2.4.1.1 Serosal recordings.....	25
2.4.1.2 Intraluminal recordings.....	27
2.4.2 Contractile activities.....	28
2.4.2.1 Extraluminal measurements.....	28
2.4.2.2 Intraluminal pressure measurements.....	29
2.4.3 Neural activities.....	29
 CHAPTER III MATHEMATICAL BACKGROUND FOR THE ANALYSIS OF THE NEURAL SIGNAL.....	 32
3.1 Introduction.....	32
3.2 Review of the neural system.....	32
3.2.1 The neuron	33
3.2.2 Generation of nerve impulses.....	35
3.2.3 Propagation of action potentials.....	38
3.2.4 Mode of recording nerve impulses.....	39
3.2.4.1 The monophasic configuration.....	42
3.2.4.2 The biphasic configuration.....	43
3.2.4.3 The triphasic configuration.....	44
3.3 Statistical properties of neural signals.....	46
3.3.1 The action potential as a signal.....	46
3.3.2 Summed impulses as the neural signal.....	49
3.4 An approach to the analysis of nerve signals.....	51
3.5 The properties of cross-correlation.....	55
3.6 Cross-correlation algorithms.....	61
3.6.1 The General Cross-Correlation (GCC).....	62
3.6.2 The Smoothed Coherence Transform (SCOT).....	62
3.6.3 The Maximum Likelihood (ML) estimation.....	64

TABLE OF CONTENTS

	PAGE
CHAPTER IV MATERIALS AND METHODS.....	66
4.1 Introduction.....	66
4.2 Materials and methods for making various transducers.....	66
4.2.1 Nerve cuff electrode.....	66
4.2.1.1 Materials and procedures for making the cuff electrode.....	68
4.2.2 Contractile force transducer (strain gauge).....	70
4.2.2.1 Materials and procedures of making the contractile force transducer.....	70
4.2.3 Bipolar EMG electrode.....	73
4.2.3.1 Materials and procedures of making the pin electrode.....	73
4.2.4 The overall cannula system.....	75
4.3 Implantation.....	76
4.4 Instrumentation and recording.....	80
4.4.1 Impedance measurement.....	79
4.4.2 Electron microscopic studies.....	80
4.5 The computer system.....	81
4.5.1 Data acquisition	83
4.6 Considerations for discrete or digital implementation	85
4.6.1 Discrete signals analysis.....	85
4.6.2 Periodogram.....	88
4.6.3 Sampling rate and record length.....	89
4.6.4 Truncation of data	91
4.7 Procedures for analyzing the data.....	92

TABLE OF CONTENTS

	PAGE
4.7.1 Preparation of data.....	94
4.7.1.1 Simulated data.....	94
4.7.1.2 Recorded neural signals.....	95
4.7.2 Digital filtering	95
4.7.3 Subtract means.....	96
4.7.4 Normalization.....	96
4.7.5 Windowing.....	97
4.7.6 Zero padding.....	97
4.7.7 FFT computation.....	98
4.7.8 PSD computation.....	98
4.7.9 Computation of the Generalized Cross Correlation (GCC).....	99
4.7.10 Computation of the coherence function.....	99
4.7.11 Computation of the Smoothed Coherence Transformation (SCOT).....	99
4.7.12 Computation of the signal-to-noise ratio.....	100
4.7.13 Computation of the Maximum Likelihood (ML).....	100
4.8 Display of results.....	101
CHAPTER V RESULTS: SIMULATED SIGNALS	102
5.1 Introduction.....	102
5.2 Simulation details.....	102
5.3 Simulation with the Gaussian White Noise (GWN).....	104
5.4 Simulation with Sine Wave (SINE).....	115
5.5 Simulation with IMPulse (IMP).....	128
5.6 Summary:.....	141
CHAPTER VI RESULTS: NEURAL SIGNALS	142
6.1 Introduction.....	142
6.2 Typical recorded neural signals with corresponding EMG and contractile patterns?.....	143
6.2.1 Synchronization of the neural activities with EMG and contractile activities.....	143
6.2.2 Alternating firing firing patterns between adjacent nerves.....	147

TABLE OF CONTENTS

PAGE

6.3 Typical sensory and motor neural patterns.....	152
6.3.1 Patterns during active contractile periods.....	152
6.3.2 Patterns during quiescent periods.....	159
6.3.3 Cross-correlation of highly damaged nerve trunk signals.....	164
6.3.3 Cross-correlation of corrupted neural signals.....	171
6.4 Sensory and motor patterns with respect to the duration of electrode implantation.....	177
6.5 Results of stimulating the nerve of Latarjet with cuff electrode.....	182
6.6 Results of stimulating cervic vagal nerve with unitary impulses.....	187
6.7 Electron Microscopy (EM) studies.....	189
6.8 Impedance measurement of the cuff electrode.....	197
6.8.1 Impedance of average normal cuff electrodes.....	197
6.8.2 Impedance of cuff electrodes with highly damaged nerve trunks.....	198
CHAPTER VII DISCUSSIONS.....	201
7.1 Introduction.....	201
7.2 Simulation of the algorithms.....	201
7.2.1 GCC method :.....	202
7.2.2 SCOT method:.....	203
7.2.3 ML method:.....	204
7.3 Analysis of the neural signals.....	207
CHAPTER VIII CONCLUSION AND SUGGESTIONS FOR FURTHER STUDIES.....	215
8.1 Conclusions.....	215
8.2 Suggestions of further studies.....	217
8.2.1 Improvement in data acquisition.....	217
8.2.2 Physiological significance.....	219

TABLE OF CONTENTS

	PAGE
REFERENCES.....	221
APPENDIX A Procedure for the preparation of stimulating the cervical nerve.....	229
APPENDIX B Circuit diagram for a low noise pre-amplifier	231
APPENDIX C Circuit diagram for a analog multiplexer and demultiplexer.....	232

LIST OF ILLUSTRATIONS

FIGURE		PAGE
2.1	Gastrointestinal tract of a dog.....	9
2.2a	Muscle layers of the GI tract.....	15
2.2b	Smooth muscle layers of the stomach.....	15
2.3	Typical relationship among ECA, ERA, and the stomach contractile activities of the antrum region.....	18
2.4	Simplified block diagram of the organization of the extrinsic and intrinsic neural network.....	21
2.5	Some interconnections between the intrinsic and extrinsic nerves.....	24
2.6	Pin and wire electrode for the myogenic activities.....	26
3.1	Basic structure of a myelinated neuron.....	34
3.2	A typical neural action potential.....	38
3.3a-c	Typical wave shape from three different extracellular recording configurations: (a) monophasic, (b) biphasic, and (c) triphasic.....	42
3.4a	The Dirac impulse function.....	47
3.4b	A train of impulses.....	47
3.5a	A simplified nerve cuff electrode.....	52
3.5b	A equivalent signal flow diagram for Fig. 3.5a.....	52
3.6	A typical cross-correlation function of $x(t)$ and $y(t)$	58
3.7	The pre-filtered cross-correlator.....	59
4.1a-b	Diagram of the nerve cuff electrode (a) Sideview of the neural cuff electrode, (b) Cross-sectional view of the electrode.....	64

LIST OF ILLUSTRATIONS

FIGURE	PAGE
4.2 Structure of the contractile force transducer (strain gauge).....	71
4.3 Diagram of the pin EMG electrode.....	74
4.4 Location of the implanting site of the various electrodes.....	77
4.5 The block diagram of the recording instrumentation for this study.....	79
4.6 The computer system for the acquisition and analysis of neural signals.....	82
4.7 Flow diagram for the data sampling program.....	85
4.8 Procedures for analyzing the recorded neural signals.....	93
5.1 The average estimated cross-correlation peak values using the three estimation algorithms: GCC, SCOT, and ML with GWN as the inputs.....	106
5.2 The standard deviation of the estimated cross-correlation function using the three estimation algorithms: GCC, SCOT, and ML with GWN as the input.....	107
5.3 The average deviation of the estimated peak locations from the actual peak location with GWN as the input data.....	108
5.4a,b The estimated cross-correlation as a function of number of lags and SNRs obtained from the GCC method with GWN as the input data.....	109
5.5a,b The estimated cross-correlation as a function of number of lags and SNRs obtained from the SCOT method with GWN as the input data.....	111
5.6a,b The estimated cross-correlation as a function of number of lags and SNRs obtained from the ML method with GWN as the input data.....	113

LIST OF ILLUSTRATIONS

FIGURE	PAGE
5.7	Waveshape of the sinewave data sequences of 1.5K Hz corrupted with GWN data sequence with a SNR of 0 db.....117
5.8	The power spectrum density (PSD) of the waveform shown in Fig 5.7. The peak in the PSD at 1.5K Hz corresponds to the sinewave frequency.....118
5.9	The average estimated cross-correlation peak values using the three algorithms with SINE wave as inputs.....119
5.10	The standard deviation of the estimated cross-correlation function using the three estimation algorithms: GCC, SCOT, and ML with SINE wave as the inputs.....120
5.11	The average deviation of the estimated peak locations from the actual peak location.....121
5.12a,b	The estimated cross-correlation as a function of number of lags and SNRs obtained from the GCC method with SINEwave as the input data.....122
5.13a,b	The estimated cross-correlation as a function of number of lags and SNRs obtained from the SCOT method with SINE as the input data.....124
5.14a,b	The estimated cross-correlation as a function of number of lags and SNRs obtained from the ML method with GWN as the input data.....126
5.15	Waveshape of the impulse data sequences corrupted with GWN data sequence with a SNR of 0 dB.....130
5.16	The power spectrum density (PSD) of the impulse data sequences corrupted with GWN data sequence shown in Fig 5.15.....131
5.17	The average estimated cross-correlation peak values using the three algorithms: GCC, SCOT, and ML with IMPulse as inputs.....132

LIST OF ILLUSTRATIONS

FIGURE	PAGE
5.18	The standard deviation of the estimated cross-correlation function using the three estimation algorithms: GCC, SCOT, and ML with IMPulse as the inputs.....133
5.19	The average deviation of the estimated peak locations from the actual peak location, with IMPulse as the inputs.....134
5.20a,b	The estimated cross-correlation as a function of number of lags and SNRs obtained from the GCC method with IMPulse as the input data.....135
5.21a,b	The estimated cross-correlation as a function of number of lags and SNRs obtained from the SCOT method with GWN as the input data.....137
5.22a,b	The estimated cross-correlation as a function of number of lags and SNRs obtained from the ML method with GWN as the input data.....139
6.1	An example of scychronization of neural activities with the corresponding EMG and contractile activities of the corpus (E4,S4), the antrum (E3,E2,S2) and the duodenum (E1,S1).....145
6.2	An example of a long duration alternating firing patterns between N1 and N2 shown with the EMG and the contractile patterns of the corpus (E4,S4) and the antrum (E2,S2) areas.....148
6.3	An example of the short duration type of alternating neural firing pattern.....150
6.4	Cross-correlation between two channels (N21,N22) of the recorded neural signals during the contractile period. The cross-correlations using GCC, SCOT and ML methods are shown in Fig 6.4a, 6.4b, and 6.4c respectively.154
6.5	The peak values of the sensory and the motor cross-correlation by SCOT technique with respect to time from Fig 6.4b. Downward arrows indicate peak of contractions.....158



LIST OF ILLUSTRATIONS

FIGURE	PAGE
6.6	Cross-correlation between N21 and N22. When there are no measurable contractile activities.....160
6.7	An example of the neural signals N21 and N22 from a damaged nerve trunk and its corresponding contractile and EMG activities.....165
6.8	The cross-correlation of the neural signals (N21,N22) from a highly damaged nerve trunk (Fig 6.7, Box A).....167
6.9	Example of the neural signals corrupted with movement artifacts and the corresponding EMG and contractile activities.....172
6.10	The cross-correlation of the neural signals corrupted with movement artifacts.....174
6.11	Series of sensory and motor patterns with respect to the duration of the cuff electrode implantation.....178
6.12	Average sensory peak location vs. the implanted duration of the nerve cuff.....181
6.13	Results of stimulating the nerve of Latarjet using cuff N2 with stimulus parameters of 10V, 6 pps, and 1 msec in duration.....183
6.14	Results of stimulating the Nerve of Latarjet using cuff N1 with a parameter of 5 V, 3 pps, and 1 msec in duration.....185
6.15	Averaged impulse obtained from 64 stimulation impulses from the Cervical vagal nerve.....188
6.16	Low magnification micrograph of a cross-section of the vagal nerve (nerve of Latarjet) from a control dog.....191
6.17	Low magnification micrograph of a cross section taken from nerve which had been encased in a nerve cuff over a period of 3 months.....191

LIST OF ILLUSTRATIONS

FIGURE	PAGE
6.18	High magnification micrograph of a cross-section of a control vagus.....193
6.19	High magnification of a cross-section taken from nerve which has been enclosed in nerve cuff over a period of 3 months.....193
6.20	Cross section of a nerve which had been enclosed in the nerve cuff over a period of 3 months.195
6.21	Cross section through severely damaged vagus, which had been enclosed in a nerve cuff over a period of 3 months.....195
6.22	The average impedance of 6 cuff electrode as function of frequency and days.....199
6.23	The average impedance of three cuff electrodes with highly damaged nerve trunks.....200

LIST OF ABBREVIATIONS

BER - Basic Electric Rhythm
DFT - Discrete Fourier Transform
dB - decibel
ECA - Electrical Control Activity
ERA - Electrical Response Activity
EMG - Electromyogram
FFT - Fast Fourier Transform
FT - Fourier Transform
GCC - General Cross-Correlation
GI - Gastrointestinal
GWN - Gaussian White Noise
IMP - impulses
ML - Maximum Likelihood
PSD - Power Spectral Density
SCOT - Smoothed Coherence Transform
SINE - Sine wave
SNR - Signal-to-Noise ratio



CHAPTER I

INTRODUCTION

1.1 INTRODUCTION

Gastrointestinal (GI) motility involves the study of the function of the gut as the ingested material is mixed, triturated, digested, absorbed, and propelled. The various organs of the GI tract include the esophagus, liver, pancreas, stomach, small intestine, and large intestine. Specific motility patterns in response to the ingested material are brought about by the integration, in time and space, of three control systems: myogenic, neural, and hormonal. These functions almost always operate inter-dependently. However, it is thought that the myogenic control system is the one immediately responsible for the control of GI motility [Daniel et al 1960]. The myogenic control system is in turn modulated by the hormonal and neural control systems.

Components of the hormonal control system are activated in response to the various types of ingested material and may modulate myogenic control directly or indirectly by affecting neural controls. The neural control system is brought about by the activation and integration of both intrinsic (within the gut wall) and extrinsic nervous systems, initiated by stimuli external and internal to the gut and affected by hormonal

controls [Debas et al 1975, 1977, Fox et al 1980].

Consequently a study of GI motility necessitates the monitoring of the three control activities. In this regard much attention has been devoted toward understanding myogenic activity and its modulation as per input from other systems by monitoring the electrical and contractile signals with electrodes and strain gauges respectively, both in humans and animals [Bortoff, 1975; Daniel and Chapman, 1963; Daniel and Irwin, 1968]. The role of various hormones in gut motility are usually analyzed by monitoring blood samples and myogenic activities [Debas et al, 1975; Fox et al, 1977].

On the other hand, not much has been accomplished in monitoring the neural activities in relation to myogenic activities. The GI tract is richly innervated with an intrinsic neural network embedded in the intestinal wall [Furness and Costa, 1980]. The intrinsic nervous system appears to be capable of modulating the myogenic activities without extrinsic inputs [Kelly and Code, 1969; Papazova and Atanassora 1972]. This is possible, because the intrinsic nerves have both sensory and motor components. The extrinsic nervous system appears to influence GI motility mainly via the intrinsic nervous system, but the nature of the interactions between the extrinsic nerves, intrinsic nerves, and the smooth muscle cells remains unclear.

Our present knowledge of the neural control of GI motility is mainly based on acute in-vivo experiments in anesthetized animals or on in-vitro studies of isolated gut tissues. These however pose significant disadvantages (discussed in the next chapter). Milan and

Roman [1978] have studied unanesthetized animals by suturing the vagal motor fibers, some of which are involved in central nervous system control of gastric (stomach) motility, to the peripheral end of the left phrenic nerve (nerve that innervates the diaphragm). The activity patterns of the motor units of the innervated diaphragm studied in parallel with physiological variables affecting gut motility provided an indication of the nature of the vagal motor fibre activity. Hall and Diamant [1982] studied the problem in unanesthetized animals in-vivo by blocking the cervical vagal nerves by cooling and examined the resultant changes in motility patterns. The findings of both these investigators suggest that the vagal nerve plays an important role in the control and coordination of gastric motility. However, neural activities and their corresponding motility patterns have not been reported in conscious animals.

In the absence of sufficient data, it is not possible to understand the integration of the neural controls with the myogenic controls. This lack of information is mainly due to the difficulties encountered in developing techniques for implanting electrodes on the gut nerve trunk and for recording and analyzing low amplitude nerve signals.

Within a nerve bundle, which can consist of thousands of nerve fibres, each fibre can generate characteristic action potentials (next chapter). Recording separately from these individual fibre yields an impulse like waveform [Davison and Grundy, 1978; Grundy et al, 1981; Milan and Roman, 1978]. These individual fibres, however, can fire

synchronously or asynchronously, independent of each other. Let M be the summation of all the individual fibre potentials at any instant time then,

$$M(t) = \sum_{i=1}^N n_i(t) \quad 1.1$$

Where n_i is the instantaneous potential produced by the i^{th} nerve fibre. As per the Central Limit Theorem [Papoulis, 1965], $M(t)$, approaches a Gaussian probability distribution as the number of samples (N) increases without bound and so long as the $n_i(t)$ are independent. Hence recording from a large nerve trunk tends to yield a random waveform. Thus these nerve fibres may, at a given instant, carry sensory or motor impulses by virtue of the nerve consisting of both sensory and motor fibres. In order to understand the mechanism of the extrinsic neural control of the GI system, it is necessary to be able to separate the distribution of motor and sensory signals from the measured compound signals; and correlate them to the underlying GI motility patterns.

More than any other organ system of the body, the GI tract consists of an heterogeneous collection of dissimilar organs, i.e. the structure and functions of, for example, the esophagus and the stomach are as dissimilar as are those of the small and the large intestine. This dissimilarity among the functions of the components of the systems adds complexity to the study of the GI physiology. This thesis deals with the stomach (gastric) and duodenum (proximal part of the small intestine) portion of the GI system. The techniques developed in this

study, however, can easily be adapted to any other portion of the GI system.

1.2 OBJECTIVES OF THE RESEARCH

The objectives of this research include:

- (i) the development of an instrumentation system to record neural signals innervating the stomach in conscious animal chronically (in-vivo) including a cannula system consisting of electrodes and strain gauges for implantation;
- (ii) the development of computer algorithms to explore the sensory and motor neural patterns from the recorded compound neural signals;
- (iii) the study of the recorded neural signals:
 - (a) for the distributions of the motor and sensory activities from the measured compound neural signal using a laboratory oriented personal computer system;
 - (b) the correlation of the motor and sensory activities to the corresponding contractile activities; and
- (iv) the evaluation of the effects of this instrumentation on nerves.

1.3 ORGANIZATION OF THE THESIS

The organization of this thesis is as follows:

Chapter II deals with a review of the general anatomy and functions of the GI tract, the control of GI motility, and methods for investigating gastric motility. Chapter III deals with a basic review of the generation of the neural signals, their statistical characteristics, and algorithms for estimating the sensory and motor patterns from the recorded compound neural signals. The procedures for fabricating the various electrodes, instrumentation requirements, computer facilities, and implementation of the various algorithms in analyzing the neural signals are given in Chapter IV. In Chapter V, the performance of the various algorithms are evaluated using three different simulated signals. In Chapter VI, using the various algorithms, the sensory and motor patterns of the recorded compound neural signals are analyzed under various conditions such as: during periods of contractions; during quiescence; in the case of highly damaged nerve trunk; and, signals contaminated with artifacts. The conditions of the nerve trunk and of the cuff electrode studied by the electron microscopy and impedance measurements are given. The discussions of the simulation results and analysis of the neural signals are given in Chapter VII. Finally conclusions and suggestions for further studies are given in Chapter VIII.

CHAPTER II

REVIEW OF THE CONTROL OF THE GASTROINTESTINAL (GI) SYSTEM

2.1 INTRODUCTION

In order to comprehend how the neural system influences GI motility, it is essential to have a basic understanding of the physiology and functions of the GI system. In this chapter a brief review of the physiology of the GI system is given. A detailed description can be found in various physiology textbooks and reviews [Daniel and Irwin, 1968, Davison J.S. 1983, Bortoff A. 1976]. Since this thesis deals with the neural activities of the stomach (gastric system), the main emphasis will be on the neural control system. The organization of this chapter is as follows: (i) general anatomy and functions of the GI tract; (ii) review of the control of GI motility; and, (iii) methods for investigating gastric (stomach) motility.

2.2 GENERAL ANATOMY AND FUNCTIONS OF THE GI SYSTEM

The primary function of the GI tract is to provide the body with a continuous supply of water, nutrients, and electrolytes and to remove certain waste products. This is achieved by (i) facilitating the

mixing, trituration, and movement of food through the GI tract at an appropriate rate; (ii) secreting gastric juices and various enzymes for the digestion of food; (iii) absorbing the digested food, water, and various electrolytes, and, (iv) secretion of certain substances for purposes of excretion. The general structure of the GI tract of dog is show in Figure (2.1).

2.2.1 MOUTH AND ESOPHAGUS

As food enters the mouth, it is chewed into small pieces before it is swallowed. This chewing mechanism helps to increase the surface area of the food exposed for intestinal secretion which helps digestion. As the chewed food is swallowed and enters the pharynx (Figure 2.1), the upper esophageal sphincter is opened allowing the bolus to enter the upper esophagus by a naturally controlled mechanism, the peristaltic wave. This transit requires integrated activities of voluntary and involuntary muscles with the assistance of voluntary activities from the pharynx and is accomplished in approximately 1 to 2 seconds. The primary function of the esophagus is to transfer food from the pharynx to the stomach. An esophageal peristaltic wave propels the food aborally to the lower esophagus, opens the lower esophagus sphincter and allows the bolus to enter the stomach.

2.2.2 STOMACH

The main functions of the stomach are: (i) storing the large

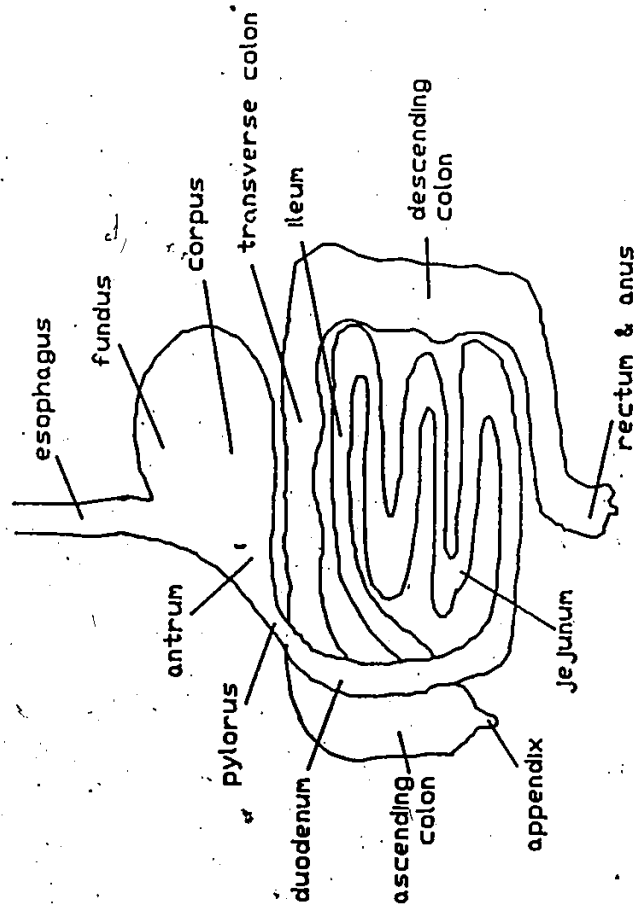


Figure 2.1 Gastrointestinal tract of a dog

quantity of food until it can be transported and accommodated in the lower portion of the GI tract (the fundus, which undergoes receptive relaxation); (ii) mixing the food with gastric secretions, and triturating it until large particles are broken down to an appropriate size; and (iii) emptying the food into the duodenum at an appropriate rate corresponding to the type of food. Anatomically, the stomach can be divided into three parts (Figure 2.1): fundus, corpus, and antrum. As the food enters the stomach, it is stored in the fundus and the corpus region. These two regions, mainly the fundus, relax and increase in volume progressively with little increase in pressure (receptive relaxation) to accommodate more food. The gastric juices are secreted from the secretory glands of the stomach which cover almost the entire wall of these two regions. The food stored closest to the stomach wall directly contacts the gastric juices. Within a short period after the food enters the stomach, regular rhythmic contractions occur in the gastric corpus and antrum. In general these rhythmic contractions originate around the corpus region and propagate with increasing intensity and velocity towards the pyloric region. This peristaltic type of contraction is also called the mixing wave. As the peristaltic wave squeezes the stomach contents towards the pylorus ring, the pylorus contracts and closes. Prior to its closure, liquid and some gastric particles of diameter less than the resting diameter of the pylorus are expelled. The majority of the chyme is retropelled from the pyloric ring towards the corpus, thus resulting in a mixing and triturating action. This action helps to prevent (i) the undigested large food particles from entering the duodenum, and (ii) the reflux of duodenal

contents back into the stomach and reduces damage to the stomach. The antral peristaltic wave, when active, occurs at a maximal rate of approximately 3 times per minute in humans and 5 per minute in dogs as per the rate ECA. After the food has been thoroughly mixed with the gastric secretions and triturated, it is passed down to the small intestine. The food at this stage is milky, semifluid, and is called chyme, which has already undergone some digestion by gastric secretion enzymes.

2.2.3 SMALL INTESTINE

The small intestine which is the longest portion of the GI tract consists of duodenum, jejunum, and ileum (Fig. 2.1). The major functions of the small intestine are: (i) secretion of digestive enzymes, and mixing of these and bile with chyme, i.e., digestion of chyme (ii) absorption of nutrients, and (iii) propulsion of the chyme toward the large intestine. The chyme is propelled through the small intestine by peristaltic and non-peristaltic waves which also help to spread the chyme along the small intestinal wall for optimal surface contacts. This contractile activity usually greatly increases immediately after a meal. The chyme may be held up at the ileocecal valve for a few hours until more food is eaten. Another function of the ileocecal valve is to prevent the backflow of fecal content from the colon into the small intestine.

2.2.4 LARGE INTESTINE (COLON)

The basic functions of the colon are: (i) the absorption of water and electrolytes, (ii) storage of fecal matters until absorption is completed or until defecation is possible, (iii) defecation at an appropriate time. The colon basically consists of three parts: ascending, transverse, and descending colon. A short sac-like area where the ileum joins the colon is called cecum. In humans, though not in dogs, an appendix is present on the cecum; both cecum and appendix appear to have no significant functions in these species. Most of the water and electrolytes are absorbed in the ascending colon, and some in the transverse colon. One of the important functions of the descending colon is the storage of the fecal matters. The movements of the colon contents are mostly sluggish, and bring about mixing but not propulsive type of contractions. In the mixing movement (also called haustration) the fecal material is gradually exposed to large intestinal surface for the absorption of water and electrolytes. The propulsive movement (also called "mass movement") occurs infrequently around the transverse and the descending colon forcing the fecal material towards the rectum.

2.2.5 RECTUM AND ANUS

The excretion of the waste material, known as defecation, is controlled by the anus and voluntary abdominal contraction. The anus consists of an internal anal sphincter, and an external anal sphincter.

As the propulsive movement pushes the feces towards the anus, the internal sphincter is relaxed. If the external sphincter also relaxes defecation will occur. The external sphincter, like the abdominal muscle, can be controlled voluntarily, to enable defecation to occur at a suitable time.

2.3 GENERAL PRINCIPLES OF GI MOTILITY

One of the most important features of the GI tract is the involuntary self-regulation process that keeps the food moving at an appropriate pace - slow enough for trituration, digestion, and absorption but fast enough to provide the nutrients needed by the body. Only swallowing and defecation are subjected to voluntary control. The pace of movement varies according to the specific functions of the corresponding portions of the GI tract and their controls. The movements take many forms and are termed "motility". The basic unit that supplies the power for motility is the smooth muscle cells.

2.3.1 SMOOTH MUSCLE

Smooth muscle is one of the three types of muscles that make up the musculature of the body. The other two types of muscle are striated (skeletal) muscle for body movement, and striated cardiac muscle for heart function. Smooth muscle is found in the GI tract and other hollowed structure organs such as the bladder, uterus, and blood vessels. These muscles are controlled or regulated by the autonomic

nervous system. For the GI system, especially the small intestine and stomach, the smooth muscle cells are mainly arranged in two layers with the outer layer longitudinal to the gut axis oriented at 90° to the inner layer which is the circular layer (Figure 2.2 a,b). When one or more of the circular smooth muscle cells are stimulated and depolarized prior to contraction, the electrical changes can be transmitted to the adjacent smooth muscle cells through cell contacts, known as gap junction [Larsen, 1983]. Longitudinal muscle contains few or no gap junctions [Daniel, 1977] and membrane potential changes are transmitted to other cells in this layer by other junctions. In the esophagus, stomach, and small intestine, only the circle muscle layer have gap junctions and there may be none in the muscles of the colon [Daniel, unpublished]. Smooth muscle cells innervated by intrinsic gut nerves do not have the classical post-synaptic structure (end-plate) as do the skeletal muscle cells [Katz, 1966; Burnstock, 1979]. The response of the smooth muscle to neural stimulation is much slower because of the greater space between nerve release site and smooth muscle response site.

The GI tract smooth muscle, like most of the other types of smooth muscles, exhibit both tonic contractions and rhythmic or phasic contractions. Tonic contractions usually are continuous or long lasting up to minutes or even hours. The degree of the tonic contraction of the specific segment of the GI tract and the resistance of adjacent segments to volume decrease in that segment determine the intensity of steady pressure at the corresponding site. At the lower esophageal sphincter, pyloric, ileocecal, and anal regions, there are often muscles undergoing

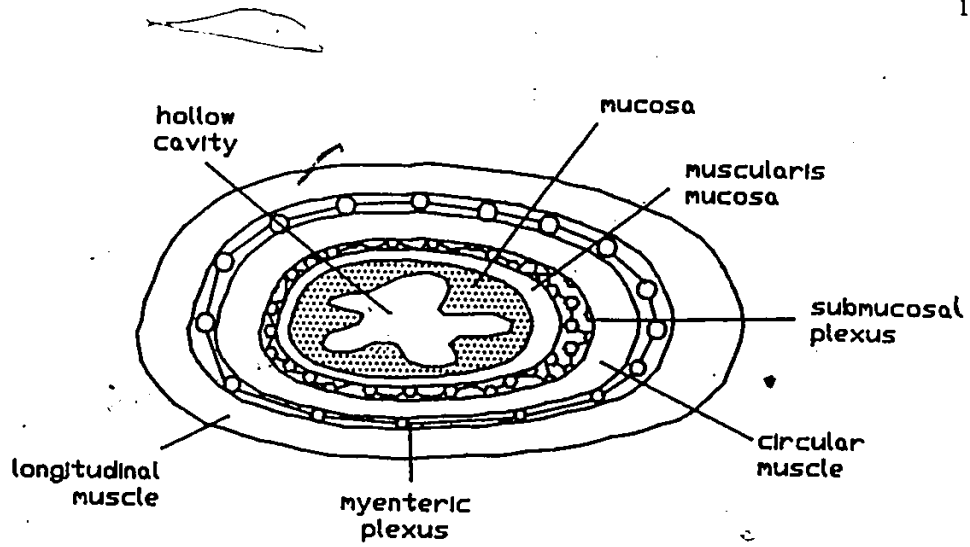


Figure 2.2a Muscle Layers of the Gastrointestinal Tract

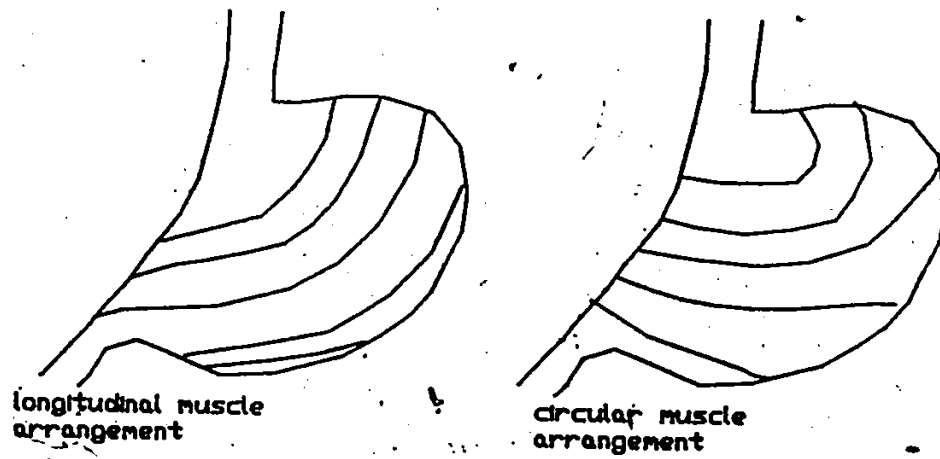


Figure 2.2b Smooth muscle Layers of the stomach

continuous tonic contractions which prevent transit of food in either direction except when reflex relaxation occurs, thus regulating the mixing, onward propagation, and reflux.

The rhythmicity of contractions varies in different regions of the GI tract. For example, in humans, the rhythmic contraction of the stomach is approximately 3 per minute (5 per minute in dogs), 12 per minute in the duodenum (18 per minute in dogs). This rhythm is determined by the myogenic electric control system (slow waves, pacemaker activity, electrical control activity) of each region discussed below.

2.3.2 CONTROL OF THE GI MOTILITY

There are basically three factors that control the GI motility viz., myogenic, hormonal, and neural as discussed below.

2.3.2.1 MYOGENIC CONTROL

The smooth muscle of many parts of the gut exhibits rhythmic electrical activity without the intervention of extrinsic neural and hormonal activity. It has been claimed that these rhythmic oscillations originate from the longitudinal muscle layer (Figure 2.2 a,b) [Bortoff, 1975], but this is still uncertain. The rhythmic phenomena is caused by the oscillatory ionic flow across the membrane of the smooth muscle cell. Detailed description of the oscillatory ionic flow can be found in [Daniel and Sarna, 1978]. This rhythmic oscillation is variously

known as slow wave, pacesetter potential, electrical control activity (ECA), or basic electric rhythm (BER) [Daniel and Chapman, 1963; Sarna et al, 1971, and Bortoff, 1975]. Muscular contraction takes place in response to a second rapid potential associated with increase in cytoplasmic Ca^{++} ; the potentials can be initiated during the depolarized phase of the slow wave and therefore occur superimposed on the slow wave. These rapid potentials are usually called fast action potentials, spike activity, electrical response activity (ERA), or simply spike bursts. For the remainder of the thesis, the slow wave will be referred as ECA and the fast waves as ERA. Since spikes occur only once per given cycle, the frequency of the ECA appears to control the occurrence of the ERA oscillatory response [Daniel, 1977; Bortoff, 1975]. A typical relationship among ECA, ERA, and the stomach contractile activities of the antrum region is shown in Figure 2.3.

2.3.2.2 HORMONAL CONTROL

Recent studies [Daniel et al, 1983] show that many GI hormones may exert their control of GI motility through effects on intrinsic or extrinsic nerves and sometimes directly on smooth muscle of the gastric system. However, it is difficult to quantify the importance of their role because of difficulty in separating out neural, myogenic, chemical and other influences on the motility. A detailed review of the action of GI hormones is given in [Glass, 1980].

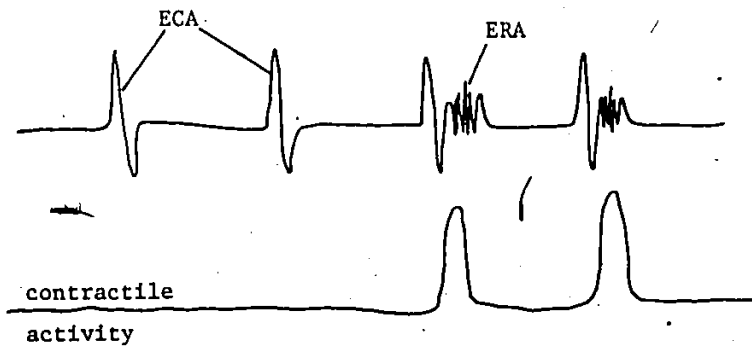


Figure 2.3 Typical waveforms of ECA, ERA, and its corresponding contractile activity of the stomach antrum.

2.3.2.3 NEURAL CONTROL

The basic function of the central nervous system which includes the brain and the spinal cord is to transmit information from one place to another and to process and integrate the information according to the stimulus received. The information is transmitted in the form of impulses via the nerve fibres. The nerves are almost always arranged in a group of parallel fibres called nerve bundles. The overall pattern of these impulses from a single nerve fibre or a nerve bundle is called nerve signal.

The pathway whereby the central nervous system transmits neural signals to and from the gastric system is known as the autonomic nervous system. This system consists of two major systems: sympathetic and parasympathetic (vagal or sacral) systems. We can oversimplify by stating that these two systems have opposite functions: one stimulates and the other inhibits the motor activities, i.e. stimulation of the vagal nerves generally excites the stomach wall, whereas stimulation of the sympathetic nerve inhibits the activities of the stomach wall [Daniel and Sarna, 1975, 1976]. Sensory signals from the various parts of the GI tract are transmitted via these systems to the brain stem and spinal cord, which then in turn relay the appropriate reflex response as motor signals back to the corresponding location. There are also ganglia outside the CNS that perform integration of gut neural control. Those nerves, that are located outside the GI tract wall are called extrinsic nerves. In addition there is another important set of nerves

embedded in the tract wall called intrinsic nerves. The simplified organization of these two neural networks is shown in Figure 2.4.

2.3.2.3.1 EXTRINSIC NEURAL NETWORKS

The extrinsic neural network consists of parasympathetic and sympathetic nerves innervating the entire GI tract. The vagus nerves of the parasympathetic system mainly innervate the upper portions of the GI tract from the brain stem, whereas the sympathetic system nerves are mostly from the spinal cord (Figure 2.4). The branches of the vagus nerves that innervate the stomach are called the nerves of Latarjet. The distribution of excitatory vagal fibres of the nerves of Latarjet on a dog stomach wall is given in [Daniel et al, 1976]. It is thought that less than 20% of these nerves are efferent (motor) fibres while more than 80% are afferent (sensory) fibres [Agostini, 1957; Abrahamsson, 1973]. However the degree and the nature the extrinsic nerve control varies along the different parts of the GI tract. Extrinsic nerves play more important role in the esophagus and stomach than in the small intestine. Due to the independent functional capability of the intrinsic nervous system, most parts of the GI can function almost normally even without the extrinsic neural supply and most parts can adapt their functions to the absence of extrinsic neural inputs. The role of the extrinsic nerves thus appears to be to modulate the intrinsic control. The exact mechanism of the neural control of GI motility remains unclear.

Our knowledge of the extrinsic neural control on GI motility is

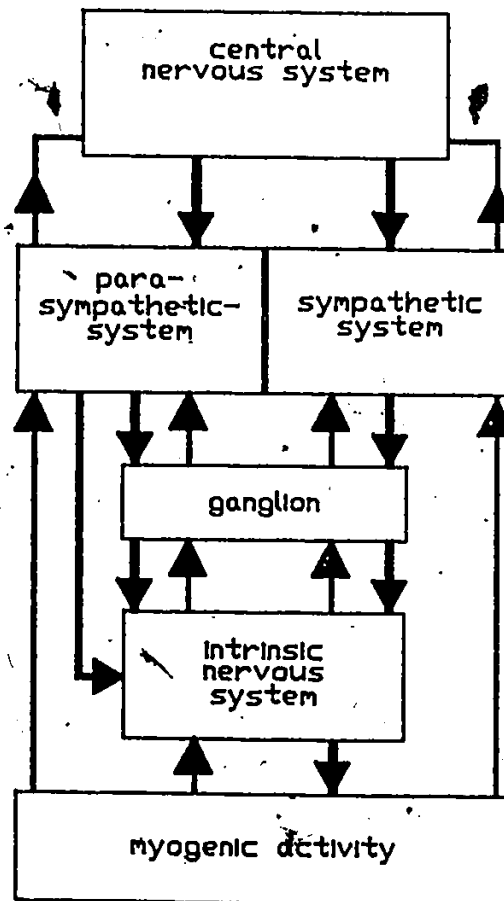


Figure 2.4 Simplified block diagram of the organization of the extrinsic and intrinsic neural network

mainly based on studies involving the removal of the extrinsic neural supply to the various portion of the GI tract and observing changes in the corresponding motility patterns. In the stomach region, after severing the vagal nerves (vagotomy), the fundus no longer shows relaxation after swallowing, resulting in a decrease in the storage capacity of the stomach [Cannon 1911]. The intragastric pressure is higher than normal and the peristaltic force also weakens at least at the initial few months [Jansson 1969, Wilbar and Kelly 1973]. Also after vagotomy, emptying rate of solid food is decreased, whereas emptying rate of liquids is increased. This suggests that contractions in the upper portion of the stomach increase the emptying of liquids, whereas weakened peristaltic force at the lower portion of the stomach delays solid food emptying. Immediately after vagotomy, the electrical activities, ECA and ERA, temporarily show total disorganizations and hence the contractile activities are not synchronized [Kelley and Code, 1969; Papisova and Atanassova, 1972]. Usually after about a week, the EMG returns to nearly normal patterns. This suggested that the intrinsic neural system is probably adapts and compensates for the decreased extrinsic vagal input [Röman 1982].

There is less information regarding the effects of severing the sympathetic nerves innervating the stomach (splanchnic nerves). It is generally stated that cutting of splanchnic nerves increases tone and the force of peristalsis [Kosterlitz, 1968], and hence increase gastric emptying. This operation has less disturbing effects on the stomach than vagotomy.

2.3.2.3.2 INTRINSIC NEURAL NETWORK

These nerve cells are embedded in the GI tract wall in the form of a tightly interconnected network known as intramural plexuses or enteric nervous system [Langley, 1921] (Figure 2.5). There are two major plexuses: submucosal (or Meissner's) plexus located in the submucosa, and myenteric (or Auerbach's) plexus located in between the main muscle layers of the tract wall. These plexuses cover the entire length of the GI tract except for the striated muscle portion of the esophagus. They can communicate among themselves, between smooth muscle cells, or with the extrinsic nerves. They also receive sensory input from the gut sensory nerves. The intrinsic neural plexuses appear to be capable of more than just relaying information; they also process information and carry out complex integrative functions independent of the central nervous system [Gershon, 1981; Wood, 1981]. In the stomach and duodenal junction region, the intrinsic neural network appears to play a basic role in the correlation between the spike activities (ERA) of the stomach and the duodenum [Atanassova 1976].

2.4 METHODS OF INVESTIGATING GASTRIC MOTILITY

From the above discussions, it is clear that the study of gastric motility necessitates the simultaneous monitoring of the myogenic activities, mechanical movements, and neural activities.

parasympathetic &
sympathetic
nerves

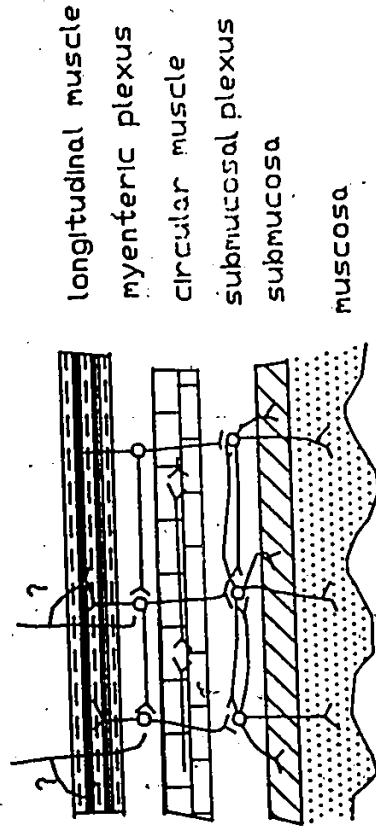


Figure 2.5 Some interconnections between the intrinsic and extrinsic nerves. The above diagram is a simplified diagram to illustrate the interconnection between the intrinsic and extrinsic nerves. The actual interconnecting circuitry is much more complex than as given in the diagram

2.4.1 MYOGENIC ACTIVITIES

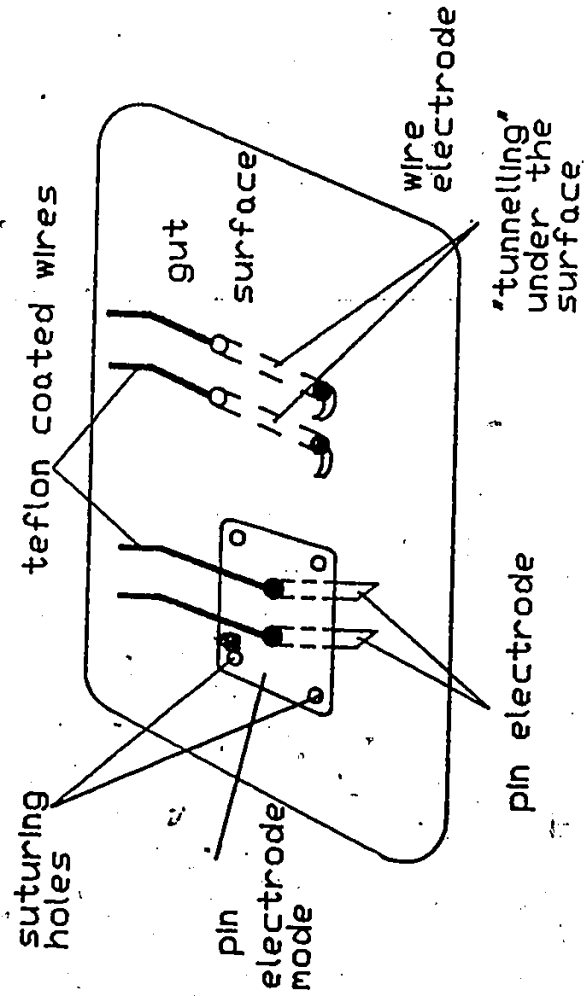
The bioelectric events of the smooth muscles can be measured by a pair of electrodes. Hence, implantation of these electrodes on the stomach muscles permits the measurement of the electrical activities of the gastric smooth muscle. The typical waveshape of the signals is shown in Figure 2.3. There are basically two recording techniques to measure the muscular electrical activities: serosal and intraluminal.

2.4.1.1 SEROSAL RECORDINGS

In this technique, the electrodes are sewn onto the stomach wall, directly under the serosa or deeper into the muscularis. There are two kinds of electrodes used for this recording: pin and wire (Figure 2.6), each with its own advantages and disadvantages. The metallic pins of the pin electrode are held firmly in place in the mold. Hence the electrode would remain in reasonably the same configuration throughout the recording. During the implantation, the electrodes are sewn with the mold firmly onto the stomach wall and later connective tissue overgrows the implant and insulates it. Thus the chance of the electrode picking up artifacts, such as respirations, and movement of other parts of the GI tract is small.

The major disadvantages of the pin electrodes are the pin length and the size of the electrode. Long pins can puncture through the stomach wall, so as to measure the electrical activities of both the

Figure 2.6 The pin and wire electrode for the myogenic activities.



longitudinal and circular muscles together. If the electrode mold that holds the pins in place is too big or rough in surface, excess fibrous tissue may grow around the electrode. After a long period of time, this might change the muscle characteristics.

Wire electrodes, on the other hand, are light-weight and less detrimental to the system. They can be implanted by 'tunneling' just underneath the longitudinal muscle layer. These electrode, however, cannot be implanted as securely as the pin electrodes. There is also higher probability of the wire coming loose from the implanted site, especially during long term chronic recording. After a period of time and numerous contractions, part of the the bare wire portion (Figure 2.6) of the electrode may protrude through the muscle and when so exposed causes a 'noisy' environment.

Both types of electrodes are currently used in various laboratories, with pin electrode electrodes implanted in chronic animals and wire electrodes used in humans or in acute animal models. More studies are needed to make quantitative comparisons between the two electrodes.

In this research, the pin electrode was employed. The method and materials of making the electrodes are given in Chapter IV.

2.4.1.2 INTRALUMINAL RECORDINGS

This technique measures the bioelectric event from inside the stomach. The electrode similar to the pin-type one described above is inserted into a suction cup and mounted on a tube. Once the tube has

been inserted, into the colon for example, via the anus, suction is applied to maintain the close contact between the electrode and the gut wall. There are technical problems in obtaining these records and major problems in their interpretation. This technique, therefore, is not practical for animal experiment especially for the nature of this study.

2.4.2 CONTRACTILE ACTIVITIES

The early studies (Cannon, 1911) of the gastric movement were performed by visualization of animals during laparotomy. Radiography has also been used to observe the movements of stomachs in patients. These techniques however fail to provide quantitative, objective measurements. There are two techniques commonly used on animals to study the gastric contractions: extraluminal measurements and intraluminal pressure measurement.

2.4.2.1 EXTRALUMINAL MEASUREMENTS

In this technique, the gastric contraction is measured by suturing either force transducers or displacement transducers onto the stomach surface [Bass and Wiley, 1972; Mendel et al, 1979]. The limitations of this technique are the breakage of the strain gauge (especially at the soldering joints) and the development of fibrous tissue growing around the transducers and affecting their recording. For this study, the strain gauge mounting was made much thinner and more flexible. This decreases the load on the stomach surface and allows

strain gauge to readily follow the contractile activities. The theory, method, and materials of making the transducer are described in detail in the next two chapters.

2.4.2.2 INTRALUMINAL PRESSURE MEASUREMENTS

There are various methods for measuring the intraluminal pressure, such as: open tipped tubes, continuous-perfused catheters, tubes (Tigon or silastic) mounted with strain gauges, and tubes attached with balloon distended with air or water. These transducers are often sensitive around the sphincteric area, but variably sensitive or insensitive inside the stomach cavity.

2.4.3 NEURAL ACTIVITIES.

As mentioned earlier, our present knowledge of the extrinsic neural control of the gastric system is mainly based on severing or destruction of the whole or part of the extrinsic nerve supply and observing the gut system responses. Another method is to dissect the nerve trunk carefully and record from a single nerve fibre [Davison and Grundy, 1978]. All these studies are performed in the anesthetized state. Study of the nervous system in acute experiments under anesthesia have several significant disadvantages that affect the interpretation of the results: (i) depending on the type and depth of anesthesia, in the anesthetized state, the central nervous system activities can be partially or totally disorganized; (ii) recording from

a single nerve fibre (efferent or afferent) by dissecting a nerve trunk can be very tedious and create complications and often the site of innervation cannot be located for comparison; (iii) placing the nerve fibre on a pair of (hook or similar) electrodes and wetting with saline for a long period of time can cause swelling and affect the neural transmission; and, (iv) in acute experiments there is limited opportunity for repetitive testing and for study of long term effects.

Roman and Milon (1976) have employed an indirect method to study the extrinsic neural activities in fully conscious animals. They carefully cut a vagal motor branch that was thought to carry nerve axons involved in central nervous system control of gastric motility and sutured it to the peripheral cut end of the phrenic nerve (nerve that innervates the diaphragm). Then, a portion of the diaphragm becomes innervated by the regenerated vagal nerve. The electrical activities of the reinnervated muscle (easily recorded) reflect the vagal neural activities. They then exteriorized the reinnervated portion of the diaphragm muscle to the body surface to study the vagal neural activities. In another case, Hall and Diamant (1982) investigated the problem in-vivo by blocking the cervical (neck) vagal nerves bilaterally (on both sides of the neck) by cooling and observed gastric motility. Their findings suggested that the vagal nerves are important factors in the control of gastric motility. There do not appear to be any other publications showing the neural activities from the nerve trunks innervating the stomach and its corresponding gastric motility.

In this study a nerve cuff electrode was developed to record the neural signals. The rationale and design of the cuff electrodes are

given in the next chapter. The mathematical theory for the analysis of the measured neural signals is also given in the next chapter.

CHAPTER III

MATHEMATICAL BACKGROUND FOR THE ANALYSIS OF THE NEURAL SIGNAL

3.1 INTRODUCTION

In the previous chapter, the basic physiology of the GI system has been reviewed. The necessity of monitoring the neural activities in order to gain a better understanding of the control of the GI system was also mentioned. In this chapter a basic review of the generation of neural signals, together with their statistical characteristics, and algorithms to estimate the sensory and motor patterns from the measured compound neural signals are given.

3.2 REVIEW OF THE NEURAL SYSTEM

In order to analyze the distribution of sensory and motor signals from the measured compound neural signals, it is essential to have a basic understanding of the physiology of the nervous system and the generation of neural signals as discussed below. A detailed description of the subject can be found in many texts [Hodgkin and Huxley, 1952; Katz, 1966].

3.2.1 THE NEURON

The basic unit of the nervous system is a neuron which occurs in a wide variety of sizes and shapes. Generally a neuron consists of: the dendrites with cell body (or soma), the axon, and the axon terminals (Fig. 3.1).

The dendrites form a series of highly branched connections to the cell body. The cell body and the dendrites are the site of most of the specialized junctions where signals are received from other neurons. The cell body contains the nucleus and such organelles as endoplasmic reticulum, and mitochondria to maintain the neuron metabolism, growth, and synthesis of secretory proteins, etc.

The axon, or nerve fiber, is a single nerve process that extends from the cell body through the axon hillock (Fig. 3.1). This long portion of the neuron is usually connected to the neurons, muscles, or glands. An axon is either myelinated or nonmyelinated. Myelin is a tightly layered plasma membrane which is formed from a special cell, known as a Schwann cell. The locations where the Schwann cells meet and free of myelin (Fig. 3.1) are called the node of Ranvier. The myelin insulate the flow of local currents between the node of Ranvier and forcing these currents to flow between nodes along the axon. This arrangement causes more rapid propagation of neural impulses by myelinated nerves as compared to unmyelinated nerves. Generally myelinated axons of larger diameter have longer internodes and faster propagation velocity [Ruch and Patton, 1965; Furness and Costa 1980].

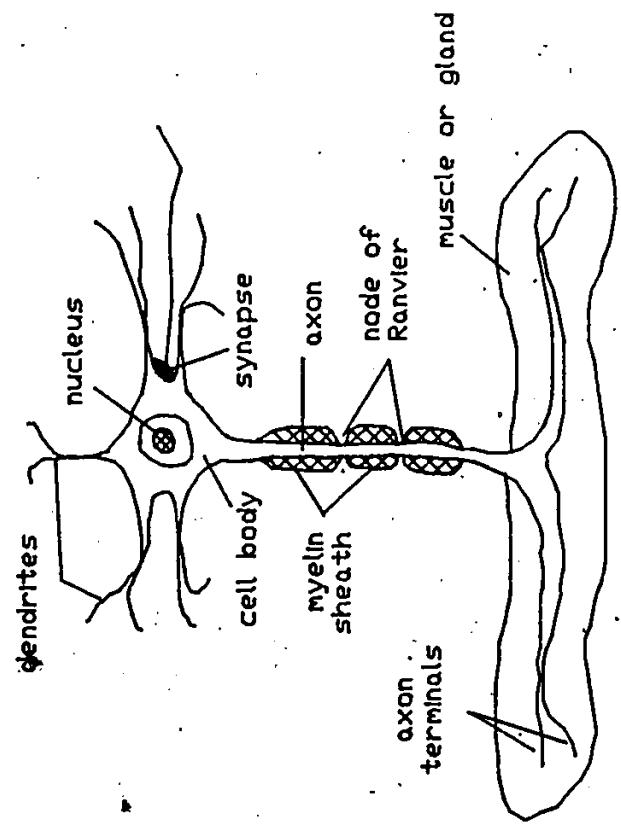


Figure 3.1 Basic structure of a myelinated neuron

The end of an axon branches into many small terminals which are responsible for transmitting signals from the neuron to the other cells by releasing transmitter. In the peripheral autonomic and enteric nervous system, there are myelinated and unmyelinated extrinsic nerves but intrinsic nerves are nearly all unmyelinated. In end organs there are many varicose sites of mediator release along the axon and/or axon terminal.

The neurons that carry signals, hence information, from the peripheral organs to the brain or the spinal cord are called afferent or sensory neurons. The neurons that originate from the central nervous system (brain and spinal cord) and affect such organs as muscles or glands are called efferent or motor neurons. They too may be myelinated or unmyelinated.

3.2.2 GENERATION OF NERVE IMPULSES

In the resting state, the potential inside the neuron cell membrane is approximately -90mv with respect to that of the outside. This potential difference is caused by the differences in concentration of various ions across the membrane. The major ions that contribute to this membrane potential are potassium (K^+), sodium (Na^+), and chloride (Cl^-). The Na^+ and Cl^- concentrations external to the cell are about 10 times as high as those inside, whereas the K^+ concentration inside the cell is about 30 times that of outside. Ions of higher concentration tend to migrate across the membrane to the lower concentration. However, the permeability of these ions across the cell membrane in the

resting state varies : K^+ and Cl^- can diffuse across the membrane much more readily than the Na^+ ions. Hence the resting membrane currents are carried mainly by K^+ and Cl^- and the resting membrane potential is close to the equilibrium potential (potential at which no net ion flux occurs) of these ions. However the membrane potential is far from the Na^+ equilibrium potential and Na^+ ions continually leak into the cell. This continuous passive diffusion of these ions across the membrane requires that Na^+ be pumped out of the cell by a "Na-pump". This pump counteracts the inward "leakage" of Na^+ and maintains the Na^+ gradient and thereby the membrane potential.

Changes in the membrane potential from its resting level (resting potential) are the basis for information to be transmitted by the neuron. Nerve and muscle cell use such change of potential as signals in receiving and transmitting information. When the resting potential is raised by a stimulation to a threshold level, the permeability for the ions, usually Na^+ followed by K^+ changes drastically for a short period of time (a few msec). This rapid and sequential alteration of ionic concentration across the membrane causes a sharp change in membrane potentials resulting in an action potential. During the initial stage (rising phase) of the action potential, the permeability of the Na^+ increases sharply allowing the electrochemical gradient to drive more positively charged Na^+ ions into the cell. This forces the membrane potential to approach the Na^+ equilibrium potential (about +60 mv). This process of causing the membrane potential (measured as inside minus outside) to become more positive than the resting potential is called depolarization. After the short period of

influx of Na^+ ions, its permeability is rapidly turned off, while the permeability of the K^+ ion increases. Since the depolarized membrane potential is less negative inside than the potassium equilibrium potential, K^+ ions exit across the membrane and drive the potential towards the potassium equilibrium potential (about -95 mV). This process is known as repolarization, which returns the membrane potential back to and beyond the resting potential, leading to a period of hyperpolarization before the K^+ permeability declines. A typical neural action potential is shown in Fig. 3.2. After the threshold level, regardless of the strength of the stimulus, the amplitude of an action potential is always the same. This feature is the basis for the so-called "all-or-none" action potential. Because of this all-or-none response to the stimulus, the strength of the stimulus is coded as number of impulses firing within a given period of time.

3.2.3 PROPAGATION OF ACTION POTENTIALS

Once an action potential is generated, the local currents flow caused by the ions flow also causes depolarization at the adjacent site. When the depolarization increases the membrane potential of the adjacent site to the threshold level, it undergoes the same permeability increases described above and the action potential is propagated. Meanwhile, the membrane potential is repolarizing back to the resting level at the previous site. This process of depolarization and repolarization repeats to the end of the neuron membrane unless it is damaged, thus giving the appearance of the impulse travelling through

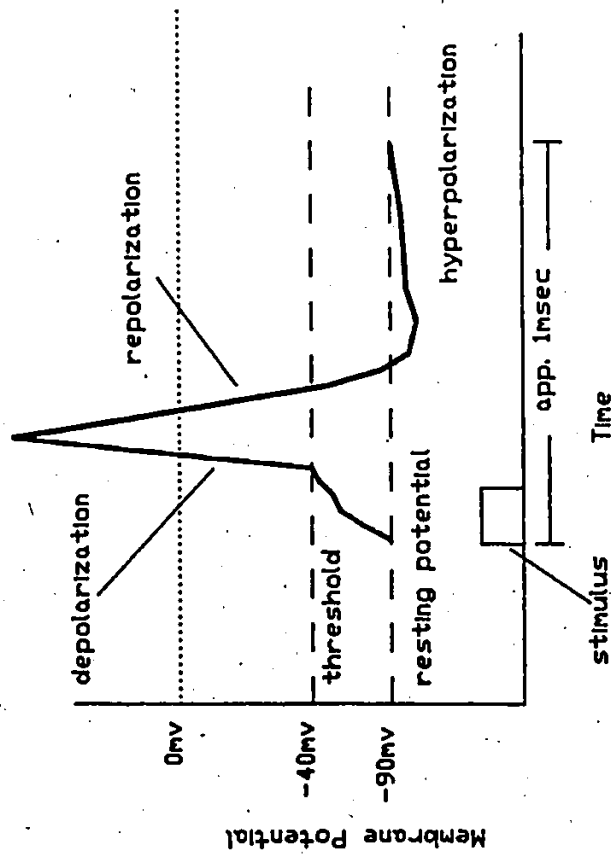


Figure 3.2 A typical action potential with the various phases

the length of the neuron. The velocity of propagation an action potential depends upon the diameter and the myelination of the nerve fibre [Hodgkin and Huxley, 1952; Cragg and Thomas, 1957; Hursh, 1939; Waxman and Bennett, 1973)].

3.2.4 MODE OF RECORDING NERVE IMPULSES

The impulses considered above are measured across the nerve cell membrane between the extracellular and intracellular membrane. This is referred to as the intracellular recording. Based on the understanding obtained from intracellular recording, the propagation and characteristics of the neural signal can also be studied by means of extracellular recording. The basis of extracellular recording methods is given in detail in Rosenfalck (1969), Chung (1974), and Stein (1977). As shown in Fig. 3.3 there are three different extracellular recording configurations: monophasic, biphasic, and triphasic. These configurations will be discussed in the next subsections.

Stein (1980), and Leibovic (1972) show that in extracellular neural recording, the relation of the neural signal level with respect to the propagated distance can be expressed as:

$$\frac{\delta v_i}{\delta x} = -i_a r_a \quad ; \quad \frac{\delta v_e}{\delta x} = i_a r_e \quad 3.1$$

and

$$\frac{\delta v_m}{\delta x} = \frac{\delta(v_i - v_e)}{\delta x} = i_a(r_a + r_e) \quad 3.2$$

where i_a = current flowing down the axon
 r_a = resistance / length of the axon
 r_e = resistance / length of the extracellular space
 v_i = intracellular potential
 v_e = extracellular potential
 v_m = membrane potential

(partial differentiation is used because the measured voltage is a function of both time and distance)

Substituting Eq. 3.2 into Eq. 3.1, the change of extracellular potential with respect to the distance is

$$\frac{\delta v_e}{\delta x} = \frac{-r_e}{r_a + r_e} \frac{\delta v_m}{\delta x} \quad 3.3$$

which shows that the extracellular resistance, r_e , acts as a voltage divider; the extracellular voltage, v_e , is a fraction of the membrane potential v_m . Since the nerve fibre is surrounded with body fluid which has low resistance, the extracellular potential changes are small compared to the intracellular potential [Kirchhoff's Law]. However, if the extracellular resistance is made to be greater than the intracellular resistance ($r_e > r_a$) (by placing the nerve in a nonconducting media, such as paraffin oil), the extracellular voltage is approximately equal to the membrane potential [Leibovic, 1972]. This space that has restricted the extracellular resistance is defined as the

extracellular resisted space.

The wave shape of the extracellular recording depends on both the configurations of the electrodes and the intracellular membrane potential (Fig. 3.3a-c). The three recording configurations are given below.

3.2.4.1 THE MONOPHASIC CONFIGURATION

For the monophasic configuration (Fig. 3.3a), the wave shape is identical to the membrane potential V_m with a reduction of amplitude by $r_e/(r_e+r_a)$ (Hodgkin and Rushton, 1946) i.e.

$$V_{\text{mono}} = \frac{r_e}{r_a + r_e} \cdot V_m \quad 3.4$$

If the conductivity of the axoplasm (intracellular media) and the extracellular fluid are σ_a and σ_e respectively, then $r_a = 1/(\pi a^2 \sigma_a)$ and $r_e = 1/(\pi(b^2 - a^2)\sigma_e)$, substituting into Eq. 3.4, the monophasic potential, V_{mono} , can be expressed as:

$$V_{\text{mono}} = \frac{a^2 \sigma_a V_m}{b^2 \sigma_e + a^2 (\sigma_a - \sigma_e)} \quad 3.5$$

If the extracellular space radius is large compared to the axon, i.e., $b \gg a$ or $\sigma_a = \sigma_e$ then

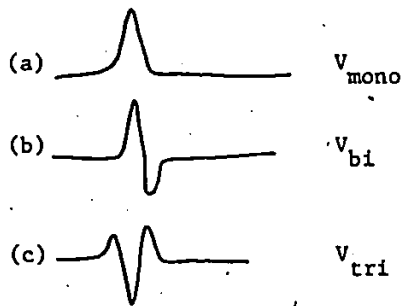
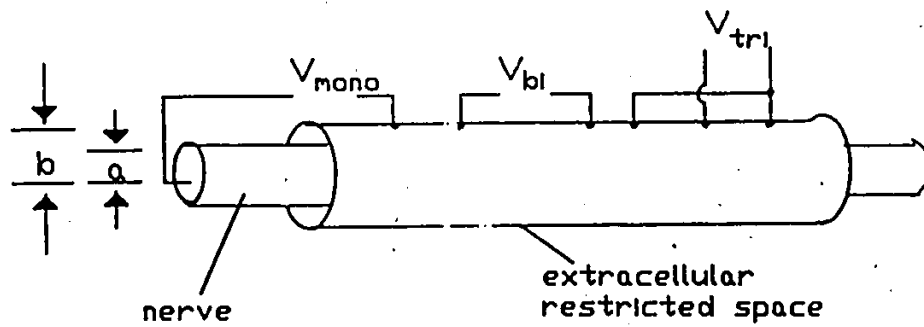


Figure 3.3 Typical wave shape from three different extracellular recording configurations: (a) Monophasic, (b) Biphasic, and (c) Triphasic; a - radius of the fibre; b - distance between the center of the fibre and the extracellular electrode.

$$V_{\text{mono}} = \frac{a^2 \sigma_a v}{b^2 \sigma_e c} \quad 3.6$$

The monophasic potential V_{mono} is proportional to the square of the radius of the axon a , but inversely proportional to the square of the radius of the restricted space b (Fig. 3.3).

3.2.4.2 THE BIPHASIC CONFIGURATION

In the biphasic situation (Fig. 3.3b), both electrodes are placed on the outside of the nerve Δx distance apart. The potential difference is equal to the difference between the monophasic action potentials at the two sites, that is,

$$V_{\text{bi}} = V_{\text{mono}}(x) - V_{\text{mono}}(x + \Delta x) \quad 3.7$$

If the separation between the electrodes Δx is greater than the "wavelength" (propagation velocity multiplied by the pulse width) of the pulse, then the peak-to-peak amplitude of the biphasic potential is approximately $2V_{\text{mono}}$. By following similar reasoning as for the monophasic recording with respect to the intra- and extracellular conductivities, the biphasic potential can be expressed as

$$V_{\text{bi}} = \frac{a^2 \Delta V_m}{b^2} \quad 3.8$$

where ΔV_m is the first difference of the membrane potential, i.e.

$$\Delta V_m = V_m(x) - V_m(x - \Delta x) \quad 3.9$$

3.2.4.3 THE TRIPHASIC CONFIGURATION

For the triphasic recording (Fig. 3.3c), the potential at the centre electrode is recorded with respect to the other two electrodes which are connected together. The potential of the triphasic recording is then

$$V_{tri} = V_e(x) - \frac{1}{2}(V_e(x + \Delta x) + V_e(x - \Delta x)) \quad 3.10$$

If the velocity of the conduction of the action potential is α and the distance between the two electrodes is L , from Eq. 3.3 the above expression can be re-arranged to

$$V_{tri} = \frac{r_e e^{\sqrt{}}}{r_a + r_e} (\frac{1}{2}V_m(t + L/2\alpha) - V_m(t) + \frac{1}{2}V_m(t - L/2\alpha)) \quad 3.11a$$

$$\text{or } V_{tri} = \frac{r_e}{r_e + r_a} \frac{\Delta^2 V_m}{2} \quad 3.11b$$

where $\Delta^2 V_m$ is the second difference of membrane potential.

Thus the triphasic wave shape depends on the length of the restricted

space and the conduction velocity. By manipulating the equations from the biphasic and monophasic configurations the amplitude of the triphasic potential is expressed as

$$V_{\text{tri}} = \left(\frac{a}{b}\right)^2 \Omega^2 V_m \quad 3.12$$

Hence the triphasic potential is proportional to the square of the fibre radius and inversely proportional to the square of the restricted space radius. To the extent that the conduction velocity is approximately proportional to the nerve fibre diameter [Hodgkin and Huxley, 1952, Pearson et al., 1970], the triphasic amplitude is proportional to the square of the length of the restricted space. However as the length of the restricted space increases, the triphasic waveform also broadens, and eventually the peak-to-peak amplitude approaches 1.5 times that of the monophasic potential [Stein & Pearson, 1971].

The triphasic recording configuration has been used widely by a number of researchers in investigating various neural activities in chronic conditions [DeLuca 1976, Hoffer 1975, Stein 1975, Davis 1978, Gordon 1980]. One of the important features of the triphasic configuration is the reduction of environmental noises such as derive from the EMG, and ECG. This is achieved by connecting the two ends of the electrode system together; this procedure provides no potential differences across the electrode. The measured signal is then generated by the neural currents flowing through the electrode. In this study, all the neural signals were recorded with triphasic configurations as discussed in the next chapter.

3.3 STATISTICAL PROPERTIES OF NEURAL SIGNALS

Neural information is transmitted in the form of impulses, and depends upon the rate of the impulses. It is known that neurons show some variability in the interval between successive impulses [Wilbur and Rinzel, 1983; Takeuchi A, 1978]. In this section the statistical properties of impulses from a single nerve fibre, from which the properties of impulse from a nerve trunk can be derived, are discussed.

3.3.1 THE ACTION POTENTIAL AS A SIGNAL

From the all-or-none nature of an action potential (section 3.2.2), an action potential may be considered as a brief pulse, and can be denoted as a Dirac impulse function, $\delta(t)$, [French and Holden 1971] (Fig. 3.4a):

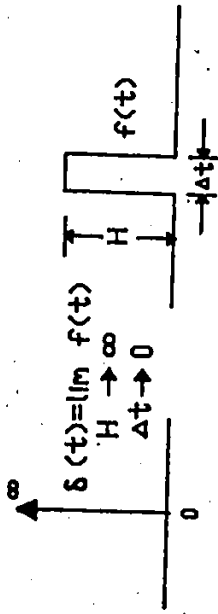
$$\delta(t) = \lim_{\substack{H \rightarrow \infty \\ \Delta t \rightarrow 0}} f(t) \quad 3.13a$$

and

$$\int_{-\infty}^{\infty} f(t) dt = \lim_{\substack{H \rightarrow \infty \\ \Delta t \rightarrow 0}} H \Delta t = 1 \quad 3.13b$$

where H is the height of the pulse and Δt is the pulse width.

A train of impulses can then be expressed as (Fig 3.4b):



(a) The Dirac impulse function



(b) A train of impulses

Figure 3.4 (a) The Dirac impulse function, (b) A train of impulses

$$x(t) = \sum_{i=1}^{\infty} \delta(t-t_i) \quad 3.14$$

where t_i is the time of the occurrence of an impulse.

A review of methods of characterizing impulse trains may be found in Perkel and Seyundo (1966). One of the methods is the interval histogram. Assuming the spike train to be weakly stationary, the properties of the spike train can be characterized as the ordered sequence of intervals $\Delta t = t_{i+1} - t_i$. The probability density function $f(t)$ of the inter-spike interval distribution is defined as [Stein, 1965]:

$$f(t) = \lim_{\Delta t \rightarrow 0} \frac{\text{(prob. of interval between } t \text{ \& } t+\Delta t)}{\Delta t} \quad 3.15$$

The mean inter-spike interval may be determined from

$$\mu = \frac{1}{N} \sum_{i=1}^N (t_{i+1} - t_i) \quad 3.16a$$

Or from the probability density function $f(t)$ i.e.

$$\mu = \int_{-\infty}^{\infty} t f(t) dt \quad 3.16b$$

The variance of the interval is

$$\sigma^2 = \frac{1}{N-1} \sum_{i=1}^N (t_i - \mu)^2 \quad 3.17$$

Even though the probability density function $f(t)$, in principle, can be a Gaussian, Gamma, or a Poisson distribution [Papoulis 1965], in the case of neural impulses, they are mostly characterized by a Poisson distribution [Tuckwell, 1979; Stein, 1965]. For a Poisson process, the occurrence of one impulse is independent of another impulse, and the probability of an impulse occurring in a very short time is constant.

The probability density function of the impulse train can be described as : [Stein, 1965]

$$f(t) = \mu e^{-\mu t} \quad 3.18$$

where μ is the mean firing rate. Eq. 3.18 shows that the spike interval of a Poisson process is exponentially distributed.

3.3.2 SUMMED IMPULSES AS THE NEURAL SIGNAL

When impulse trains from n separate nerve fibres are summed together, then the signal can be expressed as:

$$S(t) = \sum_{i=1}^N x_i(t) \quad 3.19$$

Where $x_i(t)$, $i=1,2,\dots,N$, is the amplitude of the impulse train of the i th neuron. Further $x_i(t)$ is independent of $x_j(t)$ where $i \neq j$.

The signals recorded from the nerve trunk in triphasic configuration will be composed of triphasic wave shapes (Fig. 3.3c) from numerous fibres firing asynchronously and/or synchronously. The individual impulses add and subtract from one another, depending on their phase relationship. Instead of a well defined action potential, the result will be a complex-wave shape. According to the Central Limit Theorem [Papoulis, 1965], as long as the spikes trains are stationary, regardless of the the distribution of the individual spike train, the probability distribution becomes Gaussian as the number of spike trains increase. The distribution function may then be expressed as:

$$f'(t) = \frac{1}{\sigma\sqrt{2\pi}} \exp \frac{-(t-\mu)}{2\sigma^2} \quad 3.20$$

where $\sigma^2 = \sum_{i=1}^N \sigma_i^2$ & $\mu = \sum_{i=1}^N \mu_i$

Dick & Meyer (1974), by simulation of the neural output of a chemoreceptor, showed that the variance of the signal alone from a nerve trunk may be used as an index of the nerve traffic. In summary, the

neural signals from the nerve trunk have the following characteristics: 1) the overall neural signal is the sum of the individual nerve firing fibres within the nerve trunk; 2) the firing of nerve fibres within the trunk are independent of each other; and, 3) due to the geometrical relationship of the nerve fibres and their distance from the electrode, each fibre activity adds with a weighting factor.

3.4 AN APPROACH TO THE ANALYSIS OF NERVE SIGNALS

One of the objectives in the analysis of the compound neural signals is to study such signals for their sensory and motor patterns. In this regard, the cross-correlation technique has been widely employed not only in physiology but also in communication problems, such as time delay estimations [Wozencraft and Jacobs, 1965; Van Trees, 1968]. In this study, besides the general cross-correlation technique, other methods that take into account the coherence function and signal-to-noise ratio have been employed to study sensory and motor patterns of compound neural signals recorded from two adjacent sites, as discussed below.

As shown in Chapter II (Section 2.4.3), compound signals recorded from a nerve trunk are contributed by both sensory and motor fibres. For the remainder of this thesis nerve signals are referred to as the compound neural signals.

A simplified diagram of the nerve cuff electrode and its signal components is shown in Fig. 3.5a and the equivalent signal flow diagram is shown in Fig. 3.5b. Let $x(t)$ be the neural signal recorded from the

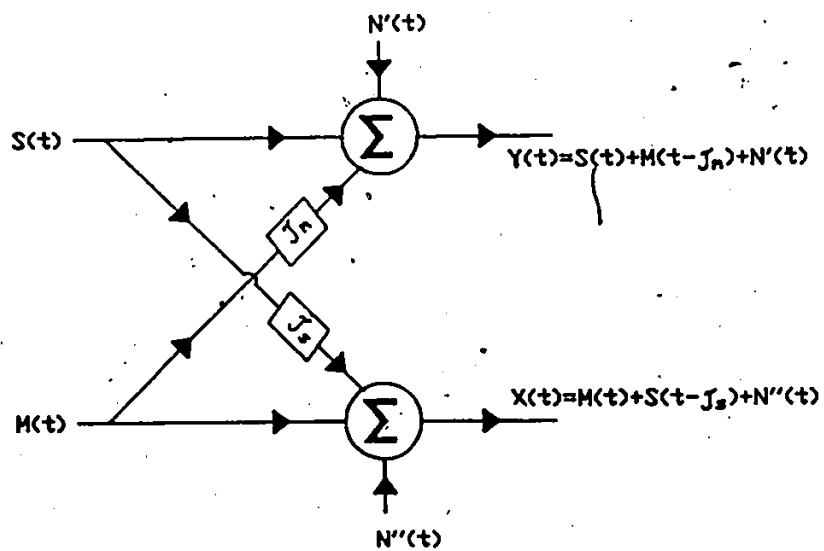
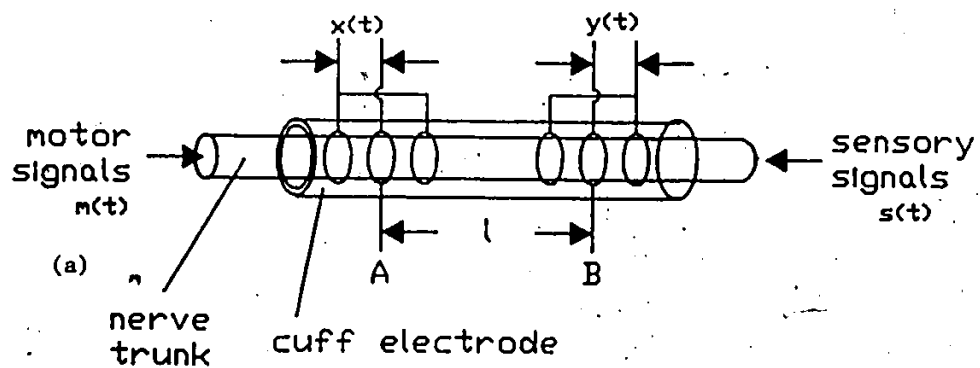


Figure 3.5 (a) A simplified nerve cuff electrode, (b) An equivalent signal flow diagram

proximal electrode at site A and $y(t)$ be the neural signal recorded from the distal at site B. The signals recorded from the two sites can then be expressed as :

$$x(t) = m(t) + s(t - \tau_s) + n_1(t) \quad 3.21$$

$$y(t) = s(t) + m(t - \tau_m) + n_2(t) \quad 3.22$$

where $m(t)$ is the signal contributed by motor fibres,

$S(t)$ is the signal contributed by sensory fibres,

τ_s is the time required for the sensory fibres to travel from point B to point A.

τ_m is the time required for the motor fibres to travel from point A to point B.

$n_1(t)$ & $n_2(t)$ are the recording noise at location A and B respectively.

The functional coupling between the two signal sources $x(t)$ and $y(t)$ and the transit time τ_s and τ_m as the signals travel from one receiver to another can be estimated by taking the cross-correlation between $x(t)$ and $y(t)$. i.e.

$$R_{xy}(\tau) = E [x(t)y(t+\tau)] \quad 3.23$$

$$R_{yx}(\tau) = E [y(t)x(t+\tau)] \quad 3.24$$

where $E [\]$ is the expectation operator

Expanding the above expression with equations 3.21 and 3.22,

$$R_{xy}(\tau) = E [m(t)s(t+\tau) + m(t)m(t-\tau_m + \tau) + m(t)n_2(t-\tau) + s(t-\tau_s)s(t+\tau) + s(t-\tau_s)m(t-\tau_m + \tau) + s(t-\tau_s)n_2(t+\tau) + n_1(t)s(t+\tau) + n_1(t)m(t-\tau_m + \tau) + n_1(t)n_2(t+\tau)] \quad 3.25$$

If n_1 and n_2 are uncorrelated measurement noises and $s(t)$ and $m(t)$ are uncorrelated events, then Eq. 3.25 simplifies to

$$R_{xy}(\tau) = E [m(t)m(t-\tau_m + \tau) + s(t-\tau_s)s(t+\tau)] \quad 3.26$$

If $\tau = \tau_m$ which is the time required for the motor signals to travel from A to B (Fig. 3.5) and the occurrence of one impulse is independent of another impulse then

$$R_{xy}(\tau_m) = E [m(t)m(t)] \quad 3.27$$

which is the expectation of the power of the motor signal.

Similarly by expanding Eq. 3.24 with Eq. 3.21 and 3.22

$$R_{yx}(\tau) = E [s(t)s(t-\tau_s + \tau) + m(t-\tau_m)m(t+\tau)] \quad 3.28$$

Again if $\tau = \tau_s$ and the occurrence of impulses in $m(t)$ is independent of each other then

$$R_{yx}(\tau_s) = E [s(t)s(t)] \quad 3.29$$

which is the expectation of the power of the sensory signals.

Hence, the cross correlation function may be used to indicate the average amounts of sensory and motor signals embedded in the measured neural signals. The properties and various techniques of estimating the cross correlation function are given in the following two sections.

3.5 THE PROPERTIES OF CROSS-CORRELATION

Consider two recorded nerve signals $x(t)$ and $y(t)$, both assumed to be continuous and stationary, then the means of $x(t)$ and $y(t)$ are

$$\mu_x = \lim_{T \rightarrow \infty} \frac{1}{T} \int_0^T x(t) dt ; \quad \mu_y = \lim_{T \rightarrow \infty} \frac{1}{T} \int_0^T y(t) dt \quad 3.30$$

The covariance function between $x(t)$ and $y(t)$ is

$$C_{xy}(\tau) = \lim_{T \rightarrow \infty} \frac{1}{T} \int_0^T (x(t) - \mu_x)(y(t+\tau) - \mu_y) dt \quad 3.31$$

If μ_x and μ_y are zero (by subtracting the means from the corresponding

original waveforms), the cross-correlation function of $x(t)$ and $y(t)$ is obtained from the covariance function as

$$R_{xy}(\tau) = \lim_{T \rightarrow \infty} \frac{1}{T} \int_0^T x(t)y(t+\tau) dt \quad 3.32$$

or in practical form

$$\hat{R}_{xy}(\tau) = \frac{1}{T-\tau} \int_0^T x(t)y(t+\tau) dt \quad 3.33$$

where $\hat{R}_{xy}(\tau)$ is an unbiased estimation of $R_{xy}(\tau)$, since the expected value for the estimate $\hat{R}_{xy}(\tau)$ is given by

$$\begin{aligned} E[\hat{R}_{xy}(\tau)] &= \frac{1}{T-\tau} \int_0^T E[x(t)y(t+\tau)] dt \\ &= \frac{1}{T-\tau} \int_0^T R_{xy}(\tau) dt = R_{xy}(\tau) \end{aligned} \quad 3.34$$

$R_{xy}(\tau)$ is always a real-valued function which may be either positive or negative. The absolute value of the cross correlation is bounded by its corresponding auto-correlation functions [Jenkins and Watts, 1968], that

is

$$|R_{xy}(\tau)| \leq R_{xx}(0)R_{yy}(0) \quad 3.35a$$

and

$$|R_{xy}(\tau)| \leq \frac{1}{2}(R_{xx}(0)+R_{yy}(0)) \quad 3.35b$$

where

$$R_{xx}(\tau) = \frac{1}{T-\tau} \int_0^T x(t)x(t+\tau)dt \quad 3.36a$$

$$R_{yy}(\tau) = \frac{1}{T-\tau} \int_0^T y(t)y(t+\tau)dt \quad 3.36b$$

The auto-correlation function is an even function and symmetrical about the ordinate at $\tau = 0$, i.e.

$$R_{xx}(\tau) = R_{xx}(-\tau) ; R_{yy}(\tau) = R_{yy}(-\tau) \quad 3.37$$

In the case of cross-correlation function, symmetry about the ordinate is displayed when x and y are interchanged. That is,

$$R_{xy}(\tau) = R_{yx}(-\tau) \quad 3.38$$

However $R_{xy}(\tau)$ is not in general the same as $R_{yx}(\tau)$. A typical cross-correlation function of $x(t)$ and $y(t)$ is shown in figure 3.6.

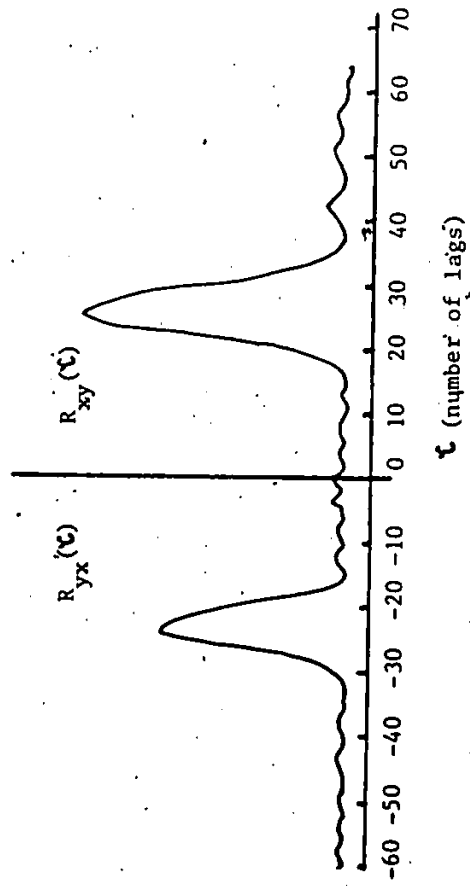


Figure 3.6 A typical wave shape of the cross-correlation of $x(t)$ and $y(t)$ (see also Fig. 3.5a & b)

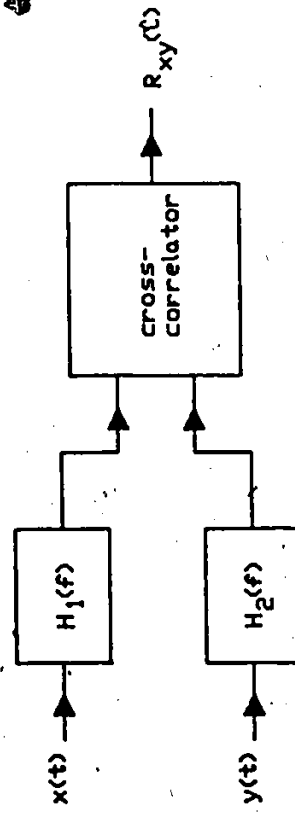


Figure 3.7 The pre-filtered cross-correlator

In order to improve the estimation of the cross-correlation and the time delay estimation, especially under low signal-to-noise ratio environment, it is desirable to filter $x(t)$ and $y(t)$ prior to the implementation of Eq. 3.33. As shown in Fig. 3.7, $x(t)$ and $y(t)$ may be prefiltered through $H_1(t)$ and $H_2(t)$ to yield $a(t)$ and $b(t)$ respectively. According to the Wiener-Khinchine theorem [Jenkins and Watts, 1968], the (cross) power spectral density and (cross-) auto-correlation function form the Fourier transform pair i.e.

$$G_{xy}(f) = 2 \int_{-\infty}^{\infty} R_{xy}(\tau) \exp(-j2\pi f\tau) d\tau \quad 3.39$$

$$R_{xy}(\tau) = \int_{-\infty}^{\infty} G_{xy}(f) \exp(j2\pi f\tau) df \quad 3.40$$

where $G_{xy}(f)$ is the cross spectrum of $x(t)$ and $y(t)$

When $x(t)$ and $y(t)$ are filtered (Fig. 3.7), the cross spectrum of the filtered outputs is

$$G_{ab}(f) = H_1(f)H_2^*(f)G_{xy}(f) \quad 3.41$$

where $*$ is the complex conjugate.

The cross-correlation function can then be obtained by taking the inverse Fourier transform of equation 3.41, i.e.

$$R_{xy}(\tau) = \int_{-\infty}^{\infty} \Omega_g(f) G_{xy}(f) \exp(j2\pi ft) df \quad 3.42$$

where $\Omega_g(f) = H_1(f)H_2^*(f)$

In practice, because of the limitation of data for analysis, only an estimate $\hat{G}_{xy}(f)$ of $G_{xy}(f)$ can be obtained. Hence,

$$\hat{R}_{xy}(\tau) = \int_{-\infty}^{\infty} \Omega_g(f) \hat{G}_{xy}(f) \exp(j2\pi ft) df \quad 3.43$$

Eq. 3.42 is the generalized correlation function between $x(t)$ and $y(t)$. The estimation of the cross-correlation can be optimized by the proper selection of the weighting factor $\Omega_g(f)$. The various algorithms of estimating the cross-correlation function are discussed below.

3.6. CROSS-CORRELATION ALGORITHMS

The prefilters, $\Omega_g(f)$, of Eq. 3.43 can be viewed as a window or weighting function applied to the cross-power spectrum before the inverse Fourier transform. The role of $\Omega_g(f)$ is to enhance the detection of the cross-correlation of $x(t)$ and $y(t)$ at the delay time τ_m and τ_s , by actually accentuating the signal passed to the correlator at those frequencies at which the signal-to-noise is the highest. The

selection of $\Omega_g(f)$ to optimize the estimation of the cross-correlation and the time delay has been studied by several investigators [Hannan and Thomson, 1973; Carter et al, 1973; Roth, 1971]. In this thesis, three type of algorithms are considered: the general cross-correlation (GCC), the smoothed coherency transform (SCOT), and the maximum likelihood (ML) estimation. Details of derivation of these algorithms are given in [Knapp and Carter, 1976; Jenkins and Watts 1968; Hannan and Thomson, 1973].

3.6.1 THE GENERAL CROSS-CORRELATION (GCC)

The general cross-correlation technique is the same as the basic cross-correlation function (Eq. 3.43) with the weight function equal to unity, that is

$$R_{xy}(\tau) = \int_{-\infty}^{\infty} G_{xy}(f) \exp(j2\pi f\tau) df \quad 3.44$$

3.6.2 The Smoothed Coherence Transform (SCOT)

In SCOT technique the weighting function is the reciprocal of the square root of the auto-spectra of $x(t)$, and $y(t)$, that is

$$\Omega_g(f) = \frac{1}{\sqrt{G_{xx}(f)G_{yy}(f)}} \quad 3.45$$

where $G_{xx}(f)$ and $G_{yy}(f)$ are the auto-power spectra of $x(t)$ and $y(t)$ respectively.

Then the cross-correlation with the SCOT weighting function is

$$R_{xy}^{(scot)}(\tau) = \int_{-\infty}^{\infty} \left[\frac{G_{xy}(f)}{\sqrt{G_{xx}(f)G_{yy}(f)}} \right] \exp(j2\pi f\tau) df \quad 3.46$$

The square of the term in the bracket of the above expression is known as the coherence function of $x(t)$ and $y(t)$ which is defined as

$$C_{xy}^2(f) = \frac{|G_{xy}(f)|^2}{G_{xx}(f)G_{yy}(f)} ; \quad 0 \leq C_{xy}^2(f) \leq 1 \quad 3.47$$

Some authors [Jenkins and Watts, 1968; Carter et al, 1973] called the above expression (Eq. 3.47) squared coherence function and the square root of Eq 3.47 as the coherency. In this thesis Eq. 3.47 is referred to as the coherence function. When $x(t)$ and $y(t)$ are linearly related at all frequencies, then $C_{xy}^2(f) = 1$. If $x(t)$ and $y(t)$ are completely unrelated at all frequencies, then $C_{xy}^2(f) = 0$. Because of the coherence term in the Eq. 3.46, it has come to be known as the Smoothed Coherence Transform. In general the coherence values lie between 0 and 1 depending on the amount of linearity and noise in the system between $x(t)$ and $y(t)$.

If $G_{xx}(f) = G_{yy}(f)$ then the SCOT is equivalent to the Roth

processor which estimates the impulse response of the optimum linear (Wiener-Hopf) filter [Roth, 1971].

3.6.3 The Maximum Likelihood (ML) estimation

Unlike the SCOT method which normalizes $G_{xy}(f)$ by the square root of $G_{xx}(f)$ and $G_{yy}(f)$, the ML method assigns the weighting function $\alpha_g(f)$ according to the signal-to-noise between $x(t)$ and $y(t)$ and normalizes $G_{xy}(f)$ with its magnitude [Hannan and Thomson 1971]. The signal-to-noise ratio, $\alpha(f)$, between $x(t)$ and $y(t)$ can be derived from the coherence function $C_{xy}^2(f)$ as given by [Bendat, 1978]

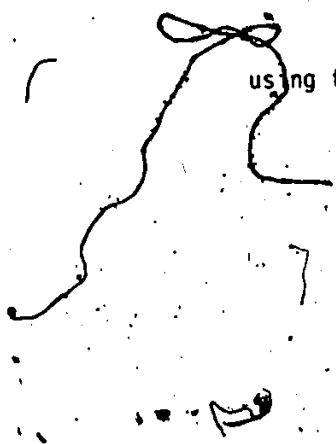
$$\alpha(f) = \frac{|C_{xy}(f)|^2}{1 - |C_{xy}(f)|^2} \tag{3.48}$$

and is a function of frequency.

The weighting function for the ML is then [Hannan and Thomson, 1971]

$$\alpha_g(f) = \frac{|C_{xy}(f)|^2}{(1 - |C_{xy}(f)|^2)} \frac{1}{|G_{xy}(f)|} \tag{3.49}$$

By substituting Eq. 3.49 into Eq. 3.43 the cross-correlation using the ML method is then



$$R_{xy}(\tau) = \int_{-\infty}^{\infty} \frac{|C_{xy}(f)|^2}{(1-|C_{xy}(f)|^2)} \exp(j\phi(f)) \exp(j2\pi f\tau) df \quad 3.50$$

$$\text{where } \exp(j\phi(f)) = \frac{G_{xy}(f)}{|G_{xy}(f)|} \quad 3.51$$

which is the phase spectrum of $x(t)$ and $y(t)$. From Eq. 3.51, it is easily seen that the ML cross-correlation function reaches its maximum value when the delay time τ reaches the sensory propagation time τ_s and motor propagation time τ_m , i.e., $\exp(j\phi(f)) \cdot \exp(j2\pi f\tau) = 1$. In other words, the ML method weights the phase of $x(t)$ and $y(t)$ according to the signal-to-noise ratio between them.

The procedures for implementation of the three algorithms are shown in the next chapter. The applications to various types of simulated and real signals under different signal-to-noise ratios are given in Chapter V.

CHAPTER IV

MATERIALS AND METHODS

4.1 INTRODUCTION

The characteristics of the neural signals and various algorithms for analyzing them were discussed in the previous chapter. In this chapter, the following subjects are described : (1) the materials and procedures for making various electrodes; (2) the implantation procedures; (3) instrumentation requirements; (4) the computer interface and programming; (4) consideration of the signal in the discrete form; and, (5) procedures for data analysis.

4.2 MATERIALS AND METHODS FOR MAKING VARIOUS TRANSDUCERS

Three types of transducers have been designed: (a) the cuff electrode, (b) the strain gauge, and (c) the bipolar electrode for neural activities, contractile activities and EMG respectively.

4.2.1 NERVE CUFF ELECTRODE

The first reported methods of implanting electrodes in autonomic

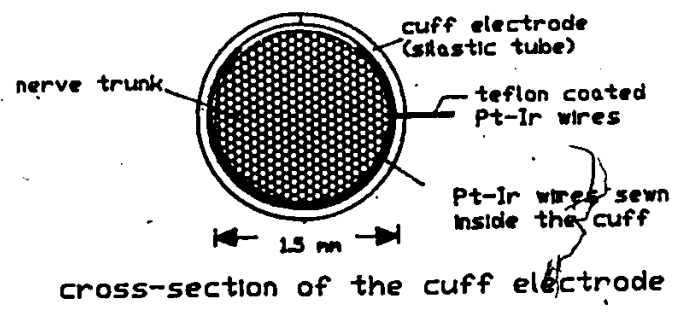
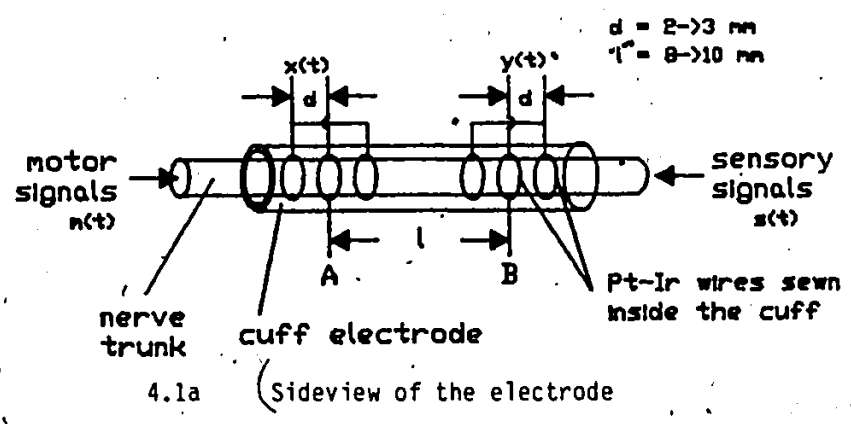
nerves chronically were from Cannon, 1933 and Vorobyov 1935. However their electrodes were designed for stimulation purpose only. Not until recently were methods of stable recording of neural activities in an awake animal reported [Stein, Pearson, 1978]. Their studies, however, were mainly based on nerves innervating skeletal muscles. With regard to the study of the autonomic nervous system in the control of the GI system in an awake animal, there are very few published reports [Miolan and Roman, 1978]. In this study, the shape and dimension of the nerve cuff electrode were made to fit the nerve trunk (Nerve of Latarjet) innervating the gastric system. The rationale for the design of the cuff electrode is given below :

As shown in Section 3.2.4.3 the dimensions of the cuff electrode are important as they affect the wave shape of the neural signal. In general the amplitude of the neural signal increases as the length of the restricted space (distance between the extreme leads) increases. However the amplitude saturates as the restricted space length reaches approximately 1 cm [Stein et al, 1975]. The diameter of the cuff electrode is also important with respect to the amplitude of the neural signal as well as the survival of the nerve fibres. If the cuff diameter is too large, the strength of the neural signals decrease drastically (inversely proportional to the square of the radius of the nerve cuff restricted space [Stein, 1975]), and allows connective tissue to grow between the electrode and the nerve trunk. In an ideal situation, the cuff should be in touch with the nerve trunk with minimal possible pressure. A tightly fitted nerve cuff may compress the nerve trunk, blocking the propagation of the neural signal and damaging some

nerve fibres. As discussed in the previous chapter (Section 3.2.3), a triphasic recording configuration between the centre lead and the two ends leads, which are connected together, permits a good rejection of environmental noises. For the gastric system, the diameter of the nerve of Latarjet ranges from 0.5 to 1.5 mm, the cuff diameter should be approximately 1.5 to 2.0 times the nerve trunk diameter [Hoffer et al, 1979].

4.2.1.1 MATERIALS AND PROCEDURES FOR MAKING THE CUFF ELECTRODE

The nerve cuff is made of a medical grade silastic tube (Dow Corning types 601 and 602). Each cuff consists of two sets of electrodes (Fig. 4.1a). The overall cuff length ranges from 1.3 to 1.5 cm with the inside diameter approximately 1.5 to 2.0 times the diameter of the nerve. For the cuff electrode, a teflon coated wire of 90% platinum and 10% Iridium (10Ir9Pt/49t Med. Wire Corp.) has been chosen for its flexible, strong, and corrosion-resistant properties. Approximately 3.5 cm of the teflon coat has been stripped off from the end of the wire and the exposed wire sewn inside the cuff in the form of three rings; this affords maximum surface contact with the nerve (Fig. 4.1b). The distances between the outside rings and the centre ring (2 mm) have been kept equal. The neural signals are recorded between the center and the outside rings which are connected together. The procedures for implanting the cuff electrode are given later in Section 4.3.



4.1b Cross-sectional view of the electrode

Figure 4.1 Diagram of the neural cuff electrode

4.2.2 CONTRACTILE FORCE TRANSDUCER (STRAIN GAUGE)

Strain gauges (SG) have been used by many researchers to monitor the GI system contractile activities. Even though the techniques for making the transducer vary [Bass and Wiley, 1972], the following rules are essential in making the transducer which will endure and accurately monitor the GI system contractile activities chronically : (1) the transducer must be compact and must have negligible mass to exert minimum influence on the tissue site being studied, (2) the backing materials for the SG must be biocompatible; and, the surface and the edges of the transducer must be smooth to decrease the growth of connective tissue, (3) the soldered joints between the SG and the wires must be well insulated to prevent seepage of fluids to the contacts, which can cause corrosion and breakage, (4) the transducer must be mounted securely on the gut surface such that the gut motility can be transmitted from the gut surface directly to the SG with minimal slippage between the gut surface and the gauge.

4.2.2.1 MATERIALS AND PROCEDURES OF MAKING THE CONTRACTILE FORCE TRANSDUCER

A complete contractile force transducer is shown in Figure 4.2. The strain gauge (Showa, model Y11-FA-5120) is a foil type and 5mm in length. After coating the SG with various backing materials (described later), the length increases to approximately 1cm. Each transducer

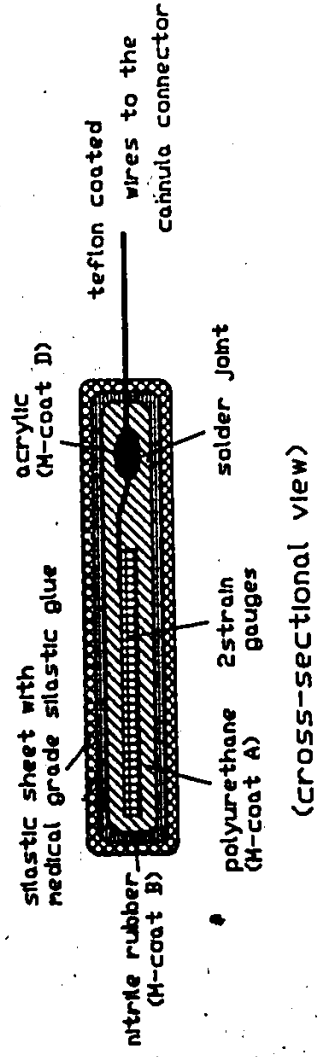
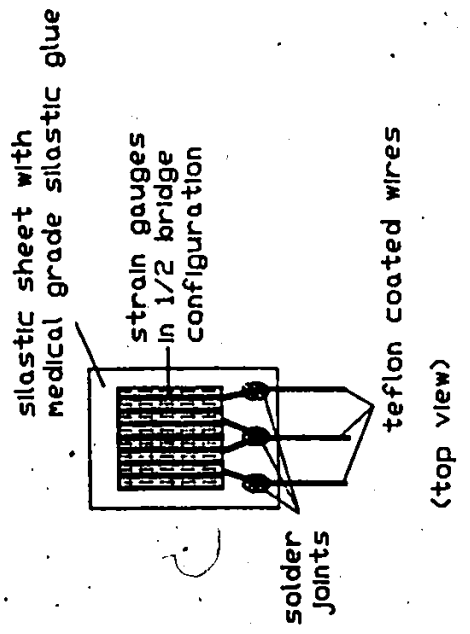


Figure 4.2 Structure of the contractile force transducer (Strain Gauge)

consists of two gauges which form the half bridge of the Wheatstone bridge. The wires that are soldered to the electrode are teflon coated for biocompatibility. The procedure for making the SG is given below:

- (i) Adhere two gauges together "back-to-back" to form a half bridge configuration with adhesives, such as epoxy-phenolic (M-bond 610 Intertechnology), or a thin layer of 'crazy glue'; the alignment of the gauge is important for ensuring that both gauges measure contractions from a given direction (e.g. longitudinal or circular).
- (ii) Solder the leads of the gauges to the teflon coated wires (Fig. 4.2); and ensure that the heat from soldering will not damage the gauges by temporarily clamping the gauges together with two thin metal plates as heat sinks during soldering. The teflon coat close to the solder joints must be pre-treated with tetra-edge. This allows the moisture proofing chemicals (to be applied later) to bond to the teflon surface.
- (iii) Apply a coat of acrylic coating (M-coat D, Intertechnology) around the soldered joint area for insulation and moisture proofing. Allow the coating to cure for about 24 hours at room temperature.
- (iv) Apply a thin even coating of polyurethane coating (M-coat A, Intertechnology), around the whole SG to provide a further moisture proof layer for the strain gauges; this coating normally requires 6-7 days to fully cure at room temperature but curing time can be shortened to 2-3 days by heating the SG with a heat lamp.
- (v) After M-coat A is completely cured, apply a coat of nitrile rubber

(M-coat B, Intertechnology) which provides bondability between the M-coat A and the outer coat.

- (vi) The most outer coats are implantable medical grade silastic sheets (Dow Corning Type 501-5) and cured silastic glue (Dow Corning Type 891) for suturing the unit on the stomach surface.

The above procedure provides a durable and chemically resistant contractile force transducer that readily responds to a variety of bending forces in a biological environment.

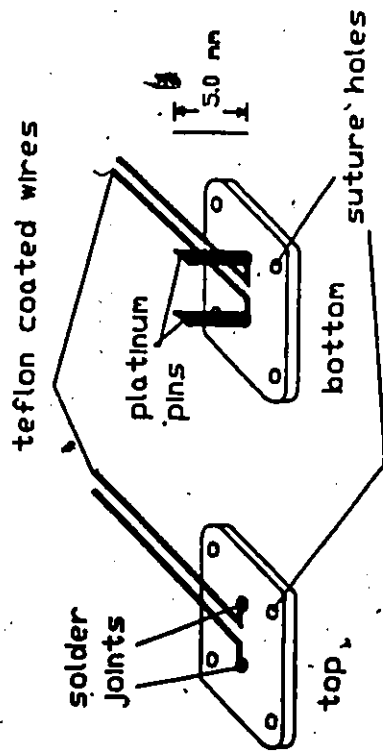
4.2.3 BIPOLAR EMG ELECTRODE

As discussed in Section 2.4.1.1 there are basically two types of EMG electrodes for recording GI EMG signals: the pin and wire electrodes. The advantages and disadvantages of both type of electrodes were also given in the same section. In this study, the pin electrode was used to measure EMG activities. The materials and procedure of making the pin electrode are given below.

4.2.3.1 MATERIALS AND PROCEDURES OF MAKING THE PIN ELECTRODE

The pin electrode is shown in Figure 4.3. It is made of platinum, Pt (0.508mm diameter) which is non-corrosive. The pins are 4mm in length, placed 4mm apart, and bonded in dental acrylics (Nu-Weld). The procedure for making the electrode is given below:

- (i) Cut two pieces of Pt wire to about 8mm and solder the ends with



The EMG Electrode

Figure 4.3 Diagram of the pin EMG electrode

- the tetra-edged teflon coated wires.
- (ii) Apply a coat of M-coat D around the solder joints for the same reasons as in preparing the force transducer.
 - (iii) After the M-coat D is completely cured, fit the two pins into the two small holes of a teflon mode. The distance between the two holes is 4mm. Prepare some dental acrylics and paste them around the pins in the mode. This step must be performed promptly because the acrylics solidify within 60 seconds.
 - (iv) After the dental acrylics are completely solidified, smoothen the pin electrode surfaces and edges of the pin electrode with a small file.
 - (v) Drill four holes in the corners of the electrode mounting for suturing the electrode on the stomach surface.

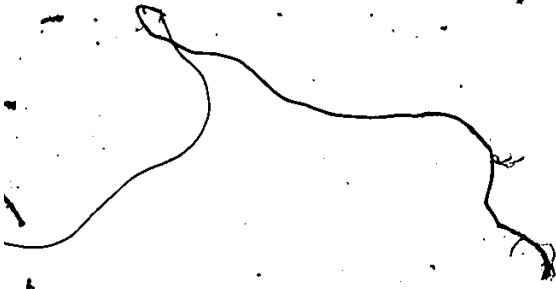
4.2.4 THE OVERALL CANNULA SYSTEM

All the wires from the various electrodes have been soldered to the pins (Amphenol, Relia-Tac 220S02) which are assembled into a 31 pin connector (Amphenol, 22211N31). The connector is firmly packed with dental acrylics and securely centered in the stainless steel cannula tube. Three layers of materials, viz.; cured medical grade silastic glue, beeswax, and silastic glue are packed inside the cannula tube to prevent corrosion of the soldered joints and to keep the wires secure within the tube.

4.3 IMPLANTATION

The cannula systems were implanted in five dogs to monitor the gastric and duodenal neural, electric and contractile signals. The implanted locations of the various electrodes are shown in Figure 4.4.

After a 24-hour fast the five healthy male dogs (approximately 35kg) were each anesthetized with 3 ml/kg solution of chloralose (2%), urethane (10%), and subsequently with 70 mg of sodium pentobarbital given intravenously. The operation was performed in an aseptic environment. The abdominal cavity was opened at the midline from the sternum to about 4 cm below the umbilicus. The connective tissues around the nerves were carefully removed with minimal damage to their blood supplies. The cuff electrodes were slit longitudinally and the corresponding nerves were placed carefully into them. The cuffs were then closed with sutures. The leads supplying the cuff electrodes were sewn on the surrounding tissue. This provided supports for the nerve cuff and prevented any pulls to the nerve trunk. The contractile force transducers were sutured to the gut wall so as to record circular contractile activities i.e. phasic or rhythmic contractions. The pin electrodes were implanted besides the strain gauges to monitor the corresponding local EMG.



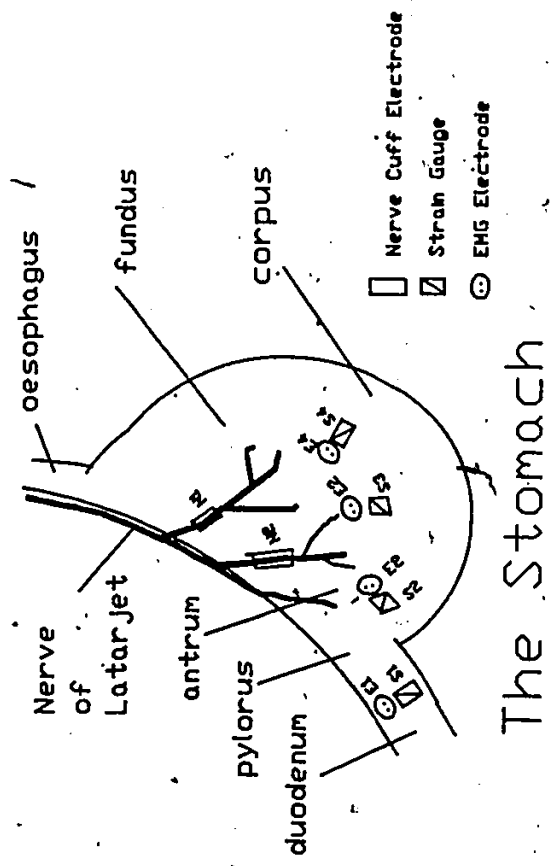


Figure 4.4 Location of the implantation site of the various electrodes

4.4 INSTRUMENTATION AND RECORDING

A block diagram of the instrumentation is shown in Fig. 4.5. The neural signals were stepped up approximately 25 times via transformers (Hammond 585F) which provided optimal input impedance matching and an increase in the signal-to-noise ratio [Stein et al, 1975]. The signals from the transformers were then amplified through an AC pre-amplifier (P15 Grass Inst.Co) with a gain of 1000 and a frequency range of 100-5k Hz. The neural signals were then recorded onto an 8 channel FM tape recorder (HP 3968A) at the maximum speed (15 inches/second) to realize a bandwidth of 5 kHz. The strain gauges and the pin EMG electrodes were connected to their corresponding couplers (coupler models 9853A and 9806A respectively) of an 8 channel dynograph recorder (Beckman R611). These various signals are thus available for amplification and filtering as desired later for analysis.

Besides recording neural signals, the nerve cuffs were also used to stimulate the nerve trunks at 10V, 6 pulse/second (using Grass S88 stimulator) to study the effect of nerve stimulation on EMG and contractile activities.

4.4.1 IMPEDANCE MEASUREMENT

The recordings were performed over a period of 10 to 15 weeks. Meanwhile the physical condition of the cuff electrode was followed by

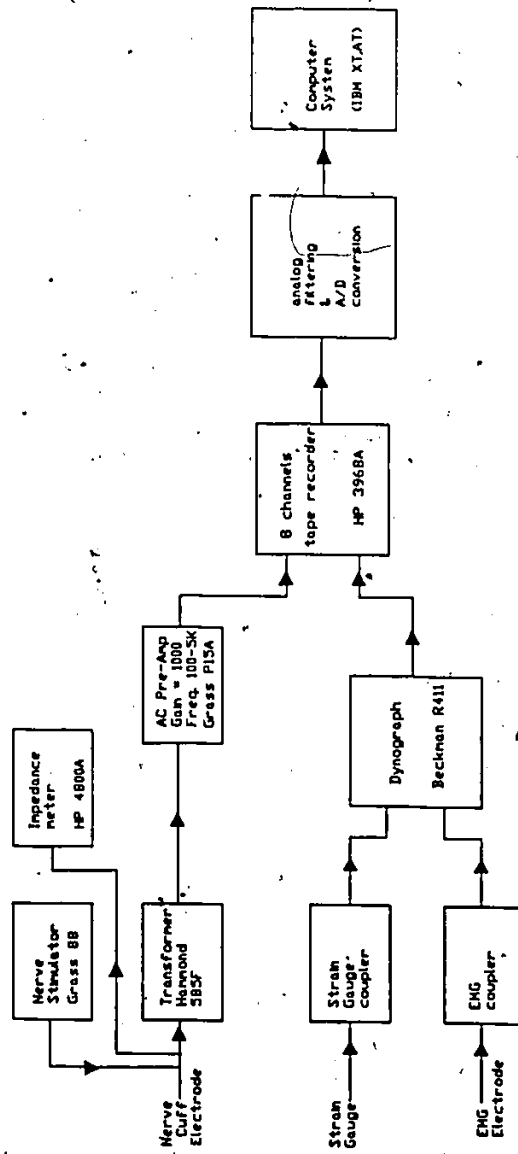


Figure 4.5 The block diagram of the recording instrumentation for this study

measuring the impedance of the electrodes by means of a HP 4800A vector impedance meter. After 12 - 15 weeks the cannula system was retrieved from the sacrificed animal and electron microscopic study of the nerve inside the cuff was performed to gauge the amount of damage to the nerve as described below.

4.4.2 ELECTRON MICROSCOPIC STUDIES

Four dogs with implanted cuffs and two control dogs without any cuff implantation were used for the electron microscopic study. The procedures of preparation of the nerve trunk for the EM studies are shown as follow: Dogs were anesthetized with sodium pentobarbital (30mg/kg i.v.). Portions of the nerves enclosed in the cuff and the corresponding segments of vagus from the control dogs were dissected and fixed by immersion with 2% glutaraldehyde in a 0.075 M Cacodylate buffer, pH 7.4, containing 4.5% sucrose and 1mM CaCl_2 for 2 hours at room temperature. Following fixation the pieces of nerve tissue were washed overnight at 4° C in Cacodylate buffer, containing 6% sucrose and 1.25 mM CaCl_2 , pH 7.4, postfixed with 2% OsO_4 (in 0.05M Cacodylate buffer, pH. 7.4) at room temperature for 90 minutes, strained en bloc with saturated uranyl acetate for 60 minutes, dehydrated in graded ethanol and propylene oxide and embedded in Epon 812. Sections were cut on a Sorvale (MT2 -B) ultramicrotome, stained for 3 minutes with a lead citrate and examined with a Philips 301 microscope at 60KV.

4.5 THE COMPUTER SYSTEM

The complete computer system for the acquisition and analysis of neural signals is shown in Fig. 4.6. The personal computer (PC) is an IBM PC/XT with a ten Mbyte hard disk, and a 360k floppy disk drive for the storage of data and programs. This microcomputer is 8088 microprocessor based with a math co-processor, 8087, installed to increase the calculation speed and precision. The text and graphics are displayed on a graphics monitor (Amdek 300A) with a high resolution graphic display card (Techmar Graphics Master). A multifunction card (AST 6-PackPlus) is installed in the system with its parallel port connected to the printer (Epson FX80) and the RS-232 serial port connected to the plotter (HP 7470A). This multifunctions card also allows the RAM size to be increased from 256K (maximum RAM size on the IBM system board) to 640K which is the maximum memory allowable for conventional usage. The extra serial port on the system allow the PC to have an option of communicating with a main frame computer (or other PCs) via a modem. The data acquisition is accomplished by a data acquisition board (Techmar Labmaster). The description of the data acquisition card and the corresponding software driver are given in the following section.

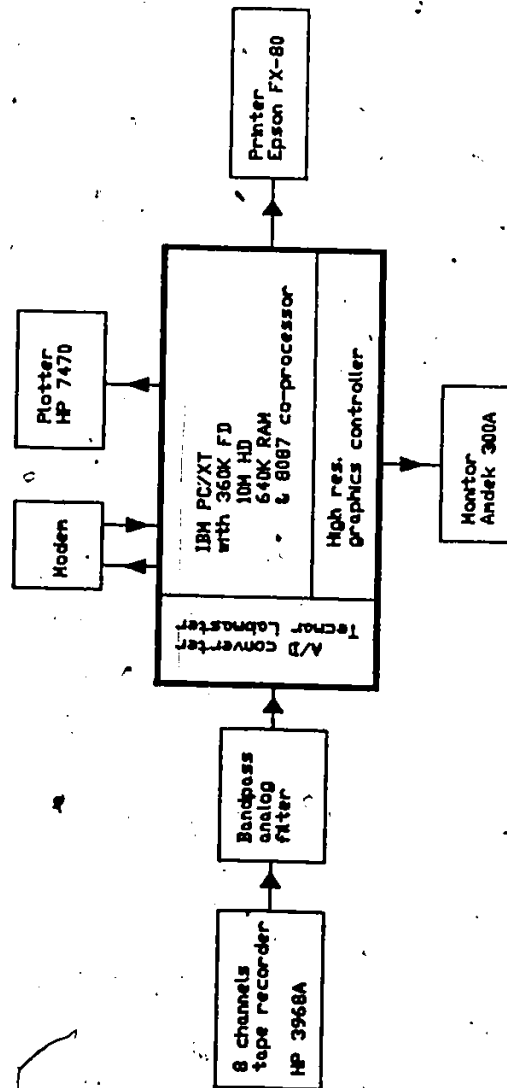


Figure 4.6 The computer system for this study

4.5.1 DATA ACQUISITION

Data recorded on the tape recorder are played back and digitized through the data acquisition board (Fig. 4.6). This board allows 16 single-ended or 8 differential inputs with 12 bits resolution at a maximum of 40 K Hz sampling rate (with proper software). The features of external trigger of A/D under the computer control, repetitive channel incrementing sampling, and the 5 independent 16 bits counters (AM 9513) are utilized for data acquisition. The detailed features of this acquisition board are given in the manufacturer's manual. The software and technical supports from the manufacturer, however, are inadequate for this study; the maximum sampling rate using the manufacturer's support software is approximately 10K HZ, and the maximum length of the data array is only 64k. The limitation of 64K data array length is due to the segmentational addressing architecture of the 8088 microprocessor which is the Central Processing Unit (CPU) of the computer. The detailed description of the mechanism of segment addressing is given in 8086/88 microprocessor literatures, such as The 8086 Book (Rector and Alexy, 1980) and The 8086 Family User's Manual (Intel, 1979). In order to overcome the problems, an assembly language program was written to drive the data acquisition board. This program can have a sampling rate of up to 40K Hz by using the overlap mode feature on the Labmaster, such that the A/D conversion process and the selection of next channel are performed simultaneously. As far as the 64K data array boundary problem is concerned, the extra-segment (ES)

register is used to index the data array instead. As soon as the incoming data reaches the 64K boundary, the ES register is incremented by 1000H (in HEX) for another 64K block. In this manner, the data array size is only limited by the amount of RAM size available on the system, which is 640k minus the system and program requirements. The flow diagram of the program is shown in Fig. 4.7.

After the digitization process, the data is converted into discrete numeric format. Various considerations in analyzing the discrete signal are discussed in the following sections

4.6 CONSIDERATIONS FOR DISCRETE OR DIGITAL IMPLEMENTATION

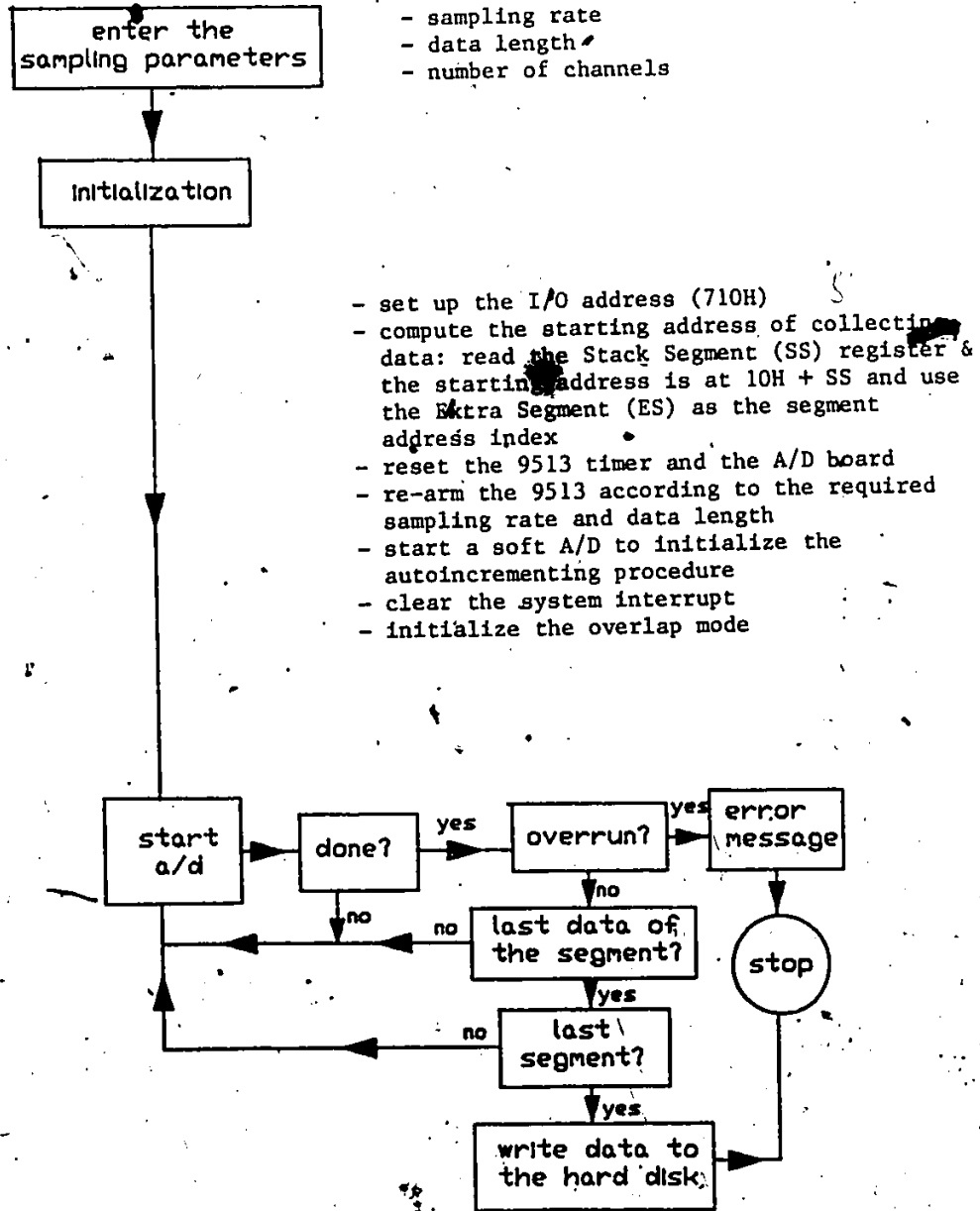
The theoretical background for the analysis of the neural signals has been given in the previous Section 3.4. All the mathematics considered are in continuous form and the integrals are performed over an infinite period of time. In practice, however, only a finite number of data points are available. The considerations of the neural signals in the discrete form are as follows

4.6.1 DISCRETE SIGNALS ANALYSIS

By digitization, a given signal $x(t)$ can be converted into discrete samples, that is

$$x_i = x(i\Delta t) \quad i=1,2,\dots,N \text{ number of samples} \quad 4.1$$

Figure 4.7 The flow diagram of the data acquisition program



where Δt is the sampling interval time

The autocorrelation of $x(t)$ and $y(t)$ (Eq. 3.36a,b) and their cross-correlation (Eq. 3.33) in the discrete form can be expressed as:

$$R_{xx}(k) = \lim_{N \rightarrow \infty} \frac{1}{2N+1} \sum_{i=-N}^N x_i x_{i+k} \quad 4.2$$

$$R_{yy}(k) = \lim_{N \rightarrow \infty} \frac{1}{2N+1} \sum_{i=-N}^N y_i y_{i+k} \quad 4.3$$

and

$$R_{xy}(k) = \lim_{N \rightarrow \infty} \frac{1}{2N+1} \sum_{i=-N}^N x_i y_{i+k} \quad 4.4$$

with $k = -n, -n+1, \dots, -1, 0, 1, \dots, n-1, n$

where N = number of data-samples

k = number of lags with n as the maximum

It was mentioned in Section 3.5 that since the (cross-) power spectral density (PSD) and the (cross-) correlation function form the Fourier Transform pair (Weiner-Khinchine theorem), the correlation functions can be obtained indirectly through the Fourier transform of the power (cross) spectra. The discrete Fourier transform (DFT) of a discrete time signal x_i can be defined as:

$$X(\Omega) = \sum_{k=-\infty}^{\infty} x_k \exp(-jk\Omega\Delta t) \quad 4.5$$

where Ω is a finite set of frequencies $\Omega_1, \Omega_2, \Omega_3, \dots, \Omega_m$, and $\Omega_i = 2\pi i/N\Delta t$

The cross-correlation discrete form of the Wiener-Khinchine theorem (Eq.

3.39, and Eq. 3.40) with a finite number of data samples, N can then be expressed as:

$$G_{xy}(\omega) = \frac{1}{N} \sum_{k=1}^N R_{xy}(k) \exp(-jk\omega\Delta t) \quad 4.6$$

and

$$R_{xy}(k) = \frac{1}{N} \sum_{i=1}^N G_{xy}(\omega) \exp(jk\omega\Delta t) \quad 4.7$$

From Equation 4.4, with a finite data samples, N , and with N much larger than the number of lag k , the cross-correlation function is

$$R_{xy}(k) = \frac{1}{N} \sum_{i=1}^{N-k} x_i y_{i+k} \quad 4.8$$

by substituting the above expression into equation 4.6, the cross-spectrum of x_i and y_i can be expressed as

$$G_{xy}(\omega) = \frac{1}{N} \sum_{k=1}^N \sum_{i=1}^{N-k} x_i y_{i+k} \exp(-jk\omega\Delta t) \quad 4.9$$

By using the factor $\exp(jk\omega\Delta t)\exp(-jk\omega\Delta t)=1$ and the definition of DFT (Eq 4.5) the above expression can be simplified to

$$G_{xy}(\omega) = \frac{1}{N} X^*(\omega) Y(\omega) \quad 4.10$$

where $*$ is the complex conjugate operator

Similarly the power spectrum density of x_i and y_i can be expressed as:

$$G_{xx}(\omega) = \frac{1}{N} X^*(\omega)X(\omega) = \frac{1}{N} |X(\omega)|^2 \quad 4.11$$

and

$$G_{yy}(\omega) = \frac{1}{N} Y^*(\omega)Y(\omega) = \frac{1}{N} |Y(\omega)|^2 \quad 4.12$$

The spectral-density estimation using Eq. 4.10, Eq. 4.11, and Eq. 4.12 are known as the periodogram spectral estimations. The factors affecting the estimation of the periodogram are discussed below.

4.6.2 PERIODOGRAM

The detailed properties of the periodogram can be found in the literature [Jenkins and Watts, 1968; Otneš and Enochsén, 1972]. For an ideal spectral density estimation, the bias and the variance of the estimated spectra $G_{xx}(f)$, $G_{yy}(f)$, and $G_{xy}(f)$ approach zero as the data length, N , approaches infinity. However for the periodogram, the spectral density estimation does not possess such converging statistical properties. For finite observations, the periodogram spectral estimation is biased. The amount of bias depends on the length of the data i.e., as the number of observations, N , increases the estimation bias decreases. Unfortunately, the variance of the estimated spectrum density does not decrease with the data length increase but remains

constant (Jenkins and Watts p.211, 1968; Fisher, 1929; Hannon, p.53, 1960). In other words, as the record length becomes longer, the frequency resolution increases, but the statistical reliability of the result is not increased (Bartlett, 1948, Jenkins and Watts, 1968). This inherent difficulty in the estimation of the periodogram can be overcome by subdividing the data into a number of segments, calculating the periodogram of each segment, and then averaging the periodogram from the k individual segments [Carter et al, 1973]. Bendat and Piersol (1973) have showed that theoretically this method can reduce the variance by k times, where k is the number of segments. Bartlett, (1948) and Carter, (1973) have shown that the estimation variance can be reduced further by overlapping the data segments. Details of overlapping segments are given in [Carter et al. 1973]. In this study, the periodogram spectral estimation was performed with 50% overlapped segmented data. Other factors such as sampling rate, record length, and truncation of data, also affect the estimation of the periodogram as discussed in the following sections.

4.6.3 SAMPLING RATE AND RECORD LENGTH

Through the process of digitization, the recorded neural signal is converted into discrete time sequences (Section 4.6.1). It is known that in order to retain all the signal information and avoid aliasing errors, it is necessary to sample the recorded signal at at least twice the maximum frequency component of the signal [Shannon 1948]. The frequency components of the neural signals depend on the length of the

cuff electrode and the propagation velocity of the neural signals along the nerve trunk [Stein et al, 1975]. Hoffer (1979) showed that neural signals with a propagation velocity of 60 meters per second (mps) with a cuff length of approximately 1 cm could have frequency components of up to 10K Hz. For the nerve of Latarjet, which consists of both myelinated and non-myelinated nerves [shown in next chapter], the conduction velocity ranges from 1 to 10 meters per second. With a cuff size of 0.4 cm, the maximum frequency component of the recorded neural signals could be up to approximately 2.5K Hz (as given later in Chapter VI).

Theoretically, sampling the signal at 5K Hz would be high enough to eliminate the aliasing problem for the signals which are band limited to 2.5k Hz. However, but it is advantageous to sample the signals at about four times the maximum frequency components of the signal for more accurate estimation of the cross-correlation function [Bendat 1978]. In this study, the sampling rate for the neural signal is 12.5k Hz with the signal band limited to 100-5K Hz. The cost of higher sampling rate is more computer storage and processing time. However, with the availability and low cost of RAM, and the fast process time using the 8087 math coprocessor, it is advantageous to sample at a higher rate in order to achieve more accurate results.

Bendat et al [1971] showed that the sampled length of data should be long compared to the fluctuation of the data time history, such that the short time averages will truly reflect average properties of the data and not just the random fluctuation of the time history. However as shown in Section 4.6.2 if the data length is too short, the estimated PSD will be biased and the spectrum will show loss of detail

i.e., will have broad frequency resolution. Detail of the bias and random errors inherent in the computation of correlation and spectral density functions are given in various references [Jenkins and Watts, 1968; Bendat and Piersol, 1971]. In this study, the data length of each segment is 256 points which with a sampling interval of 80 microseconds ($1/\text{sampling frequency} = 1/12.5\text{k}$) is 20.48 milliseconds. This duration is adequate for the study of conduction of the neural impulses between two nerve cuffs located 10mm apart.

4.6.4 TRUNCATION OF DATA

Each segment of data from a long record may be viewed as a multiplication of an infinitely long record by a rectangular or box car time window. This is also known as the truncation of data. This truncation in the frequency domain is equivalent to the convolution of the Fourier transform (FT) of the data $x(t)$ and that of the rectangular window. Hence the power spectrum density obtained from a truncated finite length of data is distorted. This undesirable distortion, known as the side-lobe effects or leakage, may be reduced by modifying the box car function in the time domain known as windowing. The design and selection the window function depends on the primary objectives of the windowing, such as the width of the main lobe, and the level of the side lobes of the window spectrum desired. Details of the design of various windows are given in numerous textbooks. [Oppenheim and Schaffer, 1975; Jenkins and Watts 1968; Otnes and Enochson, 1972]. In this study, the Hamming window function is employed to reduce the side lobe effects, the

window is given by

$$w_i = 0.54 + 0.46 \cos\left(\frac{\pi i}{NQt}\right) \quad i \leq NQt \quad 4.13$$

where NQt is the length of the window which is equal to the length of the data sequence, i.e. $NQt = 256$.

The implementation of the above in analyzing the neural signals is discussed in the next section.

4.7 PROCEDURES FOR ANALYZING THE DATA

The procedures for analyzing the recorded neural signals are given in block diagram Figure 4.8 and described below:

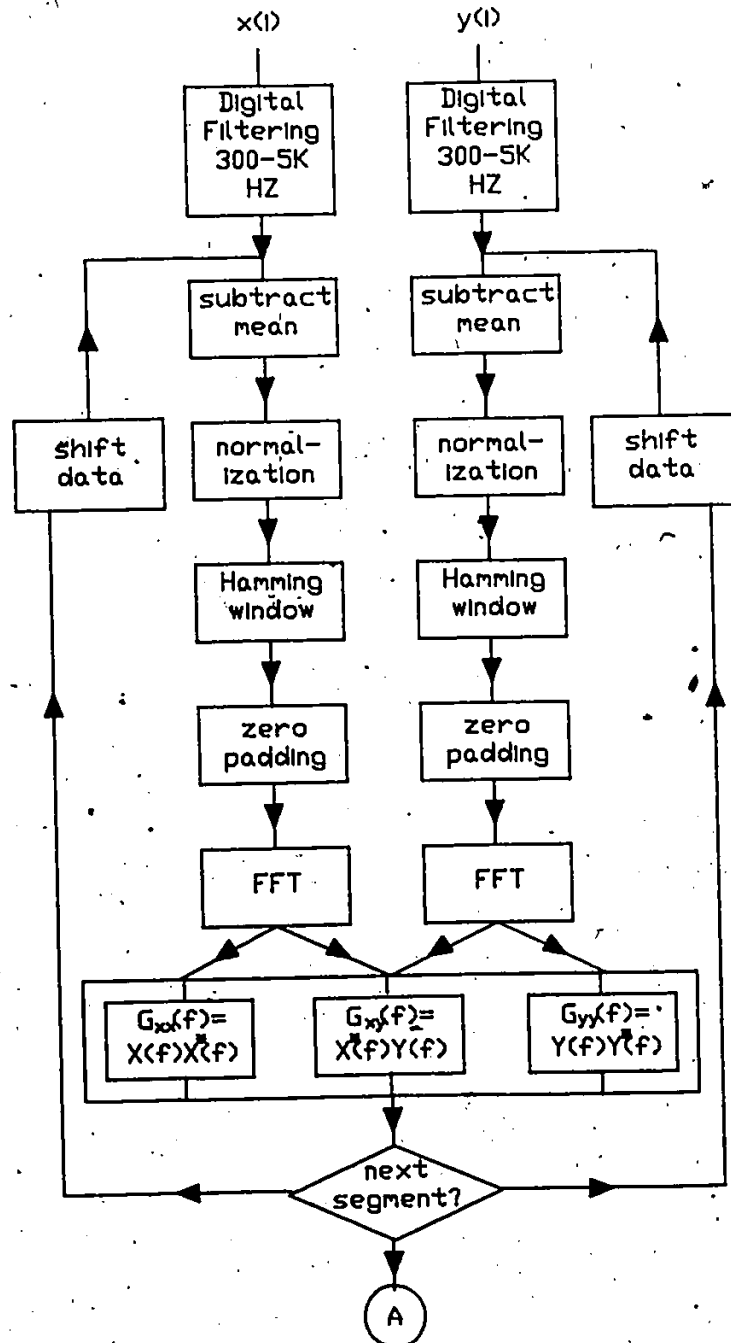
4.7.1 PREPARATION OF DATA

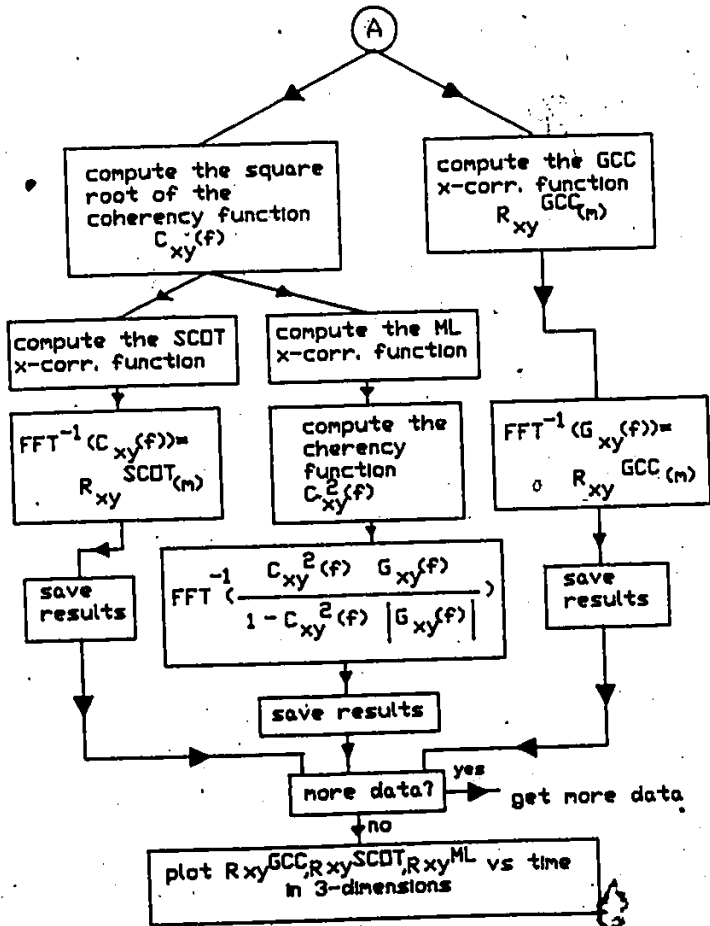
Two types of data i.e., simulated data and recorded neural signals, are prepared for the simulation studies and the neural signal analysis respectively, as described below.

4.7.1.1 SIMULATED DATA

In order to investigate the characteristics of the three cross-correlation algorithms discussed in Chapter III, three kinds of data are simulated for the model given in Figure 3.5b. They are Gaussian white

Figure 4.8 The block diagram of the procedures of the analysis of the neural signals





noise (GWN), sinusoidal signal, and simulated neural impulses. All the GWN sequences generated for the inputs (sensory, and motor), and the additive noises ($n'(t)$, $n''(t)$) are checked to ensure that they are mutually independent. The frequency of the sinusoidal signal is 1.5k Hz. The duration of the neural impulses is 1 msec with random duration between the impulses. The time delay parameters, k_s and k_m , are both 15 (1.2 msec) for the sinusoidal inputs, and 20 (1.6 msec) and 15 (1.2 msec) respectively for the GWN and simulated impulses.

4.7.1.2 RECORDED NEURAL SIGNALS

After digitization (Section 4.6), the two channels of digital data are stored in binary format of two bytes in two's complement. The data are arranged in alternative mode, i.e. each 2 bytes of the first channel is followed by 2 bytes of the second channel. Each data file is 524,288 bytes in length which is approximately 20.97 seconds of neural signals.

4.7.2 DIGITAL FILTERING

The digital signals are filtered with a second order bandpass filter with the cut-off frequencies of 100 - 5K Hz. This step ensures that the aliasing problem will not occur.

4.7.3 SUBTRACT MEANS

The means of each segment of data are computed and subtracted from the original data, that is

$$x_i := x_i - \mu_x \quad 4.14$$

$$\text{where } \mu_x = \frac{1}{N} \sum_{i=1}^N x_i \quad 4.15$$

$:=$ is used to imply an update of the value on the right hand side of the symbol.

If the mean values of the sequences before the PSD estimation are not zero, then the PSD function will exhibit a large peak (theoretically infinite) at the zero frequency which will then distort the estimation at other frequencies near the zero frequency, often known as aliasing at dc.

4.7.4 NORMALIZATION

After subtracting the means from the data segment, the sequences are then normalized with respect to their corresponding standard deviation, that is

$$x_i := \frac{x_i}{\sigma_x} \quad 4.16$$

$$\text{where } \sigma_x = \sqrt{\frac{1}{N} \sum_{i=1}^N x_i^2}, \quad 4.17$$

which is the standard deviation of the mean-removed sequence x_i .

4.7.5 WINDOWING

The normalized data sequences are then multiplied with a Hamming window to reduce the leakage of the PSD estimation. This is expressed as

$$x_i := x_i w_i \quad 4.18$$

where w_i is the window function given by Eq. 4.13

4.7.6 ZERO PADDING

This step serves to eliminate the circular effect error in calculating correlation functions at the expenses of the extra storage in the FFT computation [Bendat and Piersol, 1980]. This is achieved by padding zero data values to the end of the data sequences. In other words, a new data sequence of length $2N$ is created such that

$$\begin{aligned} x_i &:= x_i & 1 \leq i \leq N \\ &:= 0 & N < i \leq 2N \end{aligned} \quad 4.19$$

where N is the data length which is 256.

This padding with zero has no deleterious effects on the spectral waveshape other than requiring more data storage location during the FFT computation.

4.7.7 FFT COMPUTATION

The FFT $X(\omega)$ and $Y(\omega)$ of both channel one x_i , and channel two y_i respectively are computed.

4.7.8 PSD COMPUTATION

The PSD of $x(\omega)$, $y(\omega)$, and the cross-spectrum of $x(\omega)$ and $y(\omega)$ are computed, that is

$$G_{xx}(\omega) = \frac{2a}{n_d T} \sum_{j=1}^{n_d} x_j(\omega) x_j^*(\omega) \quad 4.20$$

$$G_{yy}(\omega) = \frac{2a}{n_d T} \sum_{j=1}^{n_d} y_j(\omega) y_j^*(\omega) \quad 4.21$$

and

$$G_{xy}(\omega) = \frac{2a}{n_d T} \sum_{j=1}^{n_d} x_j^*(\omega) y_j(\omega) \quad 4.22$$

where n_d is the number of data segments = 39
 a is the scaling factor for using Hamming window
 $a = \sqrt{8/3}$
 T is the data length = 256

The loop formed by Sections 4.7.3 and 4.7.8 is repeated until the number of data segments reaches 39. Each time the loop starts at Section 4.7.3, the data pointer shifts to half of the data length i.e., 128 points. This provides a 50% segment overlapping.

4.7.9 COMPUTATION OF THE GENERALIZED CROSS CORRELATION (GCC)

The cross-correlation, using the general method, GCC is obtained by taking the inverse FFT of the cross-spectrum $G_{xy}(k)$ as Equation 4.22. The results obtained are a bias estimation of the cross-correlation function. An unbiased estimate of the cross-correlation over the range $0 \leq k \leq N$ is given by

$$R_{xy}^{GCC}(k) := \frac{N}{N-k} R_{xy}^{GCC}(k) \quad 4.23$$

4.7.10 COMPUTATION OF THE COHERENCE FUNCTION

From the results obtained in 4.7.8, the coherence function is computed as

$$C_{xy}^2(\omega) = \frac{|G_{xy}(\omega)|^2}{G_{xx}(\omega)G_{yy}(\omega)} \quad 4.24$$

4.7.11 COMPUTATION OF THE SMOOTHED COHERENCE TRANSFORMATION (SCOT)

The cross-correlation function using the SCOT method is obtained by taking an inverse FFT of the square root of the coherence function (Eq. 4.24), that is

$$R_{xy}^{SCOT}(k) = \frac{1}{N} \sum_{i=1}^N C_{xy}(i) \exp(jk\Omega t) \quad 4.25$$

where $\Omega = 2\pi/N\Delta t$

An unbiased estimate of $R_{xy}^{SCOT}(k)$ over the range of $0 \leq k \leq N$ is

$$R_{xy}^{SCOT}(k) := \frac{N}{N-k} R_{xy}^{SCOT}(k) \quad 4.26$$

4.7.12 COMPUTATION OF THE SIGNAL-TO-NOISE RATIO

From the coherence function obtained in Eq. 4.24, the S/N ratio between x_i and y_i , $\alpha(\Omega)$, can be obtained by

$$\alpha(\Omega) = \frac{\sqrt{C_{xy}^2(\Omega)}}{1 - \sqrt{C_{xy}^2(\Omega)}} \quad 4.27$$

4.7.13 COMPUTATION OF THE MAXIMUM LIKELIHOOD (ML)

Using the results obtained from Eq. 4.22 and Eq. 4.27, the ML estimation of the cross-correlation is computed by taking the inverse FFT of the S/N ratio function divided by the magnitude of the cross-spectrum and multiplied by the cross-spectrum, that is

$$R_{xy}^{ML}(k) = \frac{1}{N} \sum_{i=1}^N \frac{\alpha(i) G_{xy}(i)}{|G_{xy}(i)|} \exp(jk\Omega t) \quad 4.28$$

where $\Omega = 2\pi/N\Delta t$

Again an unbiased estimate of $R_{xy}^{ml}(k)$ over the range of $0 \leq k \leq N$ is

$$R_{xy}^{ML}(k) := \frac{N}{N-1} R_{xy}^{ML}(k) \quad 4.29$$

This whole procedure is repeated up to five data files which is approximately 52 seconds of continuous neural signals.

4.8 DISPLAY OF RESULTS

In order to illustrate the relationship of the sensory and motor activities with respect to the corresponding contractile and EMG activities, it is important to be able to display a series of cross-correlation functions from a long sequence of neural signals. An interactive 3-D graphic was written in Pascal language to display the cross-correlation functions of the neural signal. This program takes into account rotations, projections, perspectives, hidden-line-removal, magnifications, distortions, and labelling. The orientation and other parameters for the 3D display can be adjusted interactively by using the cursor keys and other keys of the keyboard. A plotter driver routine is also written to plot the graphs on the plotter (model HP 7470A)

The results of the simulation studies and the analysis of the recorded neural signals are discussed in the next chapter.

CHAPTER V

RESULTS: SIMULATED SIGNALS

5.1. INTRODUCTION

The theoretical backgrounds and the implementation of the three algorithms i.e., GCC, SCOT, and ML have been discussed in Chapters III and IV respectively. In this chapter, the performance of the three algorithms are evaluated using three different simulated signals. The model for the simulation of the compound neural signal components was given in Chapter III, section 3.4, (Fig. 3.5b). The simulation details and the results are given in the following sections.

5.2. SIMULATION DETAILS

The three different types of signals used in simulation are Gaussian white noise (GWN), sine wave (SINE), and simulated triphasic neural impulses (IMP). The GWN has been bandlimited to 100 Hz - 5 K Hz. Four such data sequences have been generated by means of random number generator. All the sequences are checked to ensure that they are mutually independent. Two of the GWN sequences have been used to simulate the electrodes recording noise, $n_1(t)$ and $n_2(t)$, whereas the

other two GWN data sequences simulate the sensory signal, $s(t)$, and motor signal, $m(t)$, respectively. The SINE data sequences for the sensory, and motor signals are both 1.5 KHz sinusoidal. The simulated neural impulse sequences are triphasic and the period between impulses has been randomized.

The signal sequences are then scaled to obtain the desired signal-to-noise (SNR) between the signals ($s(t)$, and $m(t)$), and the noise sequences ($n_1(t)$, and $n_2(t)$), respectively (Fig. 3.5). In this study, SNRs of approximately 10, 7.5, 5.0, 2.5, 1.0, 0.5, 0.33, 0.25, 0.2, 0.17, 0.14, 0.13, 0.11, and 0.1 are considered. The corresponding values in dB scales are 20.0, 17.5, 13.98, 7.96, 0.0, -6.02, -9.54, -12.04, -13.98, -15.56, -16.90, -18.06, -19.09, and -20.0.

A total of 20 trials have been performed for each SNR. Each trial processes 20 segments of 256 points per segment data sequence. The time delay at which the cross-correlation is at maximum is taken as the estimated peak location. The peak value is at least two times the standard deviation of the estimated cross-correlation function [Bandet, 1978]. In order to avoid bias in estimating the standard deviation of the cross-correlation and the peak location, the estimated cross-correlation functions within ± 10 from the peak locations are not considered in the calculation of the standard deviation, and the peak locations that fall outside the range ± 15 are omitted in calculating the average estimated peak locations. Since there are two estimated peak locations, k_s and k_m corresponding to the sensory and motor sequence respectively, the average deviations of the two peak locations are calculated. In this fashion, 20 estimates of the cross-correlation are

obtained for each of the SNRs. The estimated cross-correlation functions from the three algorithms are plotted as a function of the number of lags and the various SNRs. The left of the zero lags correspond to the sensory components and to the right of the zero lags correspond to the motor components. For the simulation with the GWN as the inputs for the sensory, $s(t)$, and motor $m(t)$ signals, the delay times for the sensory components, k_s , and the motor components, k_m are both set at 15. For the simulation with SINE and IMP as sensory and motor inputs, the delay times for the sensory components, k_s and the motor components, k_m , are set at 20, and 15 respectively. The results of the simulation are discussed in the following sections.

5.3 SIMULATION WITH THE GAUSSIAN WHITE NOISE (GWN)

The average of the estimated peak values of the cross-correlation function by the three methods (GCC, SCOT and ML) are shown in Fig. 5.1. The estimated peak values by the SCOT method are approximately the same as those by the GCC method except when the SNR falls below -12dB. The estimated peak values by the ML method are however lower than those obtained from GCC and SCOT.

The standard deviation of the estimated cross-correlation function (Fig. 5.2) in GCC decreases only slightly, whereas in SCOT the standard deviation increases by about the same amount as the decrease in SNR. In ML method, the standard deviation decreases with greater amount as the decrease in SNR.

The average deviation of the estimated peak locations from the

actual peak locations (Fig. 5.3) show that when the SNR is greater than -2.5dB, all three algorithms provide accurate locations of the cross-correlation peak. However as the SNR decreases, the average deviation of estimating the peak location obtained from all three algorithms increases. The deviations obtained using the GCC and ML method are less than those obtained from the SCOT method. As the SNR falls below -15 dB however, the deviation of the SCOT method approaches that of the GCC method.

The cross-correlation functions vs. SNRs of the three algorithms of one of the trials are shown in Figs. 5.4 to 5.6. Note that, for the GCC method, the peaks are wider, and the variances are higher than by the other two methods (Fig. 5.5). For the SCOT and ML methods, the peaks are narrower. The variance of the SCOT cross-correlation function is lower than that by the GCC method but not as low as the ML method (Fig 5.5). For the ML method, when the SNR is greater than 0 dB, there are four peaks (Fig. 5.6 a,b). The two extra peaks are located at $2k_m + k_s$ ($2 \cdot 15 + 15 = 45$) and $2k_s + k_m$ ($= 45$) on the +lag (motor) and -lag (sensory) sides respectively. This suggests that, for the ML method, the estimation of the cross-correlation of the sensory components is complicated with the presence of the motor components and vice versa. Similar results have been obtained with the SINE and IMP data sequence as will be shown later in section 5.4 and 5.5. Since the two extra peaks occurs only in the ML method, the problem is clearly due to the ML weighting function ω_m . More discussion on this subject will be provided later in the discussion Chapter (Chapter VII).

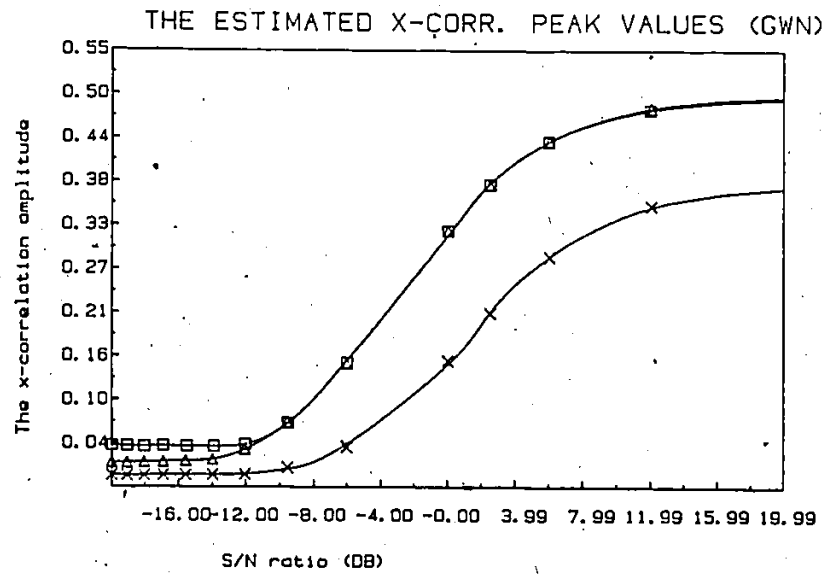


Fig 5.1 The average estimated cross-correlation peak values using the three estimation algorithms: GCC (□), SCOT (△), and ML (×) with GWN as the inputs. When the SNR is greater than -12 dB, the estimated cross-correlation peak values obtained from the SCOT method are approximately equal to those obtained by the GCC method. When the SNR is less than -12dB, the estimated peak values in the SCOT method are somewhat less than those obtained by the GCC method. The estimated peak values by the ML method are, less than those by both the GCC and SCOT methods.

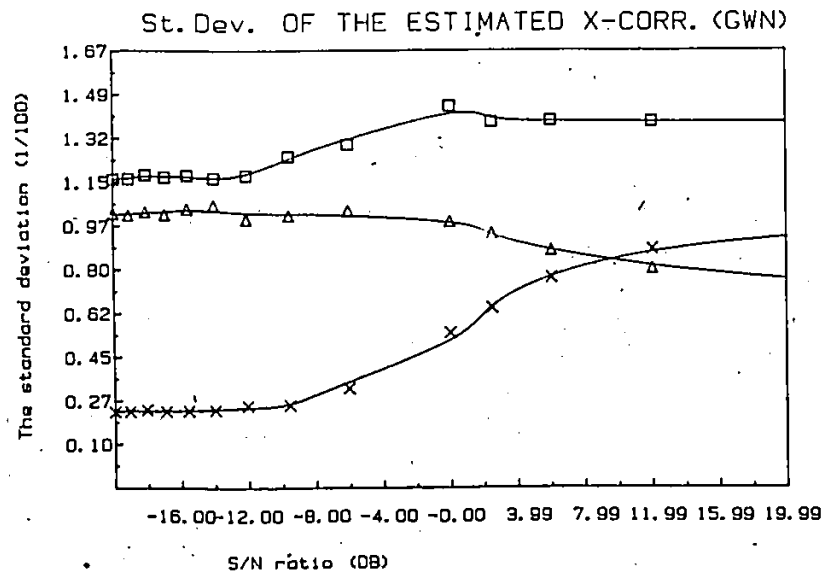


Fig 5.2 The standard deviation of the estimated cross-correlation function using the three estimation algorithms: GCC (□), SCOT (△), and ML (×) with GWN as the input. As the SNR decreases, the standard deviation of the estimated cross-correlation function in the GCC method decreases slightly, whereas in the SCOT, the standard deviation increased slightly. For the ML method, the standard deviation decreased with greater amount as the SNR increases.

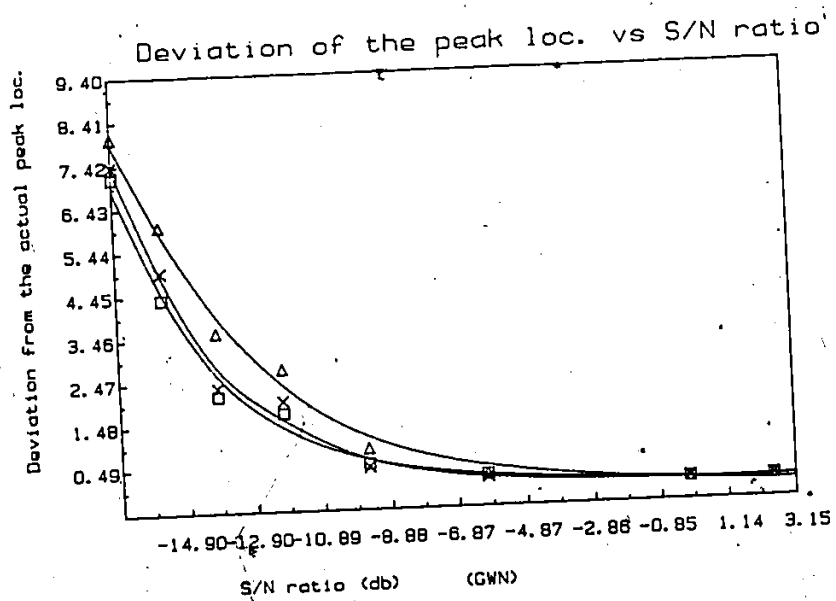


Fig 5.3 The average deviation of the estimated peak locations from the actual peak location. GCC (□), SCOT (Δ), ML (X). When the SNR is greater than -2.5 dB, all three algorithms can accurately locate the cross-correlation peaks. However as the SNR decreases, the average deviation of estimating the peak location by all three algorithms increases. The average deviation obtained by the GCC and ML methods are less than those obtained by the SCOT method.

Fig 5.4a,b The estimated cross-correlation as a function of number of lags and SNRs obtained from the GCC method with GWN as the input data. Fig 5.4b is the reverse view of Fig 5.4a. The SNRs for Fig 5.4a in the db scale are 20.00, 17.50, 13.98, 7.96, 0.00, -6.02, -9.54, -12.04, -13.98, -15.56, -16.90, -18.06, -19.09, -20.00 db. The peak locations for both sensory and motor sequences are at lag 15.

Simulation with noise+noise (GCC)

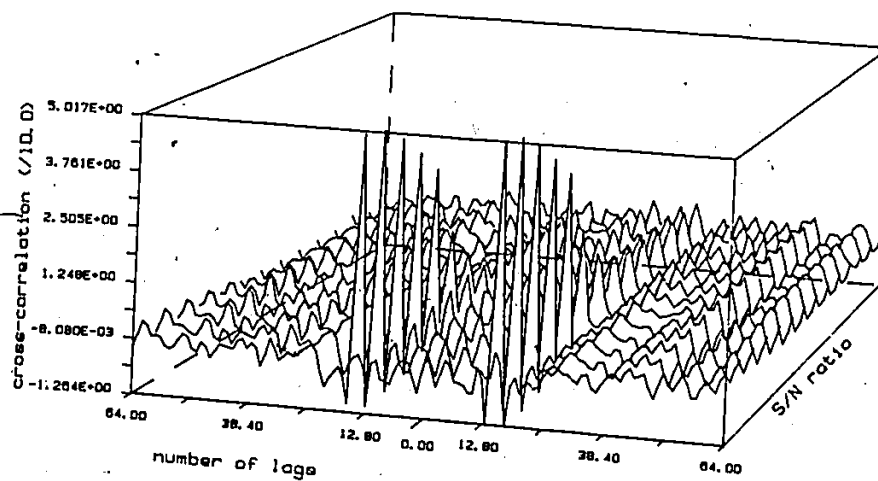


Fig. 5.4a

Simulation with noise+noise (GCC)

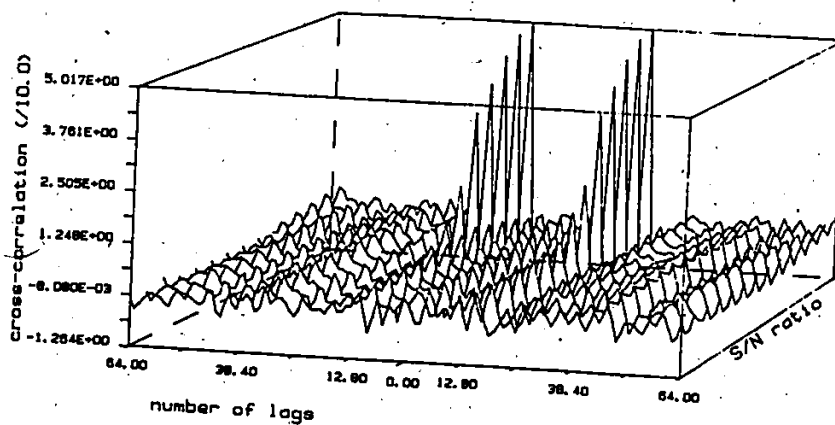


Fig. 5.4b

Fig 5.5a,b The estimated cross-correlation as a function of number of lags and SNRs obtained from the SCOT method with GWN as the input data. Fig 5.5b is the reverse view of Fig 5.5a. The SNRs scales are the same as that of Fig 5.4a,b.

Simulation with noise+noise (SCOT)

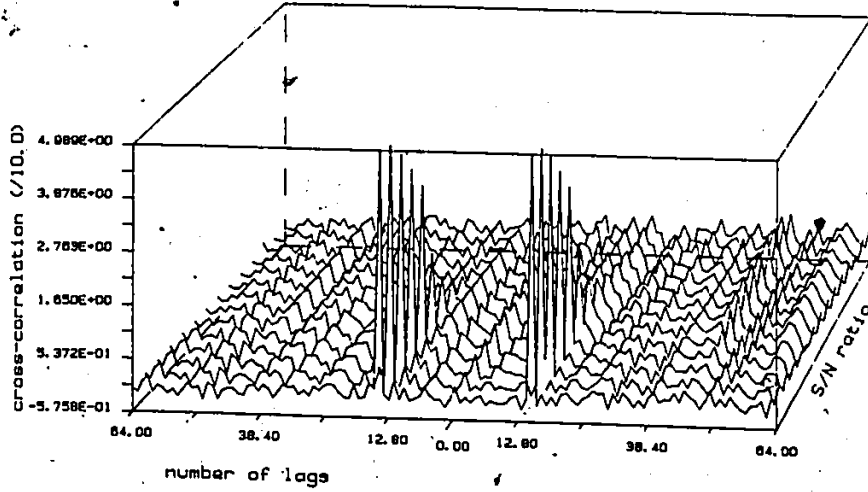


Fig 5.5a

Simulation with noise+noise (SCOT)

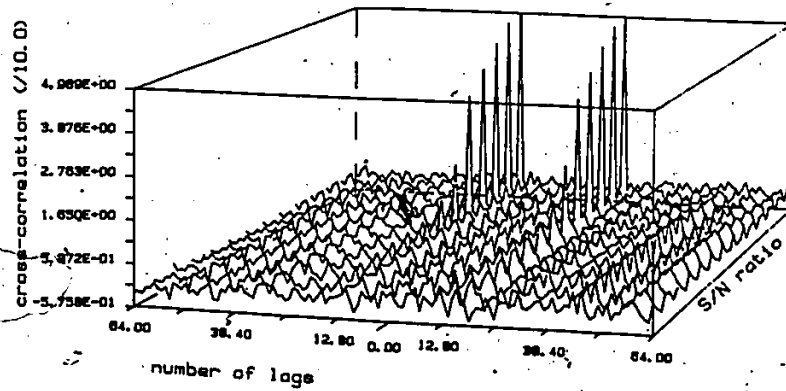


Fig. 5.5b

Fig 5.6a,b The estimated cross-correlation as a function of number of lags and SNRs obtained from the ML method with GWN as the input data. Fig 5.6b is the reverse view of Fig 5.6a. The SNRs scales are the same as that of Fig 5.4a,b.

Simulation with noise+noise (ML)

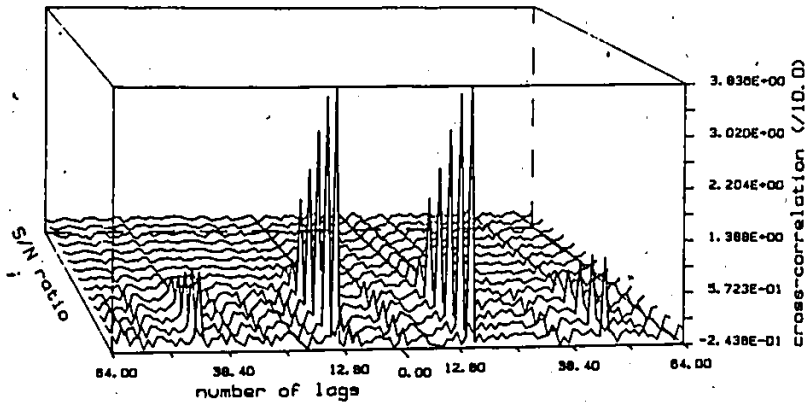


Fig 5.6a

Simulation with noise+noise (ML)

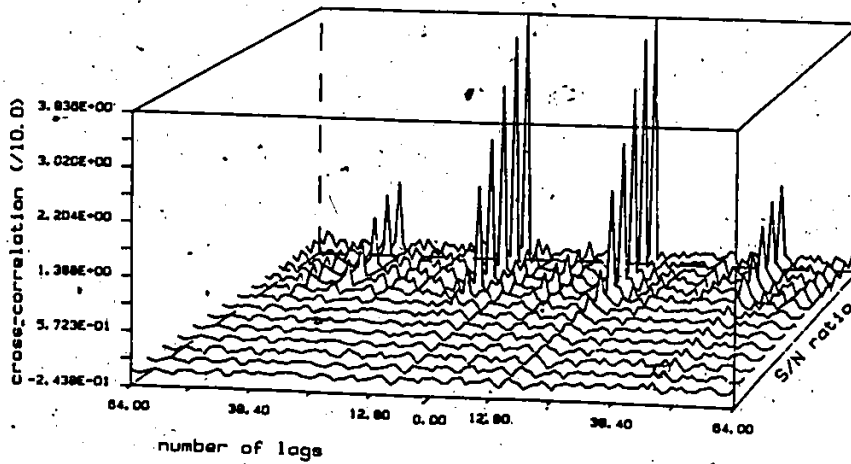


Fig. 5.6b

5.4 SIMULATION WITH SINE WAVE (SINE)

Two sine wave data sequences of 1.5 KHz are used as the sensory, $s(t)$ and motor, $m(t)$ inputs for the simulation model (Fig 3.5b). The waveshape and the PSD of the data sequences $x(i)$ after corrupting the sinewave with GWN data sequence, are shown in Fig. 5.7 and Fig. 5.8 respectively.

The peak values of the estimated cross-correlation function from the three methods are shown in Fig. 5.9. The peak value is higher by the GCC method than either by the SCOT or by the ML method. However as the SNR decreases to less than -12 dB, the peak values from the SCOT method approaches the same level as by the GCC method and the peak values from the ML method remains lower than those by the GCC and SCOT methods. Also when the SNR is greater than -12 dB, the standard deviation of the estimated cross-correlation function in GCC is significantly greater than those of the SCOT and the ML methods (Fig. 5.10).

The deviation of the peak locations vs. SNR results (Fig. 5.11) show that when the SNR is greater than -0.9 dB, all three methods can be used to accurately estimate the peak locations. When the SNRs are between the range of -1.0 dB to -15.0 dB, both the SCOT and ML methods can be used to locate the peak with less deviation than the GCC method. As the SNR decreases below -13.0 dB, the performances of both the SCOT and ML methods approaches that of the GCC in locating the peak.

The cross-correlation functions vs. SNRs of the three algorithms of one of the trials are shown from Fig. 5.12 to Fig. 5.14. Both the

SCOT and ML methods show a sharp and narrow peak at the delay times k_m and k_s , while the GCC method shows a sinewave shape of cross-correlation function with broader peaks at the delay times. As in the GWN case (section 5.2) with SNR greater than 0dB, the cross-correlation from the ML method shows two additional peaks of smaller amplitude at $2k_m+k_s$ ($2*15+20=50$) and $2k_s+k_m$ ($2*20+15=55$) on the +lag (motor) and -lag (sensory) sides respectively of the cross-correlation functions.

Similar results are obtained when the ML method is stimulated with the impulse input data sequence as will be discussed in Section 5.5.

The results of this SINE simulation suggest that when the input data is periodic, the SCOT and ML method are better than the GCC method in reducing the ambiguity of estimating the peak location of the cross-correlation function. As compared with the SCOT and ML methods, the standard deviation of the ML method decreases while that of the SCOT method increases with a decrease in SNR (Fig 5.10). However, because of the SNR weighting function of the ML method (Eq. 3.50, and Eq. 4.28 and see Section 5.6), as the SNR decreases, the amplitude of the cross-correlation in the ML method also decreases (Fig. 5.14, and 5.9). Below -15 dB SNR (Fig. 5.11), the SCOT and ML methods no longer have an advantage over the GCC method in locating the cross-correlation peaks.

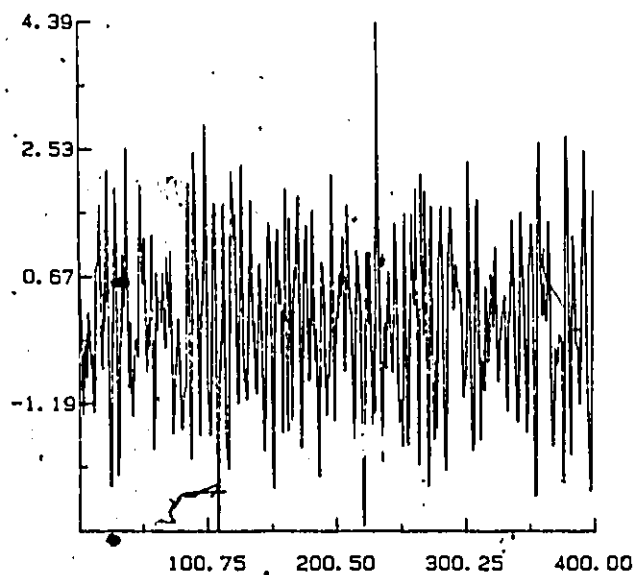


Fig 5.7 Waveshape of the sinewave data sequences of 1.5K Hz corrupted with GWN data sequence with a SNR of 0 db.

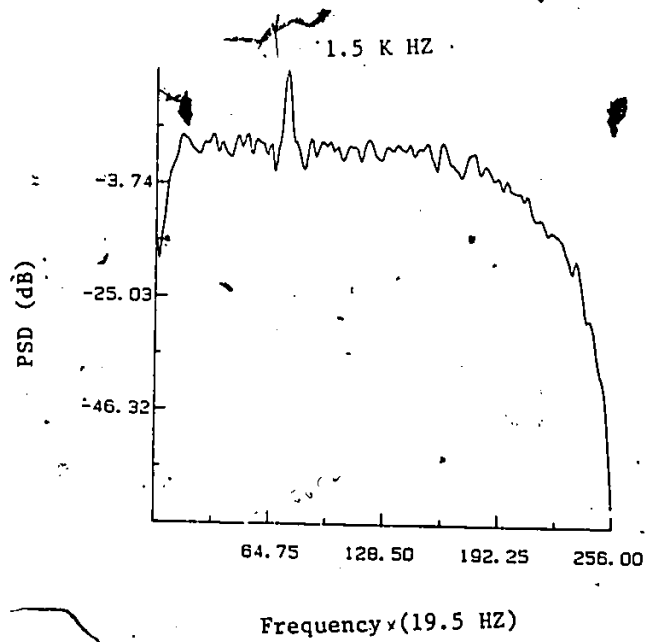


Fig 5.8 The power spectrum density (PSD) of the waveform shown in Fig 5.7. The peak in the PSD at 1.5K Hz corresponds to the sinewave frequency.

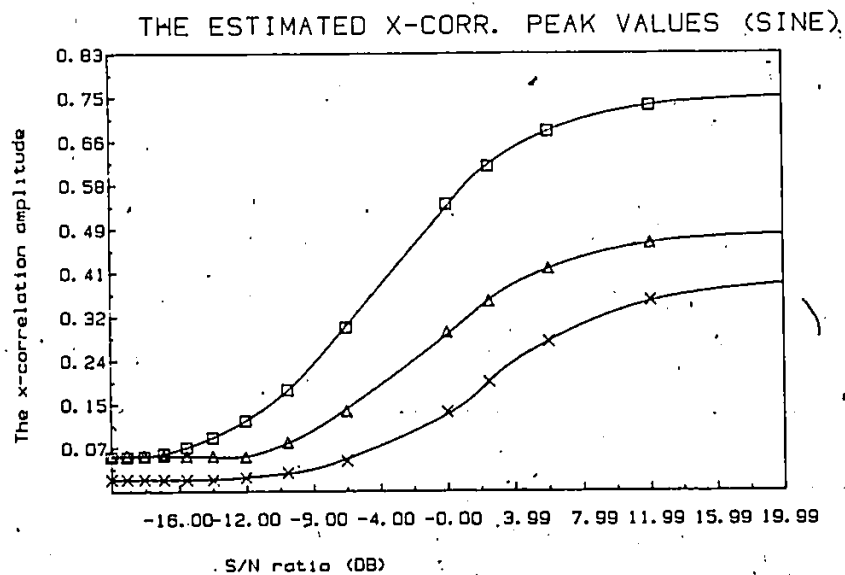


Fig 5.9 The average estimated cross-correlation peak values using the three algorithms: GCC (□), SCOT (△), and ML (×) with SINE wave as inputs. The peak cross-correlation function in GCC is higher than the peaks from the SCOT and ML methods. However as the SNR falls below -12.0 dB, the peak values from the GCC method approach those of the SCOT method. The peak values from the ML method are lower than those from the GCC and SCOT methods

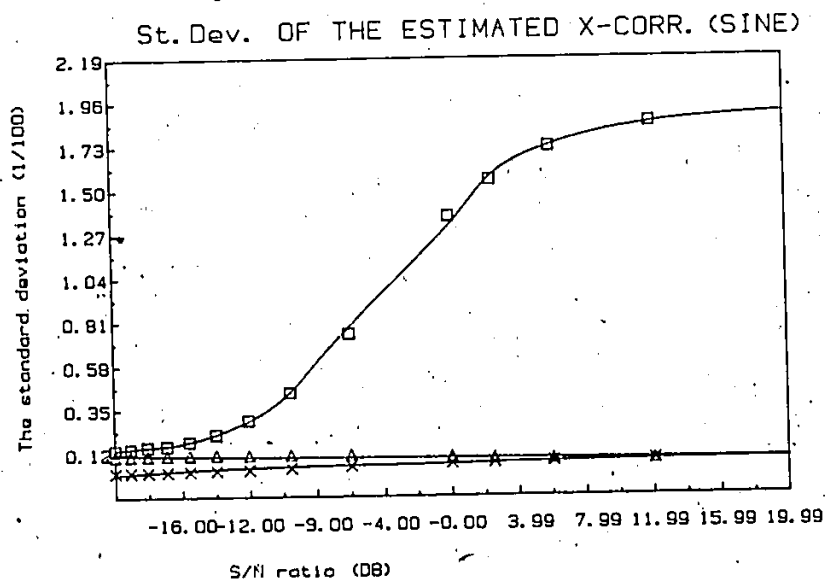


Fig 5.10 The standard deviation of the estimated cross-correlation function using the three estimation algorithms: GCC (\square), SCOT (\triangle), and ML (\times) with SINE wave as the inputs. When the SNR is greater than -12.0 db, the standard deviation of the estimated cross-correlation functions in the GCC method is significantly greater than that from the SCOT and the ML methods. When the SNR is less than -12.0 db, the standard deviation of the estimation in the GCC approaches that of the SCOT. The standard deviation obtained from the ML method decreases somewhat with the decrease in SNR, whereas the standard deviation increases in the SCOT method.

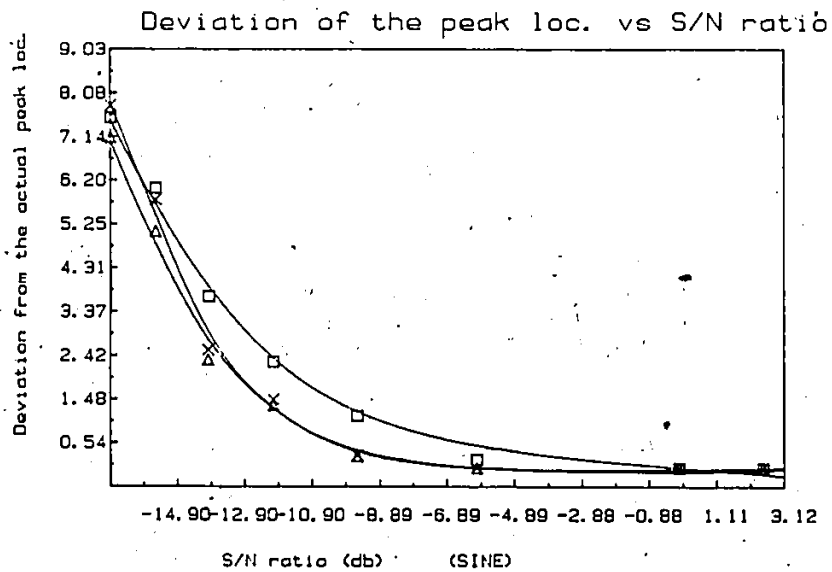


Fig 5.11 The average deviation of the estimated peak locations from the actual peak location. \square - GCC, Δ - SCOT, \times - ML. When the SNR is greater than -1.00 db, all three algorithms can be used to accurately locate the peak. However, between the range of -1.0 db to -15.0 db, both the SCOT and ML methods can be used to locate the peaks better than the GCC method. When the SNR is less than -13.0 db, the deviation of both the SCOT and ML methods approach that of the GCC method in locating the peaks.

Fig 5.12a,b The estimated cross-correlation as a function of number of lags and SNRs obtained from the GCC method with SINEwave as the input data. Fig 5.12b is the reverse view of Fig 5.12a. The SNRs scale for Fig 5.12a,b are the same as shown in Fig. 5.4a,b. The peaks locations for the sensory and motor sequences are at 20 and 15 respectively.

Simulation with sine+noise (GCC)

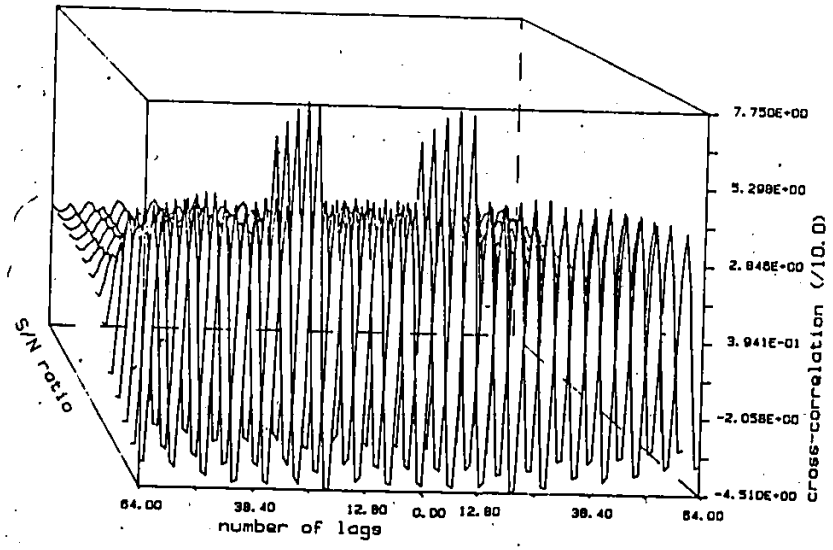


Fig. 5.12a

Simulation with sine+noise (GCC)

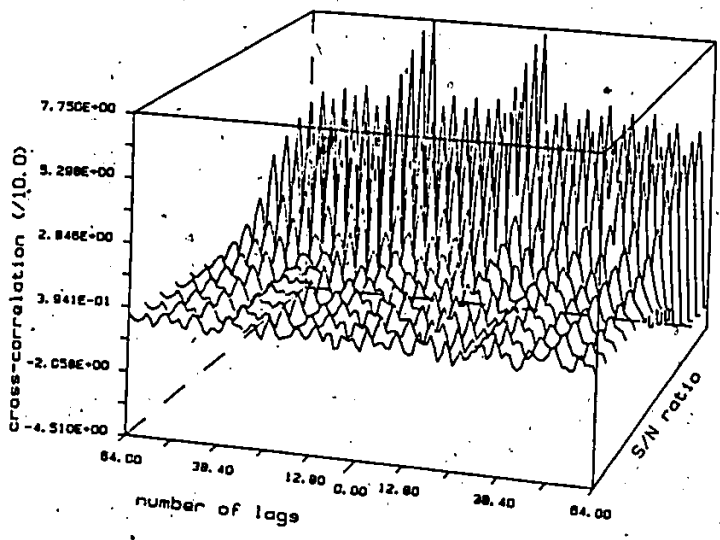


Fig 5.12b

Fig 5.13a,b The estimated cross-correlation as a function of number of tags and SNRs obtained from the SCOT method with SINE as the input data. Fig 5.13b is the reverse view of Fig 5.13a. The SNRs scales are the same as those of Fig 5.4a,b.

Simulation with sine+noise (SCOT)

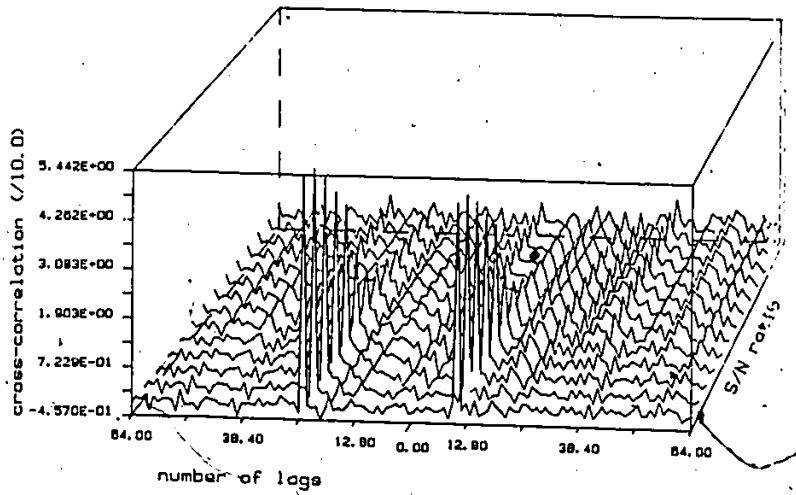


Fig 5.13a

Simulation with sine+noise (SCOT)

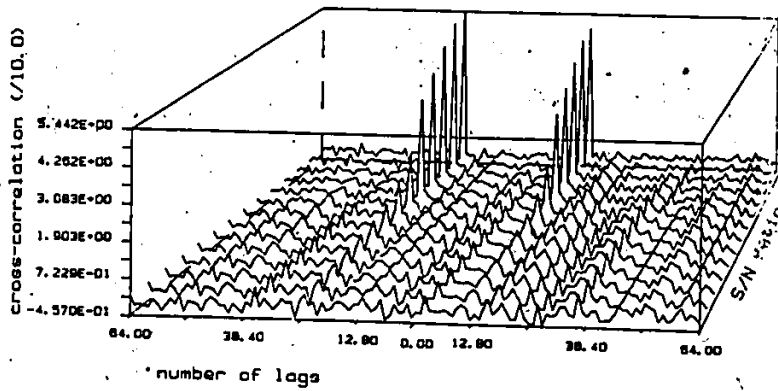


Fig 5.13b





Fig 5.14a,b The estimated cross-correlation as a function of number of lags and SNRs. obtained from the ML method with SINE as the input data. Fig 5.14b is the reverse view of Fig 5.14a. The SNRs scales are the same as those of Fig 5.4a,b.



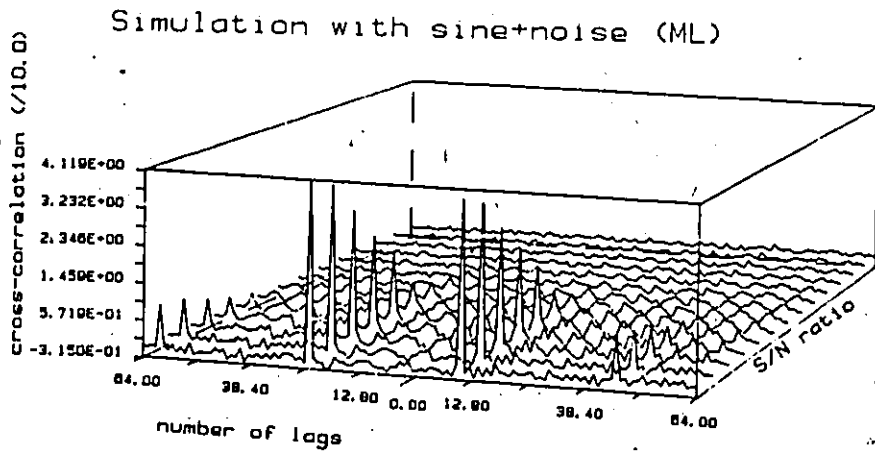


Fig. 5.14a

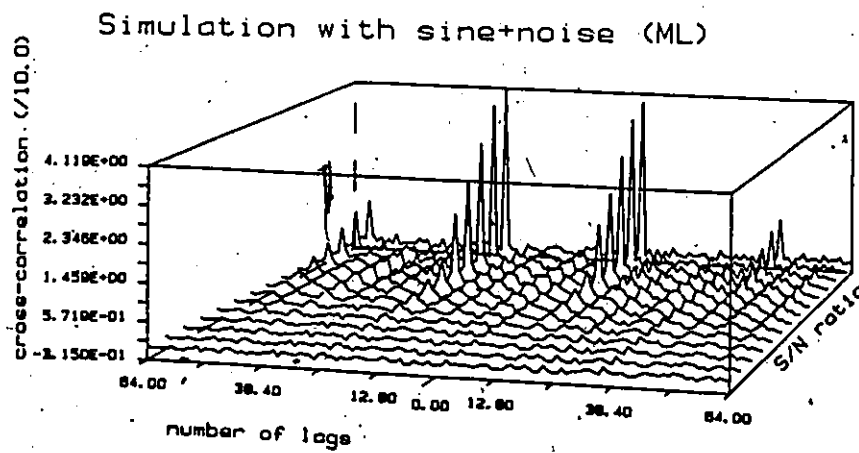


Fig. 5.14b

5.5 SIMULATION WITH IMPULSE

Two sequences of simulated impulse data (Section 5.1) are used as the sensory and motor input of the simulation model (Fig. 3.5b). The waveshape and the PSD of one of the channels after corrupting with the GWN are shown in Fig. 5.15 and Fig. 5.16 respectively. The periodic nature of the impulses can be easily discovered from the power spectrum as regularly placed peaks. Although the waveshapes of all impulses are identical, the period between each impulse has been made random (section 5.1); hence the distortion in estimating the power spectrum in GCC is not as high as that of simulated pure periodic signals.

The results of the estimated cross-correlation peak values (Fig. 5.17) show that the peaks from the GCC method are higher than those from the SCOT and ML methods. The differences, however, are not as great as those in the sinewave case (Fig. 5.11). The differences in the peak values between the SCOT and the ML methods are approximately the same as that of simulation with the sinewave.

The standard deviation of the estimated cross-correlation function (Fig. 5.18) in GCC remains significantly higher than the SCOT and ML until the SNR decreases to below -8 dB where the standard deviation from the GCC method approaches that of the SCOT method. Between the range of 12 dB to -16 dB, the standard deviation of the estimated cross-correlation functions in the ML method decreases while that in the SCOT method increases as the SNR decreases (Fig. 5.18).

The results from the deviation of the estimated peak locations (Fig. 5.19) show that when the SNR is between the range of -5.0 to -13.0

dB, the performance of the SCOT or the ML method is slightly better than that of the GCC. As the SNR decreases to less than -13 dB, the performances of the SCOT and ML approach that of the GCC method.

The estimated cross-correlation function vs. SNRs of the three algorithms of one of the trials are shown in Figs. 5.20 to 5.22. The peaks in the GCC method are wider and as the SNR decreases, it is more ambiguous to determine the cross-correlation peaks. The SCOT and the ML methods provide sharper and narrower peaks at the locations k_m and k_s on the +lag and -lag sides respectively. Similar to the other two simulations i.e., GWN and SINE cases, the cross-correlation in the ML method shows two small peaks at the $2k_m+k_s$ ($= 55$) and $2k_s+k_m$ ($= 50$) on the respective +lag and -lag sides.

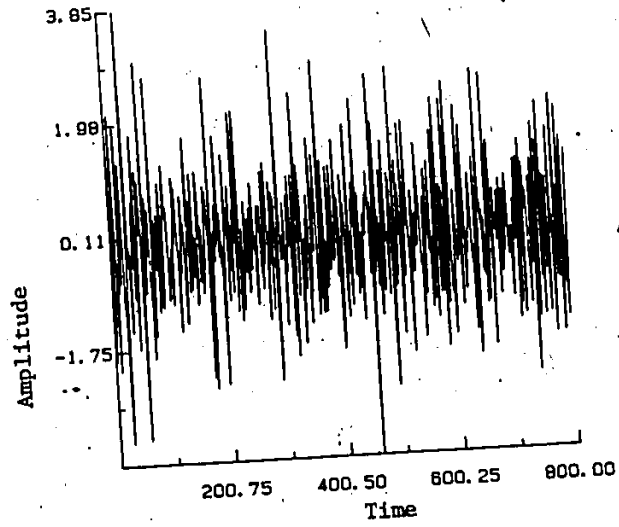


Fig 5.15 Waveshape of the impulse data sequences corrupted with GWN data sequence with a SNR of 0 dB.

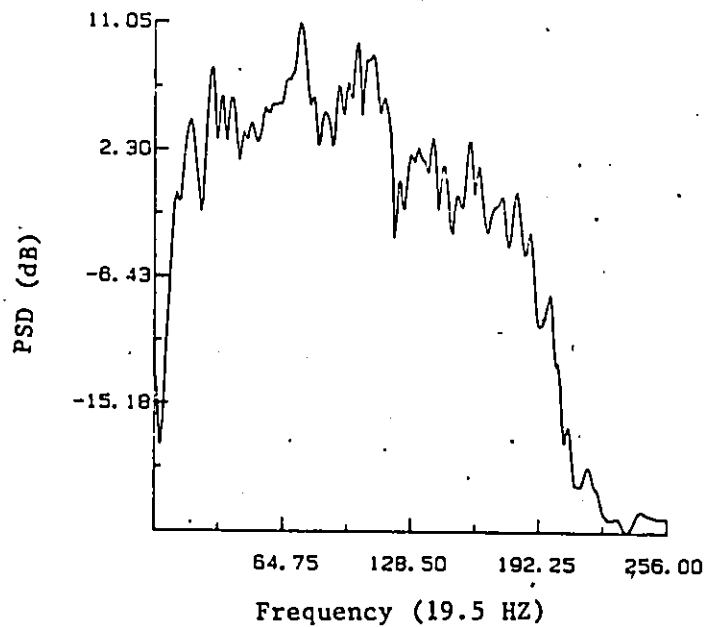


Fig 5.16 The power spectrum density (PSD) of the impulse data sequences corrupted with GWN data sequence shown in Fig .15.

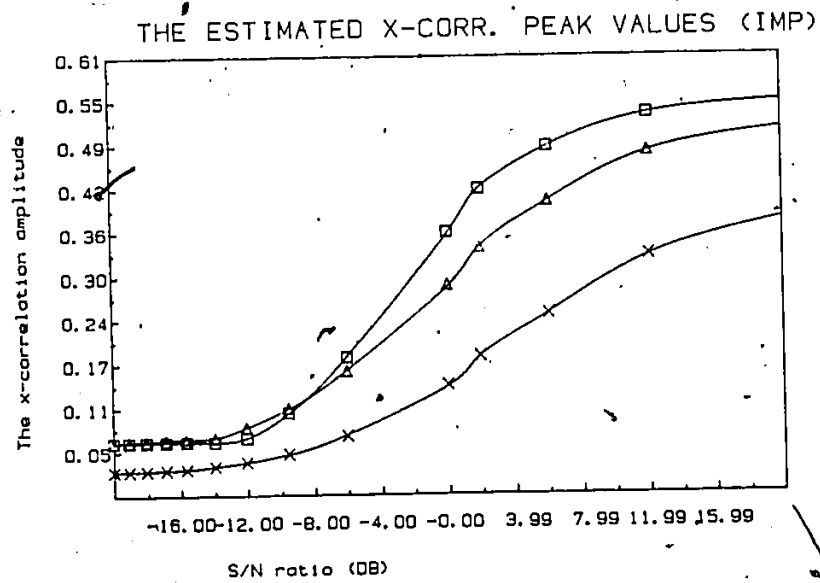


Fig 5.17

The average estimated cross-correlation peak values using the three algorithms: GCC (□), SCOT (△), and ML (X) with IMPulse as inputs. The peak cross-correlation function in GCC is higher than the peaks from the SCOT and ML methods. However, as the SNR falls below -12.0 dB, the peak values from the GCC method approaches that of the SCOT method. The peak values from the ML method are lower than that from the GCC and SCOT methods

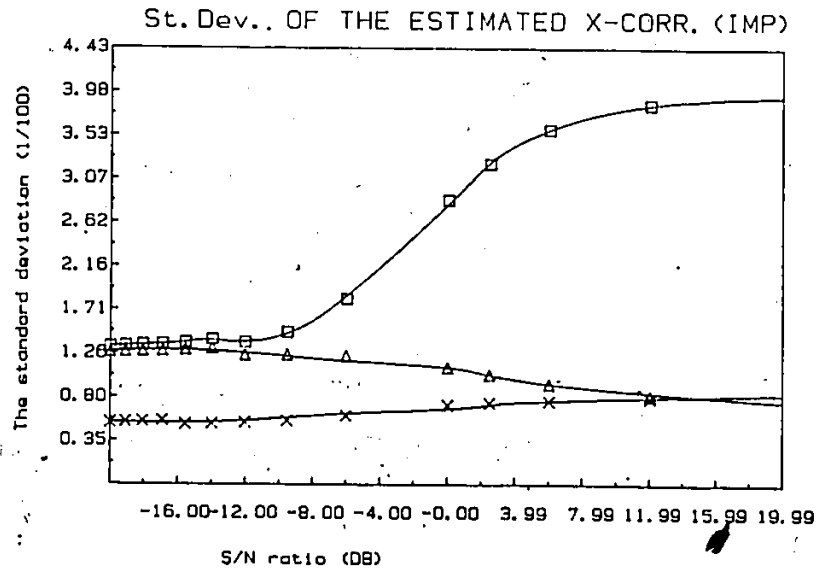


Fig 5.18 The standard deviation of the estimated cross-correlation function using the three estimation algorithms: GCC (□), SCOT (Δ), and ML (X) with IMPulse as the inputs. The standard deviation of the estimated cross-correlation functions in GCC is significantly higher than the SCOT and ML until the SNR falls below approximately -8 db where the standard deviation from the GCC method approach that of the SCOT method. Between the range of 12 db to -16 db, the standard deviation of the estimated cross-correlation functions in the ML method decreases while that in the SCOT method increases as the SNR decreases.

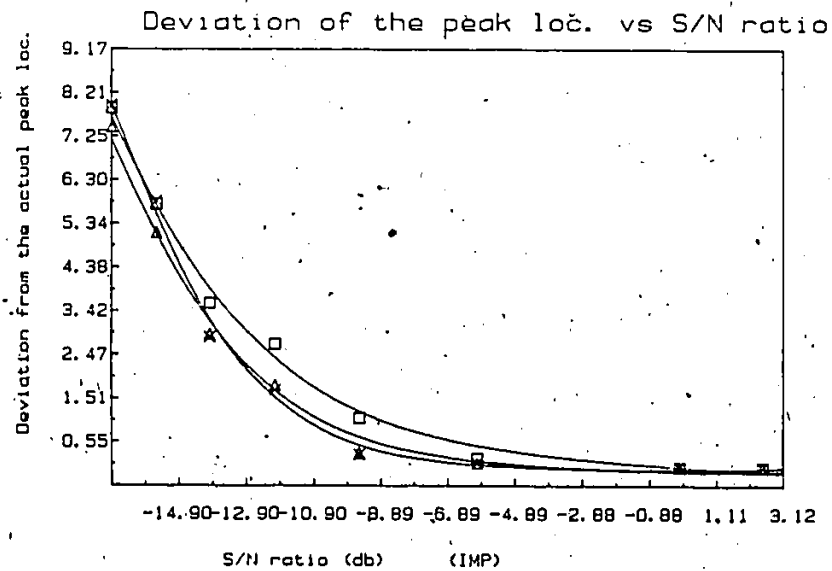


Fig 5.19 The average deviation of the estimated peak locations from the actual peak location. \square - GCC, Δ - SCOT, \times - ML with IMPulse as the inputs. when the SNR is between the range of -5.0 to -13.0 db, the performances of the SCOT and ML methods are slightly better than that of the GCC method. As the SNR falls below -13 db the performance of the SCOT and ML approaches that of the GCC method.

Fig 5.20a,b The estimated cross-correlation as a function of number of lags and SNRs obtained from the GCC method with IMPulse as the input data. Fig 5.20b is the reverse view of Fig 5.20a. The SNRs scale for Fig 5.20a,b are the same as shown in Fig. 5.4a,b. The peak locations for the sensory and motor sequences are at 20 and 15 respectively.

Simulation with impulses+noise (GCC)

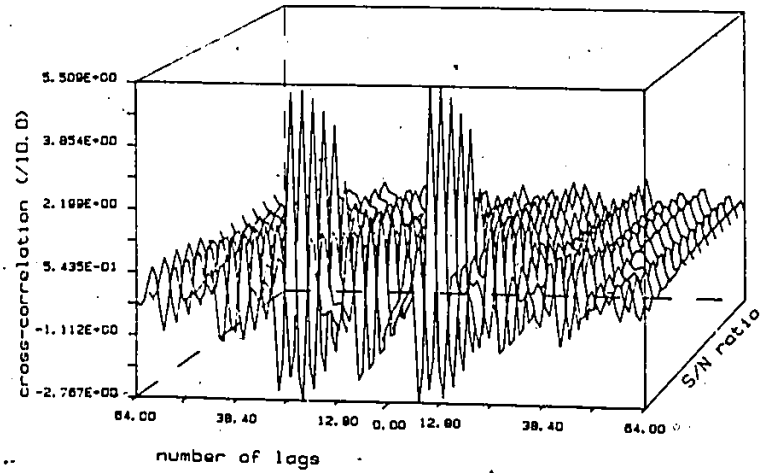


Fig 5.20a

Simulation with impulses+noise (GCC)

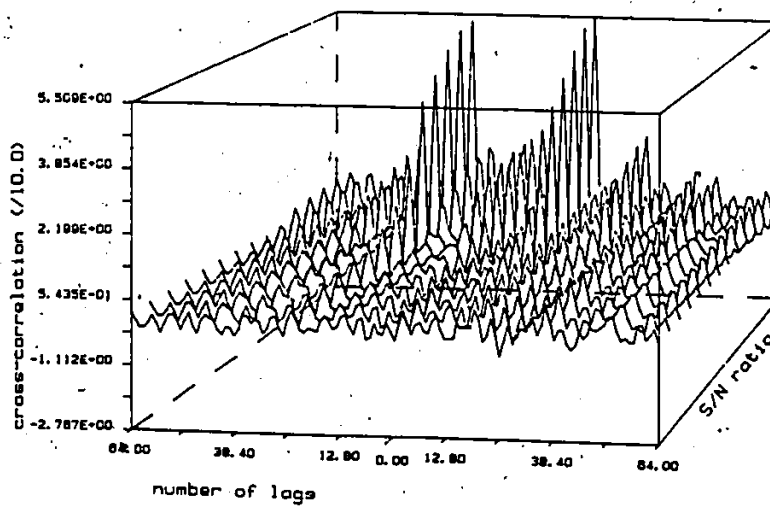


Fig. 5.20b

Fig 5.21a,b The estimated cross-correlation as a function of number of lags and SNRs obtained from the SCOT method with IMPulse as the input data. Fig 5.21b is the reverse view of Fig 5.21a. The SNRs scales are the same as those of Fig 5.4a,b.

Simulation with impulses+noise (SCOT)

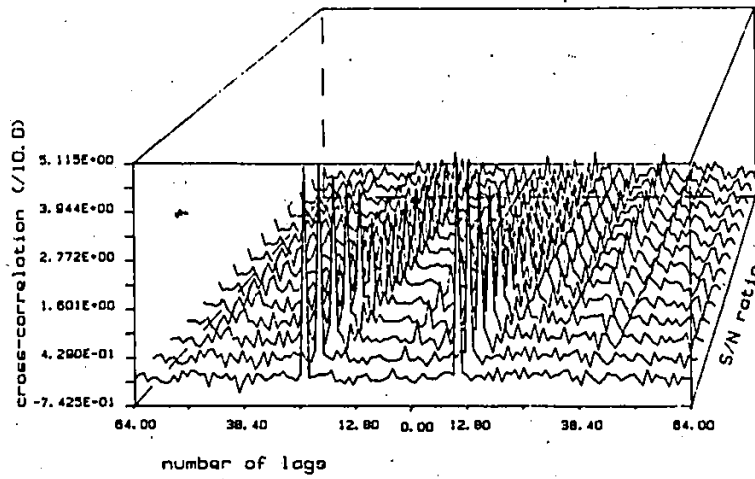


Fig. 5.21a

Simulation with impulses+noise (SCOT)

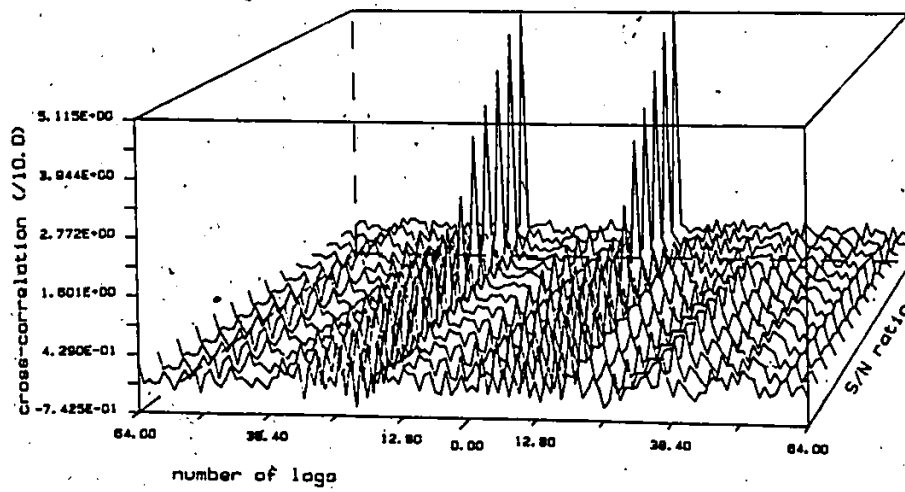


Fig. 5.21b

Fig 5.22a,b The estimated cross-correlation as a function of number of lags and SNRs obtained from the ML method with 100 pulses the input data. Fig 5.22b is the reverse view of Fig 5.22a. The SNRs scales are the same as those of Fig 5.4a,b.

Simulation with impulses+noise (ML)

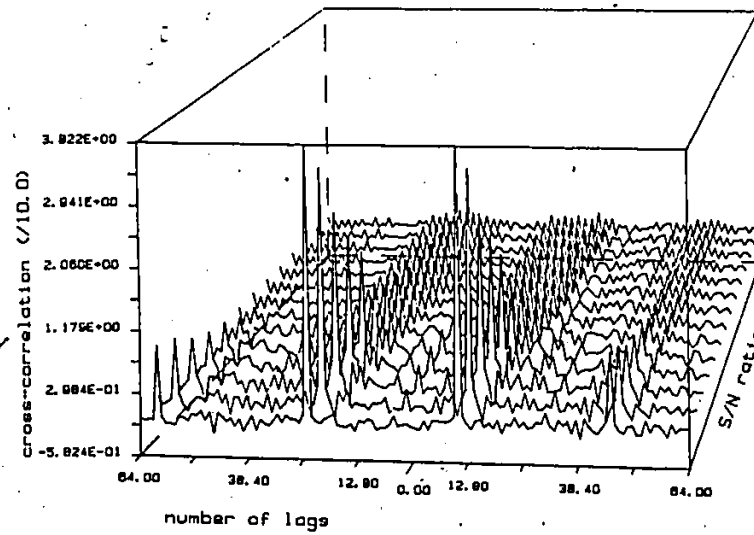


Fig. 5.22a

Simulation with impulses+noise (ML)

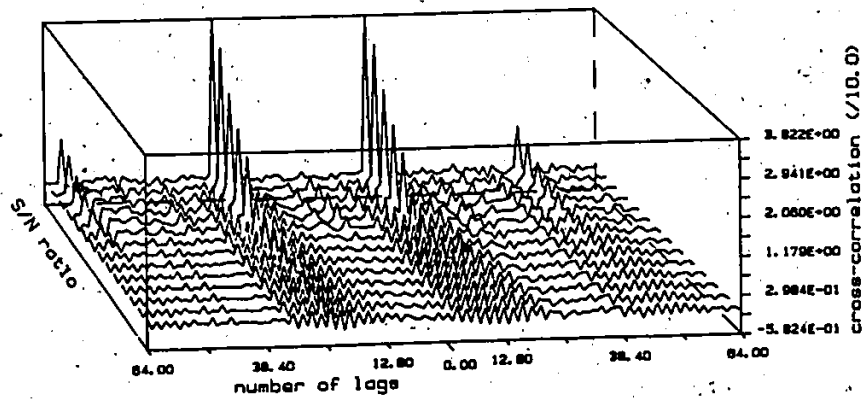


Fig. 5.22b

5.6 Summary:

For the case of GWN inputs, the GCC methods can estimate the delay time location as well as the SCOT and ML methods with the exception that the cross-correlation peaks are broader than by the SCOT and ML methods. For the case of periodic signals (SINE, and IMP) inputs, the SCOT and ML methods exhibit higher accuracy in estimating the delay time location than the GCC method. When the SNR is high, the ML method is superior to the SCOT method, because of lower standard deviation in the cross-correlation function. When the SNR is low, the ML method has no advantage over SCOT method because the performance of the ML method approaches that of the SCOT weighted with SNR (see section 7.6). For all cases of inputs, when the SNR is greater than 0 dB and analyzed with the ML method, there are two extra peaks located at $2k_m + k_s$ and $2k_s + k_m$ on the +lag and -lag sides respectively.

The application of these three algorithms in analyzing the compound neural signals that consist of both sensory and motor components is discussed in the next Chapter. The discussion of the simulated results is given in Chapter VII.

CHAPTER VI

RESULTS: NEURAL SIGNALS

6.1 INTRODUCTION

The performances of the three cross-correlation algorithms (GCC, SCOT, and ML) have been described (Chapter V). In this chapter examples of neural signal waveforms together with their corresponding EMGs and the contractile activities are given. Using the three algorithms, the sensory and motor neural patterns are analyzed under the conditions of: during periods of contractions; during quiescence (no contractile activities); in the case of highly damaged nerve trunk; and, neural signals contaminated with artifacts. As mentioned in Chapter II and III, the cuff electrode can be used to record neural signals as well as to stimulate the enclosed nerve trunk. In this chapter, the results of stimulating the nerve of Latarjet with one of the cuff electrodes and observing the contractile activities, as well as stimulating the cervical vagal nerve at the neck and recording the synchronized firing impulses with the cuff electrode are also given. The sensory and motor neural patterns with respect to the duration of the nerve cuff implantation are also discussed to study the durability of the cuff electrode and possible damage to the nerve trunk. The condition of the

nerve trunk enclosed in the cuff as compared to that without a cuff electrode studied by means of electron microscopy is discussed. Finally, the condition of the nerve cuff and the enclosed nerve trunk are also illustrated by measuring the nerve cuff impedance during the implantation period.

6.2 TYPICAL RECORDED NEURAL SIGNALS WITH CORRESPONDING EMG AND CONTRACTILE PATTERNS

As mentioned in Chapter II (Section 2.3.2), the major functions of the stomach and the duodenum are storage, mixing and propulsion of the ingested materials. Depending on the nature of gastric contents, the hormonal, neurogenic (both intrinsic and extrinsic) and myogenic controls generate a variety of coordinated motility patterns in the stomach and the duodenum. Since the extrinsic neural control is one of the important factors in influencing gastric motility (Section 2.3.2), most changes in the motility patterns should also reflect extrinsic neural activities. Three examples of the recorded neural signals together with their corresponding EMG and contractile activities are given in the following sections. The locations of the implanted electrodes was given in Fig. 4.5.

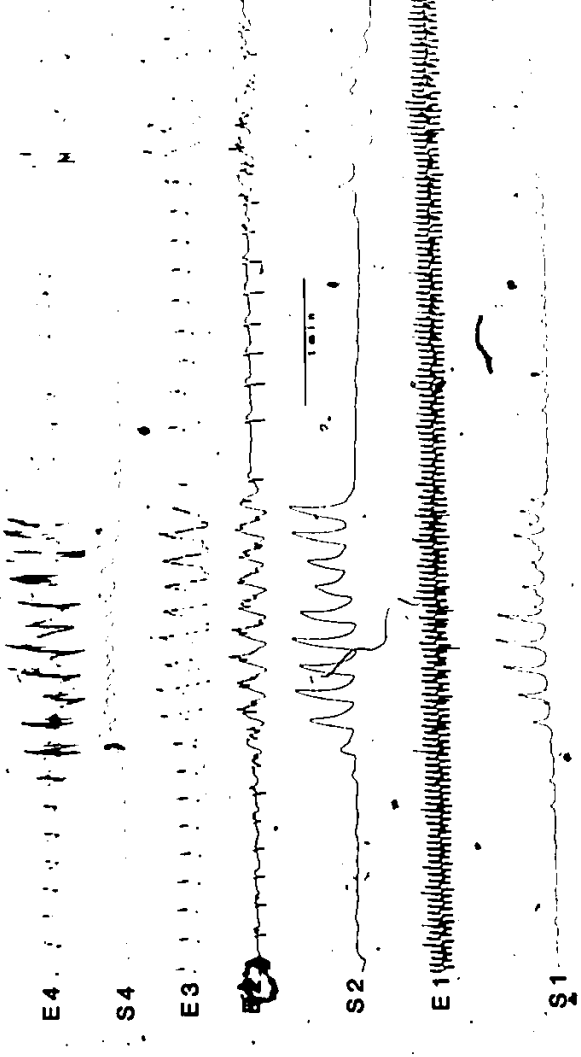
6.2.1 SYNCHRONIZATION OF THE NEURAL ACTIVITIES WITH EMG AND CONTRACTILE ACTIVITIES

An example of synchronization of neural activities with the

corresponding EMG and contractile activities of the corpus (E4,S4), the antrum (E3,E2,S2), and the proximal duodenum (E1,S1) are shown in Fig. 6.1. The dual neural signals recorded from cuff N1 are shown in N11, N12, whilst those in cuff N2 are shown in N21, N22 respectively.

The omnipresent ECA oscillations interact with nerve mediators or hormones to cause prolonged depolarization or spikes i.e., ERA leading to contractions. The maximal rate of contraction is 5 /minute in the stomach and 18 /minute in the duodenum in a dog. The neural signals from the two cuffs (N11 and N12; N21 and N22) are characterized by bursts at about 5 per minute and the occurrence of the bursts are also synchronized with the EMG of the corpus (E4) and the antral (E3, E2) areas. The example given in Fig. 6.1 also shows such bursts synchronized with the duodenal contractions at the antral rate. The sensory and motor patterns of the two sections of the compound neural signals (Box A and B in Fig. 6.1) corresponding to the contractile and quiescence periods respectively are shown later in Section 6.3. Two other examples of the neural signals with their corresponding EMG and contractile activities are discussed in the following sections.

Fig 6.1 An example of synchronization of neural activities with the corresponding EMG and contractile activities of the corpus, (E4,S4), the antrum (E3,E2,S2) and the duodenum (E1,S1). Traces N11 and N12 are neural signals from the cuff N1 and traces N21, N22 are neural signals from the cuff N2. During contractions, ERA appears on ECA, the basic carrier signals (E4,E3,E2, and E1) at a frequency of 5 per minute. The neural signals are also characterized by bursts at about 5 per minute and are synchronized with the EMG and contractions of the corpus, antrum and the duodenum. The sensory and motor patterns of the two sections of the compound neural signals (Box A, and Box B) are shown in Fig 6.4 and 6.6 respectively. The location of the implanted electrodes are shown in Fig 4.5.



6.2.2 ALTERNATING FIRING PATTERNS BETWEEN ADJACENT NERVES

The alternating firing patterns consist of both long and short durations. For the long period type, the bursting patterns between nerve trunks alternate over a duration longer than one ECA period, whereas the bursting patterns for the short period type alternate within one ECA period.

An example of the long period alternating firing pattern between cuffs N1 and N2 with the EMG and contractile patterns of the corpus (E4,S4) and of the antral areas (E2,S2) are shown in Fig 6.2. The contractile activities during the initial 4 minutes of the record were relatively low, but there were some large burst of neural activities at cuff N1 and N2. It appears that the neural bursting patterns are recorded first at cuff N1 and after approximately 20 seconds a similar pattern occurs at N2.

An example of the short period type of alternating firing pattern is given in Fig 6.3 where the neural bursting activities of N1 and N2 can be seen to alternate within one ECA cycle. The contraction rate of the stomach as well as of the duodenum were at 5 per minute, the ECA rate of stomach.




Fig 6.2 An example of a long duration alternating firing patterns between N1 and N2 shown with the EMG and the contractile patterns of the corpus (E4,S4) and the antrum (E2,S2) areas. During the initial four minutes, the contractile activities of both corpus (S4) and antrum (S2) are relatively low with some large bursts of neural activities at cuff N1 (N11,N12) and N2 (N21,N22). It appears that the neural bursting patterns are recorded first at cuff N1 and after approximately 20 seconds, the similar pattern occurs at cuff N2.

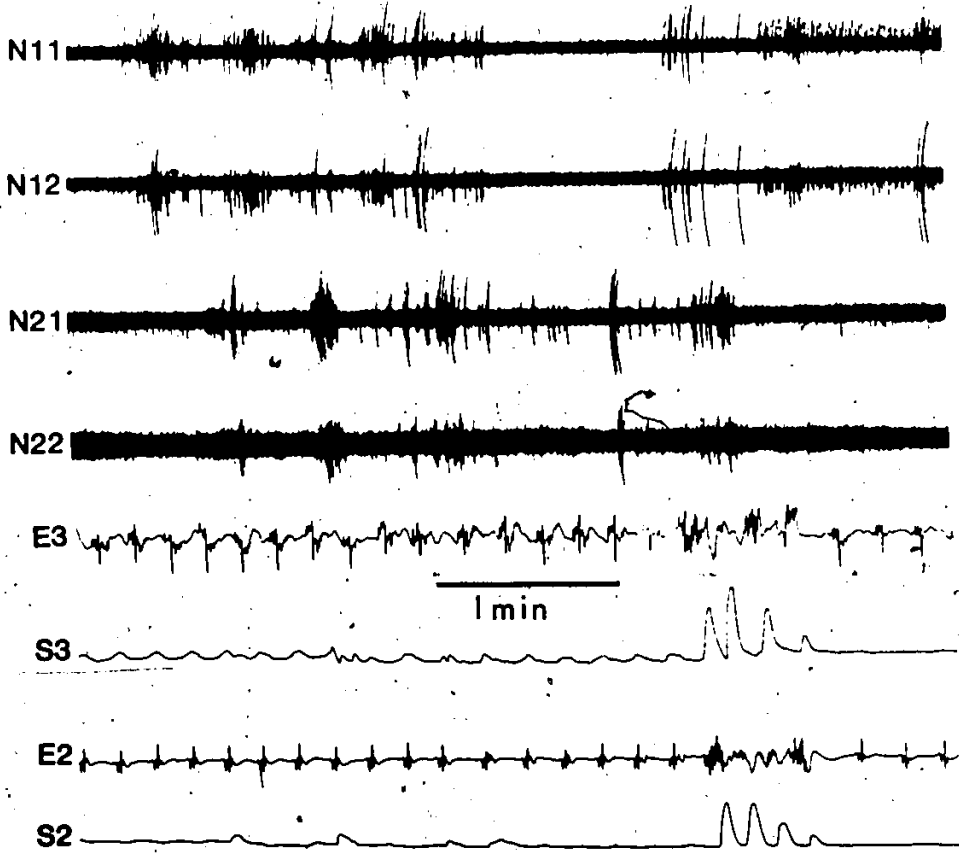
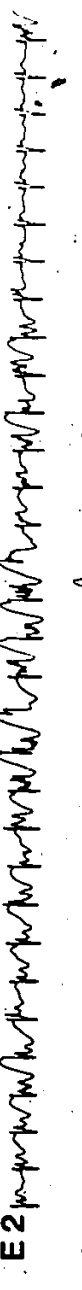
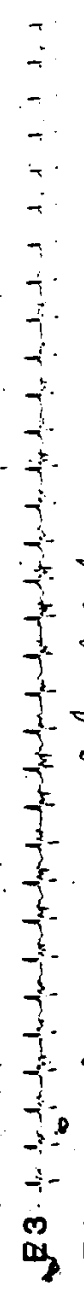


Fig 6.3 An example of the short duration type of alternating neural firing pattern. The neural bursting activities of N1 (N11, and N12) and N2 (N21, and N22) can be seen to alternate within one ECA cycle. The rates of contraction in the stomach as well as in the duodenum were at 5 per minute, the ECA rate of the stomach.



Handwritten signature or mark at the bottom of the page.

6.3 TYPICAL SENSORY AND MOTOR NEURAL PATTERNS

The sensory and motor neural patterns under four different conditions are discussed here: a) during active contractile activities; b) during quiescent period; c) of highly damaged nerve trunk; and d) neural signals contaminated with movement artifacts. It was shown in Chapter IV that the neural patterns are shown in three dimensions with the cross-correlation between two neural signals as a function of lags and times, with negative lags representing sensory components and positive lags representing motor components. Each trace of the 3-D figures represents the average cross-correlation obtained from 2.02 seconds of neural signals. Results using all the three algorithms are shown for each case in order to illustrate their corresponding performance.

6.3.1 PATTERNS DURING ACTIVE CONTRACTILE PERIODS

An example of the cross-correlation between two channels of recorded neural signals during the contractile period are shown in Figs. 6.4. The corresponding EMG and the contractile activities are shown in Box A in Fig 6.1. In general the amplitudes of the cross-correlations of the sensory components are greater than those of the motor components suggesting the dominance of sensory signals along the nerve trunk over the motor signals. This agrees with the fact that the ratio of the sensory and motor nerve fibres within the nerve of Latarjet is approximately nine to one [Agostini et al. 1951]. The average peak locations

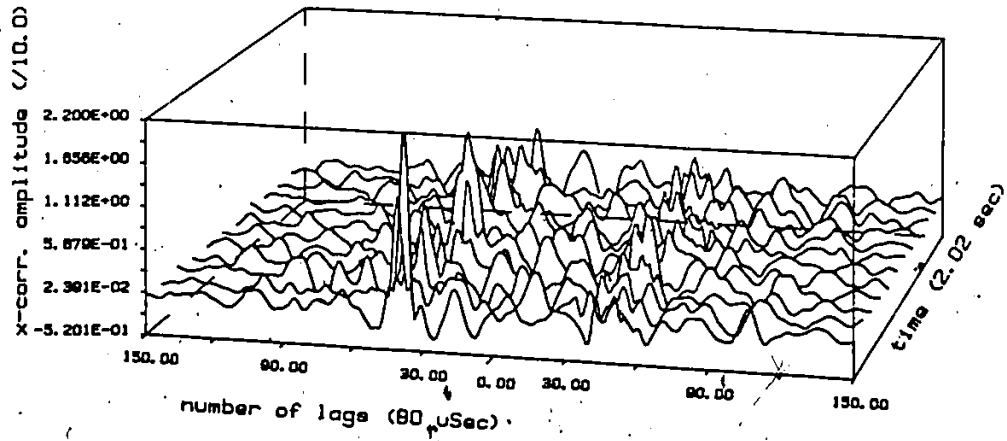
of both the sensory and motor components are between 45 ± 10 lags. Since the distance between the two electrode is 10 mm, and the time interval between each lag corresponds to 80 μ seconds, the average conduction velocity of the sensory components is approximately $10 \text{ mm} / (45 \times 80 \text{ } \mu\text{sec})$ or 2.8 meters/seconds. However, as shown later in Section 6.4, as the duration of the electrode implantation increases, (after about 60 days) the average conduction velocity of the sensory components decreases somewhat (i.e. the sensory cross-correlation peak location shifts further away), and the determination of cross-correlation peaks of the motor components becomes difficult.

When the cross-correlation diagram (Fig 6.4b) is viewed from the cross-correlation amplitude vs time axes, the peak values of the sensory and motor cross-correlations with respect to time are shown in Fig 6.5. It appears that before the contractile activities, there is a rise of motor activities, and during the peak and at the end of the contraction, the sensory activities increase with decreasing motor activities. The peaks of the motor activities lead the sensory peaks by approximately 3.5 seconds.

As shown in simulation studies (Chapter V) the cross-correlation obtained from the GCC method (Fig 6.4a) provides the highest amplitudes, but is more ambiguous in determining the peak locations. It is less ambiguous in recognizing the cross-correlation peaks in the SCOT and ML methods shown in Fig 6.4b and Fig 6.4c respectively. However, because of low SNR, the peaks in the ML method are highly attenuated (Section 5.6).

Fig 6.4 Cross-correlation between two channels (N21,N22) of the recorded neural signals during the contractile period. The cross-correlations using GCC, SCOT and ML methods are shown in Fig 6.4a, 6.4b, and 6.4c respectively. To the left of the zero lags of the cross-correlation functions are the sensory components, whereas to the right of the zero lags are the motor components. Each trace represents the averaged cross-correlation of 2.02 seconds of neural signals. The cross-correlations from all the three methods (GCC, SCOT, ML) show that the sensory cross-correlation components are greater than those of the motor cross-correlation. However, it is more ambiguous in determining the peak locations from the GCC method (Fig 6.4a). The peaks in the SCOT and ML methods are sharper and narrower, hence less ambiguous in determining the peak locations.

DOG #2987 (T16 346-391) (GCC)



DOG #2987 (T16 292-346) (GCC)

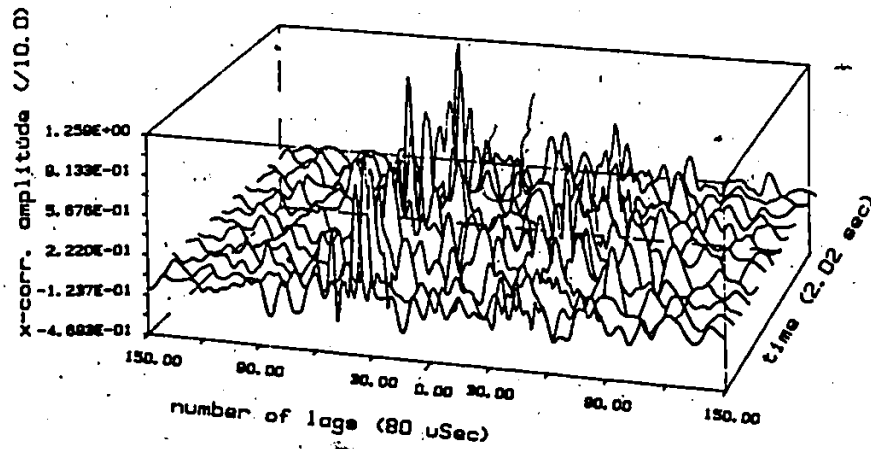
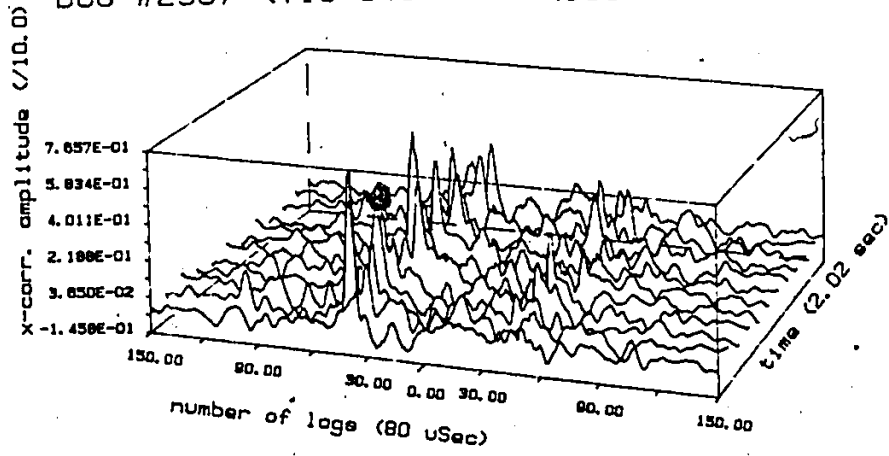


Fig 6.4a



DOG #2987 (T16 346-391) (SCOT)



DOG #2987 (T16 292-346) (SCOT)

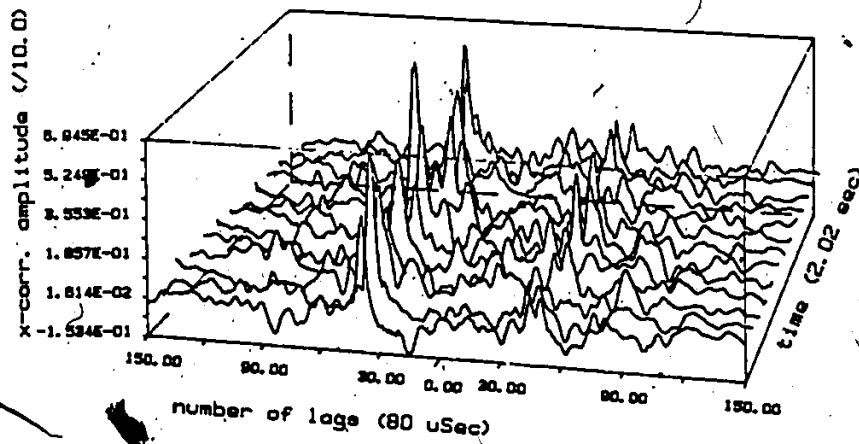
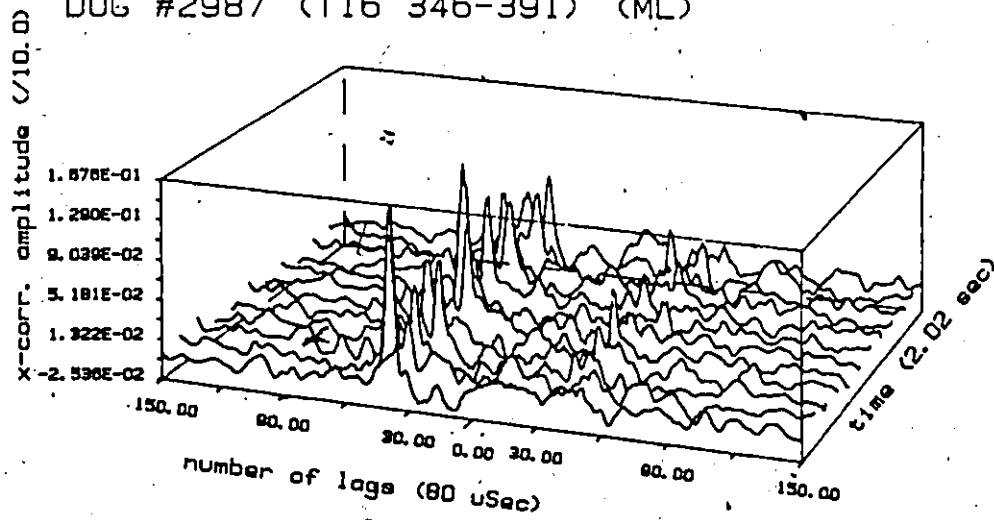


Fig. 6.4b

DOG #2987 (T16 346-391) (ML)



DOG #2987 (T16 292-346) (ML)

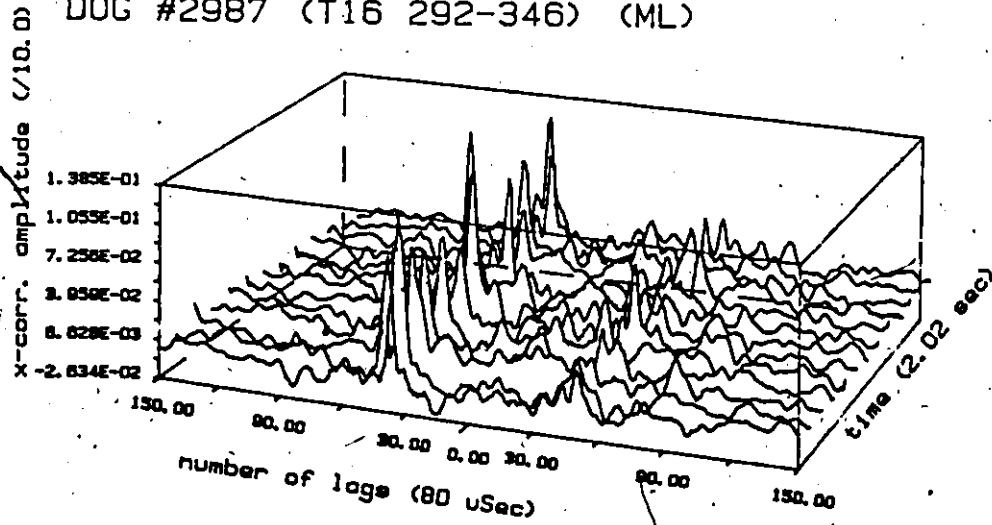


Fig. 6.4c

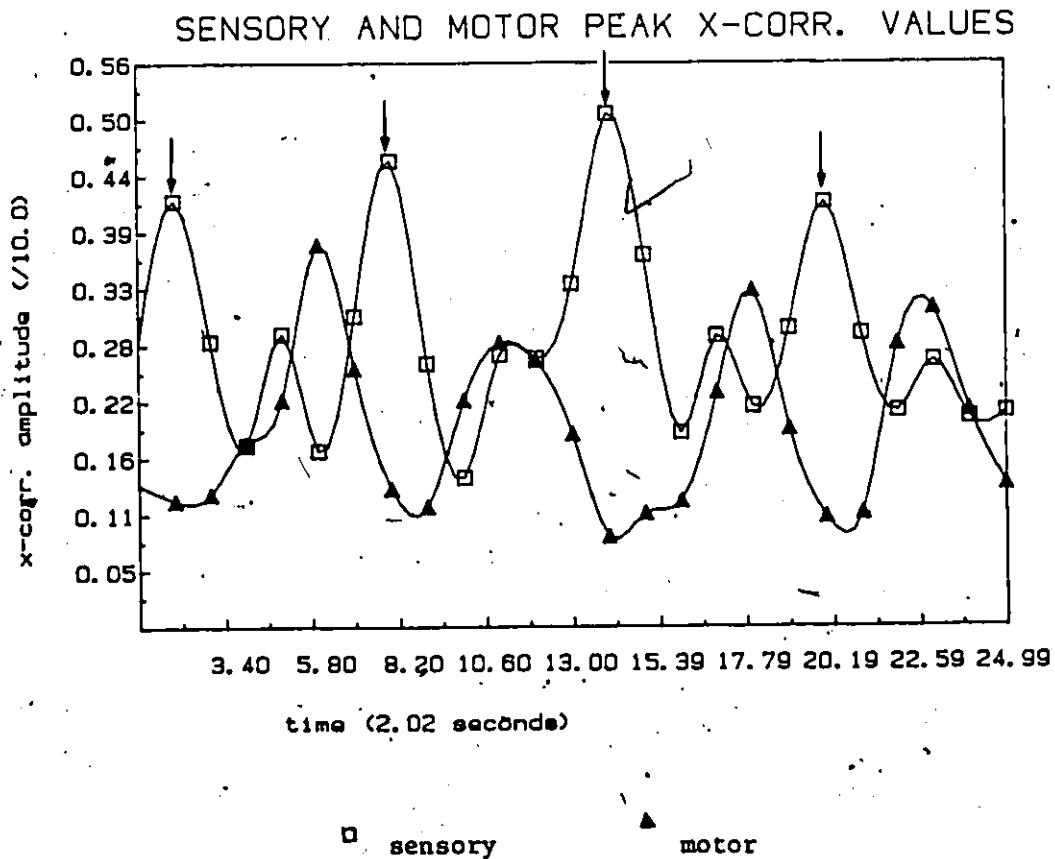


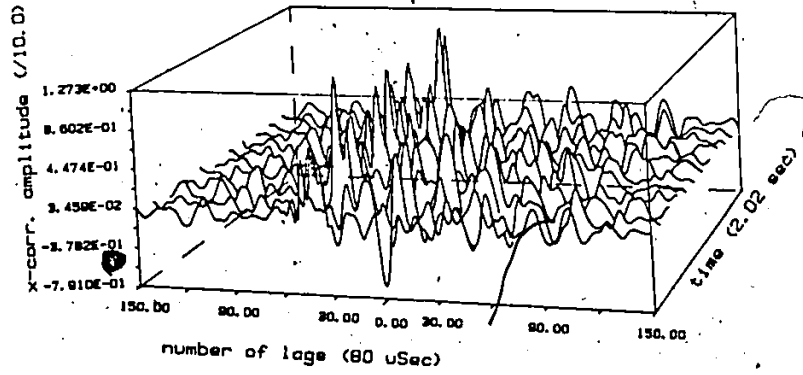
Fig 6.5 The peak values of the sensory and the motor cross-correlation by the SCOT technique with respect to time from Fig 6.4b. Downward arrows ↓ indicate peak of contractions. Note that before the peak of contraction, there is a rise of motor activities, and during the peak and end of contraction, the sensory activities increase with decreasing motor activities. The peaks of the motor activities are approximately 3.5 seconds ahead of the sensory peaks.

6.3.2 PATTERNS DURING QUIESCENT PERIODS

Examples of the three cross-correlation techniques between the two channels of neural signals when there is no measurable contractile activities are shown in Fig 6.6a-c. The corresponding EMG and contractile signals are shown in box B in Fig 6.1. As shown in Fig 6.6a, the GCC method is ambiguous in determining the cross-correlation peaks. However, the cross-correlations using the SCOT and ML methods show that there are peaks corresponding to the sensory activities, but there do not appear to be peaks corresponding to the motor activities. This suggests that during quiescence, the motor activities may not exist or may be too low to be detected by the various algorithms. Meanwhile there are sensory activities probably generated by the mechanoreceptor and/or chemoreceptors of gastric muscle in mucosa providing information on the conditions of the gastric system to the CNS.

Fig 6.6 Cross-correlation between N21 and N22. When there are no measurable contractile activities. The corresponding neural signals, EMG, and contractile activities are shown in Fig 6.1 (Box B). The GCC method is ambiguous in determining the cross-correlation peaks (Fig 6.6a). The cross-correlations using the SCOT and ML methods (Fig 6.6b, Fig 6.6c), however, show that there are peaks corresponding to the sensory activities, but there do not appear to be peaks corresponding to the motor activities.

DOG #2987 (T16 543-586) (GCC)



DOG #2987 (T16 500-543) (GCC)

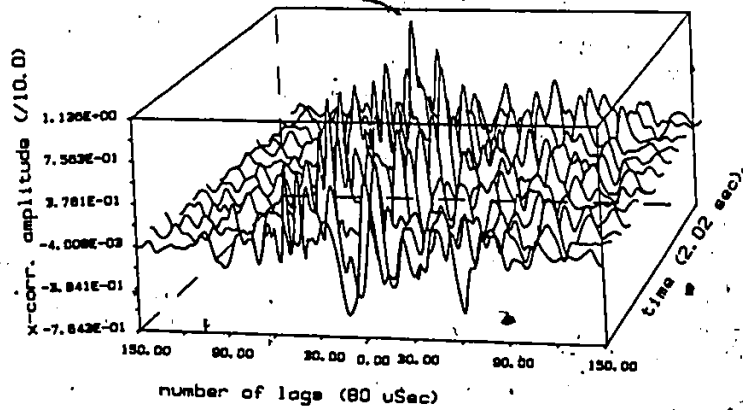
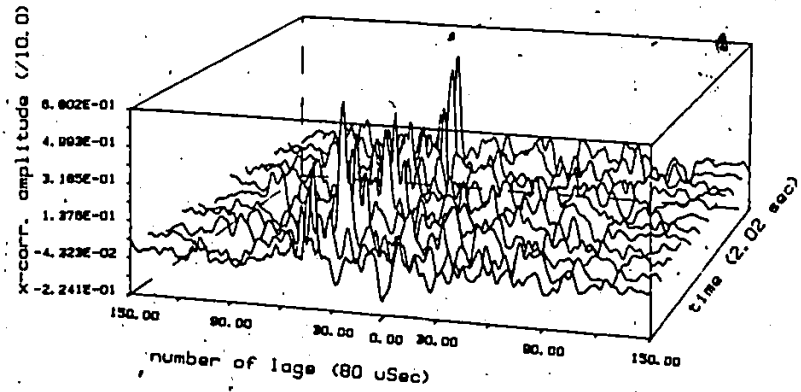


Fig. 6.6a



DOG #2987 (T16 543-586) (SCOT)



DOG #2987 (T16 500-543) (SCOT)

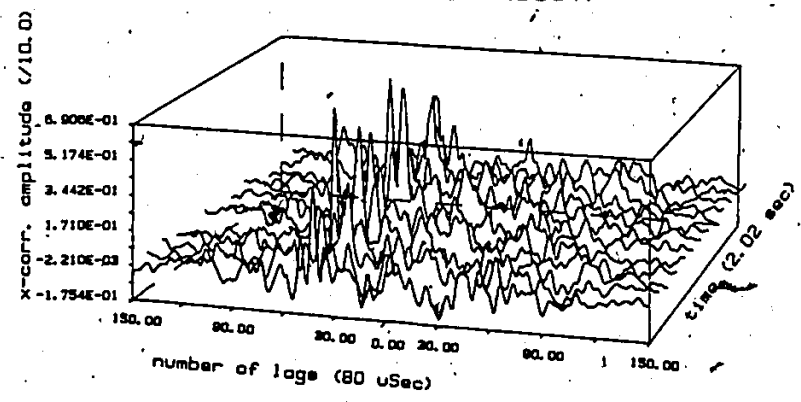
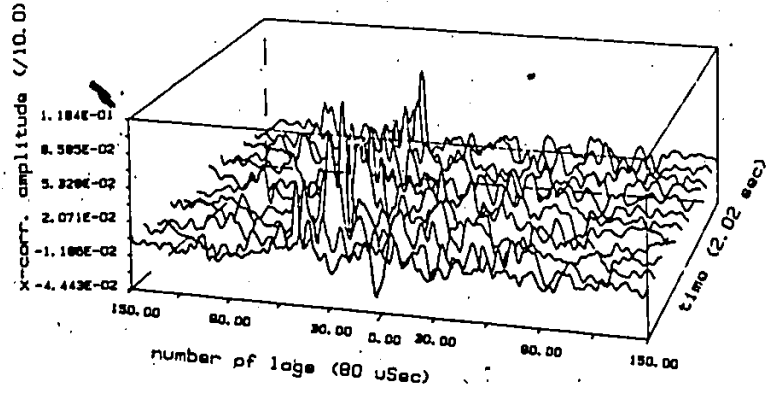


Fig. 6.6b

DOG #2987 (T16 543-586) (ML)



DOG #2987 (T16 500-543) (ML)

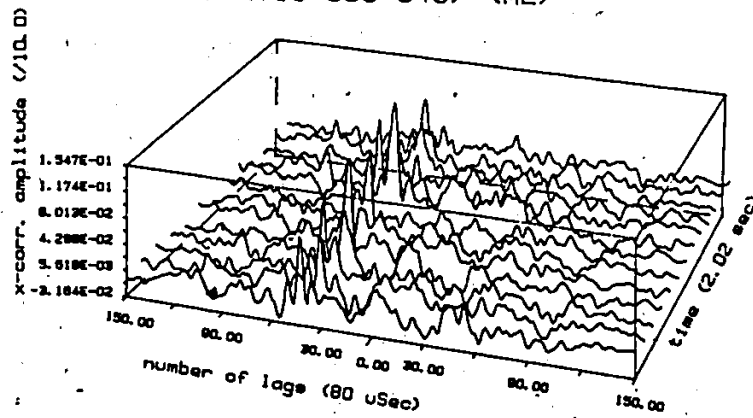


Fig. 6.6c

6.3.3 CROSS-CORRELATION OF HIGHLY DAMAGED NERVE TRUNK SIGNALS

The nerve trunk can easily be damaged during surgical handling or from the cuff compression. An example of the neural signals from a damaged nerve trunk and its corresponding contractile and EMG activity are shown in Fig 6.7. The neural activities recorded at cuff N1 (N11, N12) show burst activities at approximately 5 per minute and synchronized with the antral rate as well as the duodenal contractile activities. The neural activities at cuff N2 (N21, N22), however, are scarce. The cross-correlation of the neural activities of the highly damaged nerve trunk (Fig 6.7, Box A) are shown in Fig 6.8a-c. They illustrate that there are no significant peaks corresponding to either sensory or motor activities. The electron microscopy studies (discussed in Section 6.7) of this nerve trunk enclosed in the nerve cuff show that the nerve trunk is highly damaged with few surviving axons. This suggests that for the highly damaged nerve trunk, the neural signals generated by the surviving nerve fibres are too low, and hence, difficult for the cross-correlation algorithms to estimate the sensory and motor cross-correlation peaks. In a sense, this provides a validation of this technique by showing that false positive neural activity is not recorded.

Fig 6.7. An example of the neural signals N21 and N22 from a damaged nerve trunk and its corresponding contractile and EMG activities. The neural activities from cuff N1 (N11,N12) show bursts occurring at 5 per minute and synchronized with the aptal rate (E2,S2). The neural activities at cuff N2 (N21 and N22), however are scarce. The cross-correlation of the neural activities of Box A is shown in Figs 6.8a to c.

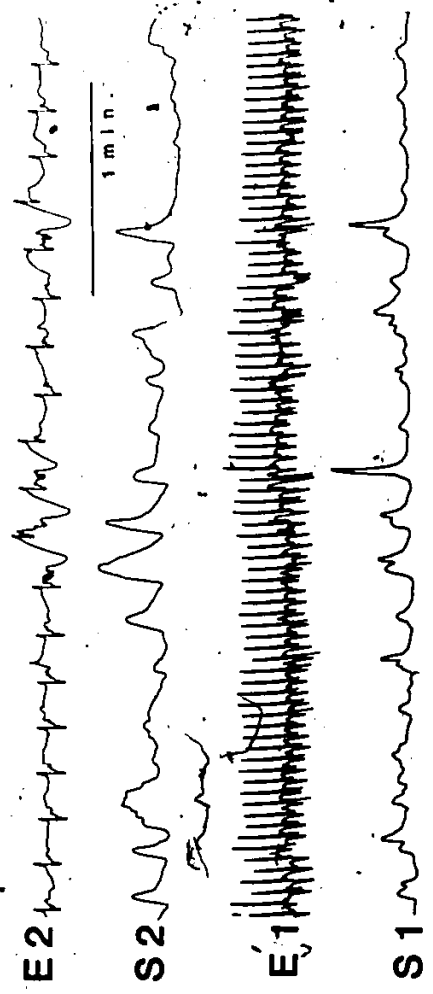
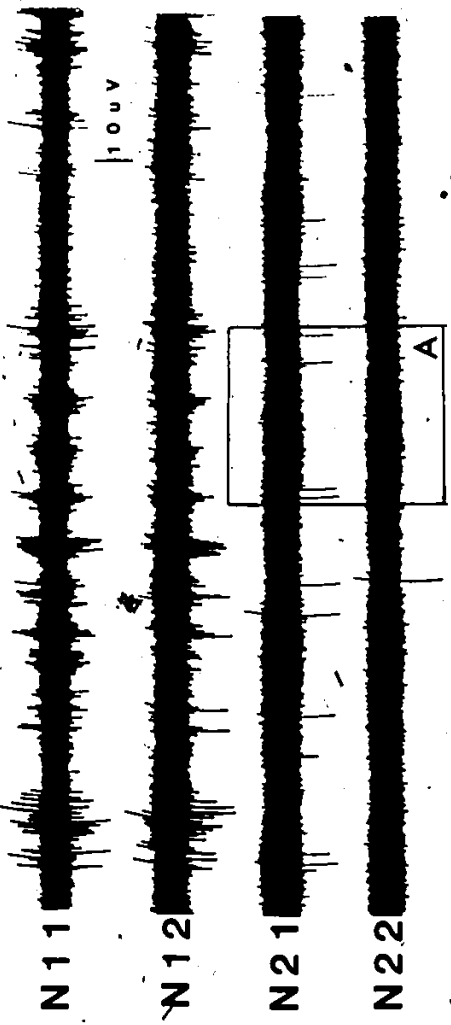
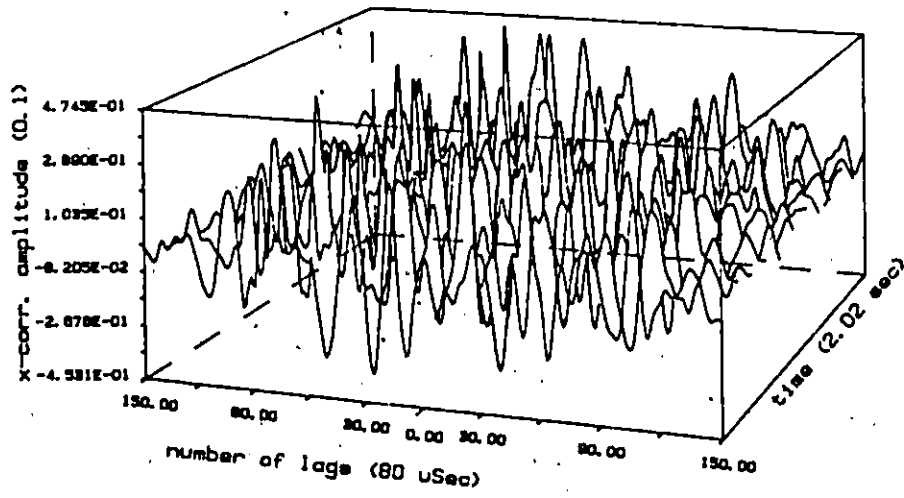


Fig 6.8 The cross-correlation of the neural signals (N21, N22) from a highly damaged nerve trunk (Fig 6.7, Box A). The cross-correlation functions from the three algorithms, GCC, SCOT, and ML (Fig 6.8 a, b, and c, respectively) show that there are no significant peaks corresponding to either the sensory or motor activities.

DOG #3817 (T37 560-600) (GCC)



DOG #3817 (T37 520-560) (GCC)

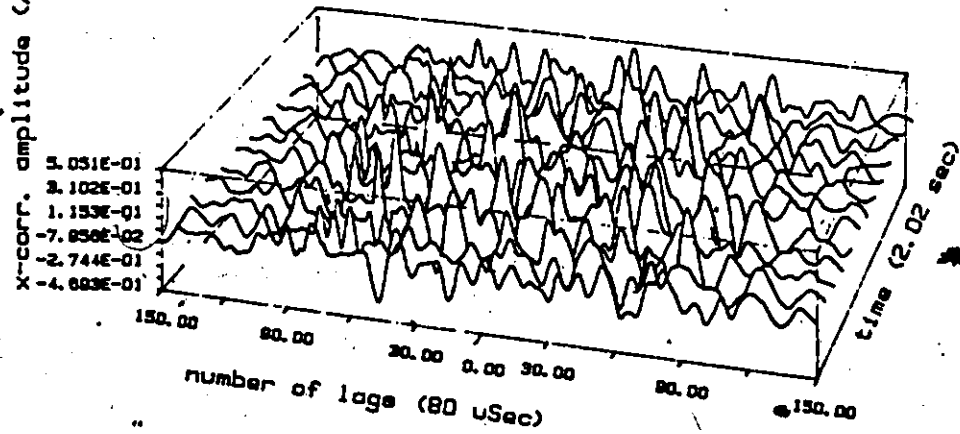
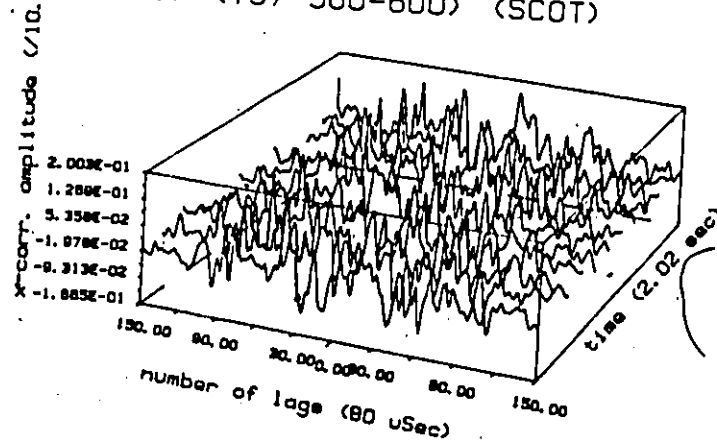


Fig. 6.8a

DOG #3817 (T37 560-600) (SCOT)



DOG #3817 (T37 520-560) (SCOT)

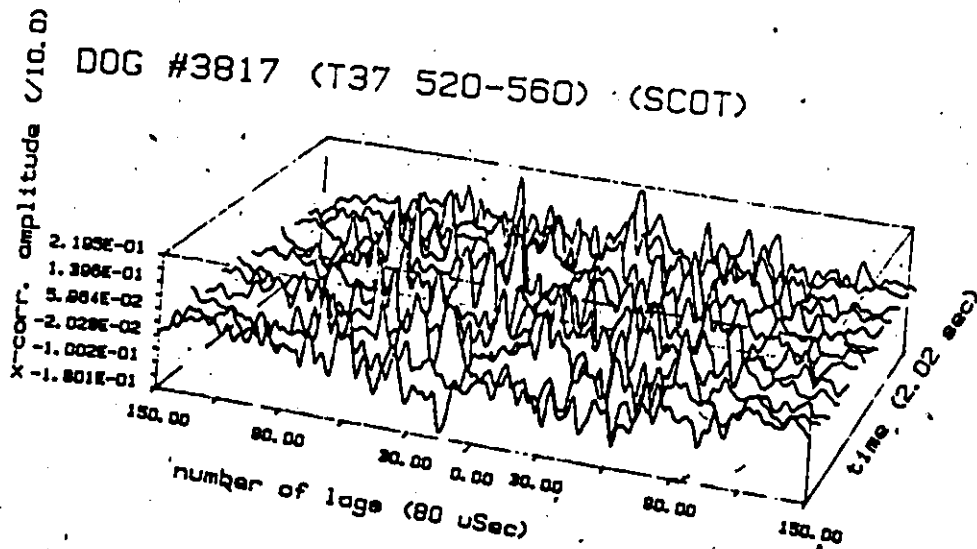
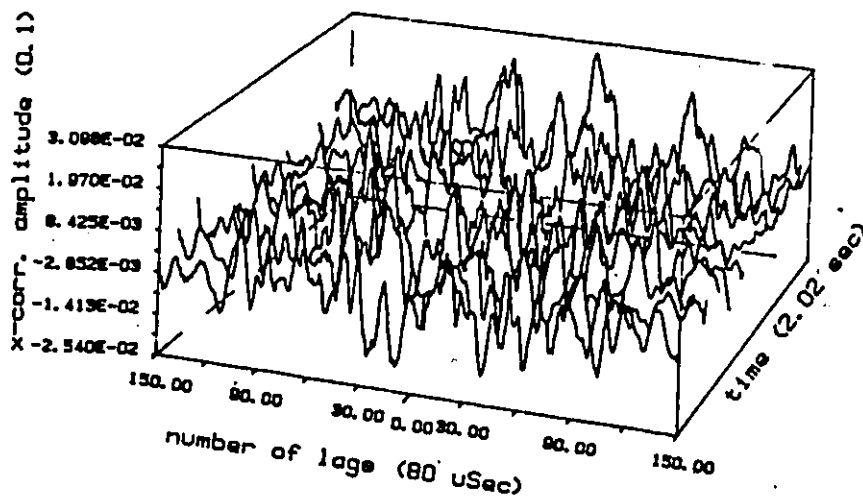


Fig. 6.8b

DOG #3817 (T37 560-600) (ML)



DOG #3817 (T37 520-560) (ML)

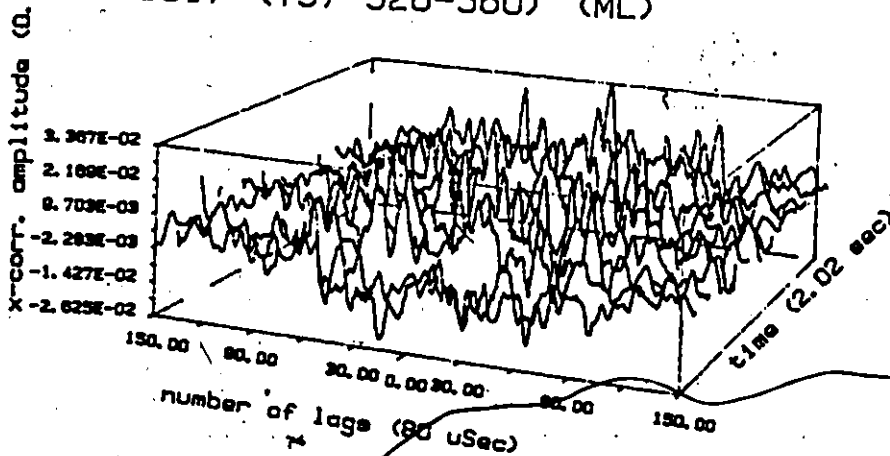


Fig. 6.8c

6.3.4 CROSS-CORRELATION OF CORRUPTED NEURAL SIGNALS

When all the recording instruments are grounded properly, the animals could move around the enclosed recording area without causing any noticeable movement artifacts to the recorded signals. However when an animal is excited and moving quickly and with large jerky motion, there may be movement artifacts in the recorded neural signals as shown in Fig 6.9. The cross-correlation function of that section of the signal is shown in Fig 6.10a-c. Notice the large peak at the zero lag of cross-correlation function of all the three algorithms. This suggests that the two channels of neural signals are closely related at zero lags, i.e. the two signals are similar without any delay. As shown later in the electron microscopy studies (Section 6.7) that majority of the nerve fibres within the nerve trunk of the Nerve of Latarjet are nonmyelinated. The conduction velocities of these fibres are generally slower than 5 meters/seconds. Hence any peaks occurring at less than 20 lags (i.e. faster than 6.25 meters/second) can be considered as artifact.

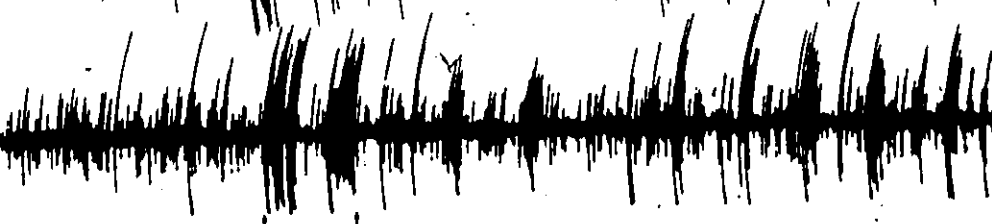
Fig. 6.9 Example of the neural signals corrupted with movement artifacts and the corresponding EMG and contractile activities. (between the upward arrows)



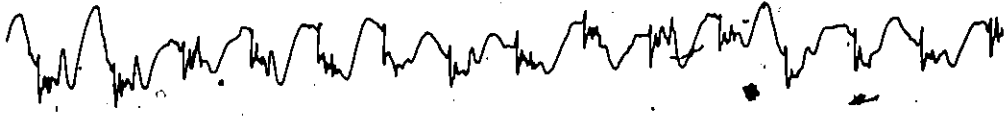
N21



N22



E2



S2



1 min

E1



S1

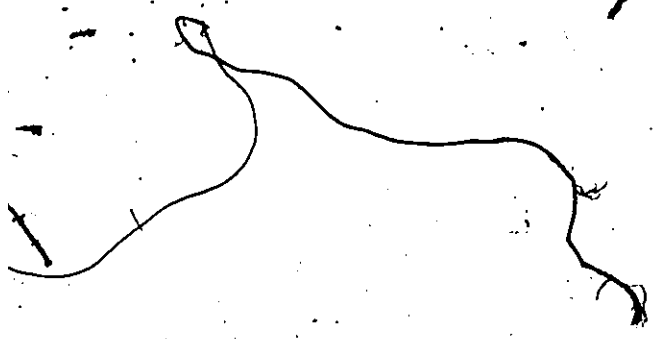
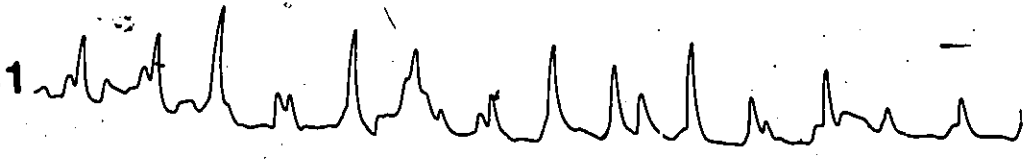


Fig 6.10 The cross-correlation of the neural signals corrupted with movement artifacts. The cross-correlation functions from the three algorithms GCC, SCOT, and ML (Fig 6.10a, b, and c respectively) show large peaks at zero lags suggesting that the two channels of neural signals are closely related.

DOG #3817 (T43 55-100) (GCC)

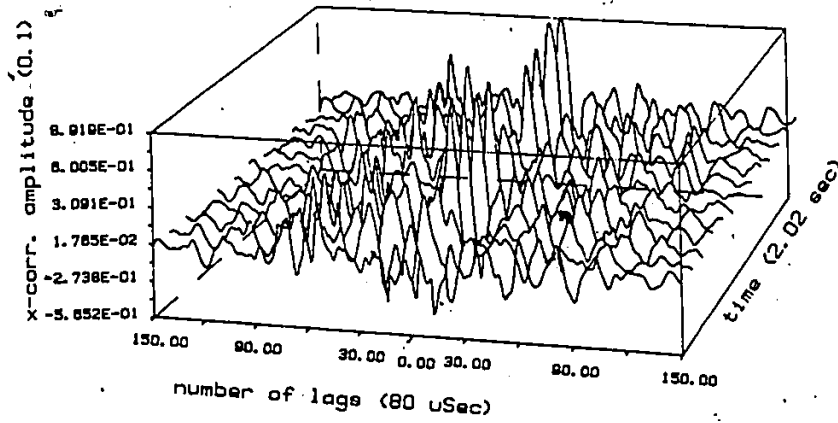


Fig. 6.10a

DOG #3817 (T43 55-100) (SCOT)

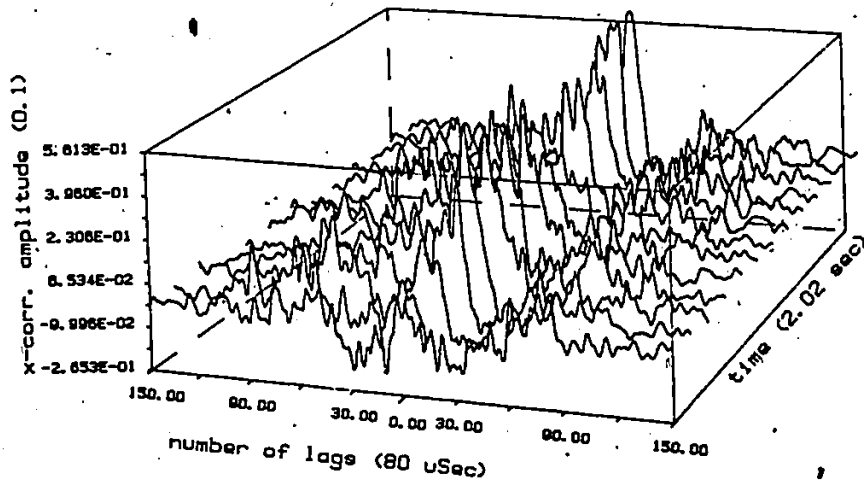


Fig. 6.10b

DOG #3817 (T43 55-100) (ML)

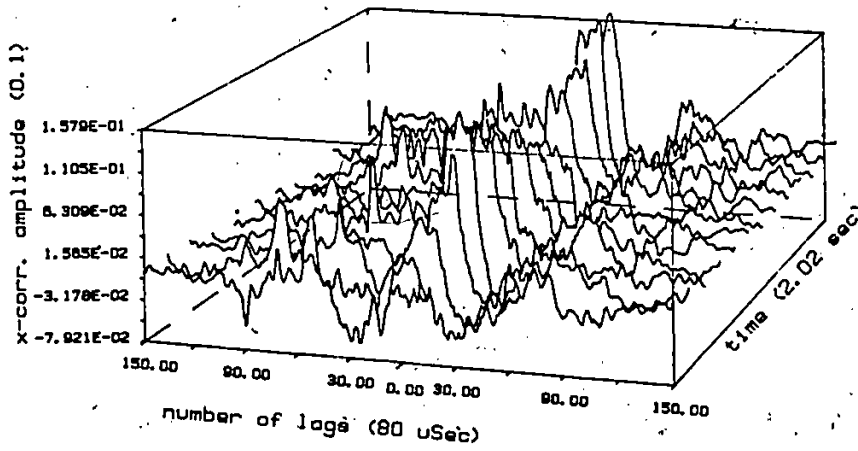


Fig 6.10c

6.4 SENSORY AND MOTOR PATTERNS WITH RESPECT TO THE DURATION OF ELECTRODE IMPLANTATION

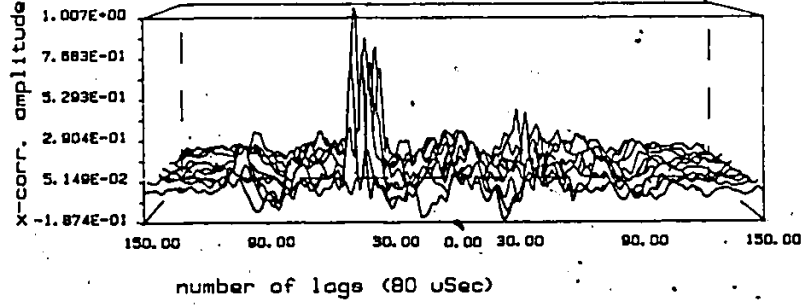
A series of sensory and motor patterns with respect to the duration of the cuff electrode implantation is shown in Fig 6.11. Approximately 15 days after the electrodes are implanted, the average sensory and motor peaks occur at locations 45 ± 10 . These peak locations remain within the same range up to about 60 days after the electrodes are implanted. After that, the cross-correlation peak locations of the sensory components increased to 50 ± 10 lags. After about 90 days, the sensory cross-correlation peak location increased to about 75 ± 15 lags. The location of the sensory cross-correlation peaks with respect to the implanted duration is shown in Fig 6.12.

As mentioned in Section 6.3 the ratio of the number of sensory fibres to the motor fibres is approximately 9 to 1, and the sensory signals occur with and/or without contractile activities. Of course contractile activity may be occurring elsewhere (not recorded). This may be why it is easier to estimate the sensory cross-correlation peak locations than the motor cross-correlation peaks locations. During the early part of the recording period, the motor peaks were detected at about 45 ± 10 lags; after about 50 days, the motor peak location may have increased somewhat to about 50 ± 10 lags. It was difficult to estimate the motor cross-correlation peaks approximately 70 days after the electrode implantation.

Fig 6.11 Series of sensory and motor patterns with respect to the duration of the cuff electrode implantation. Between 17 to 45 days after the cuff implantation, the peaks of the cross-correlation function are at 45 ± 10 lags. After 60 days, the peak locations are 50 ± 10 . After 90 days the peak locations increase to 75 ± 15 .

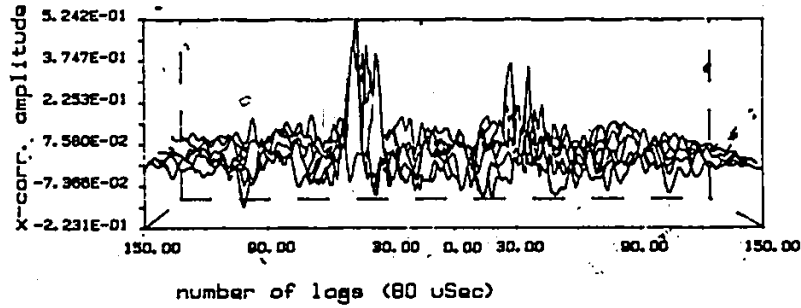
(/10.0)
DOG #2901

DAY 17



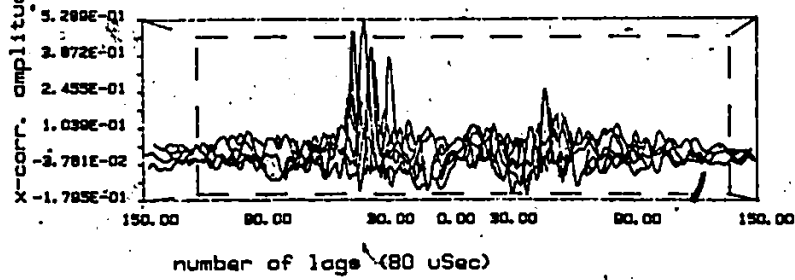
(/10.0)
DOG #3715

DAY 30



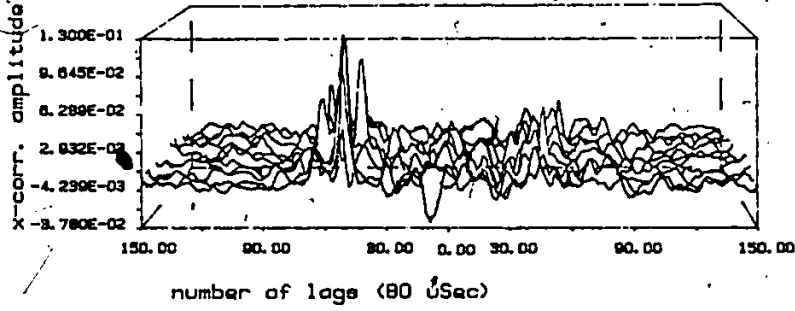
(/10.0)
DOG #2901

DAY 45



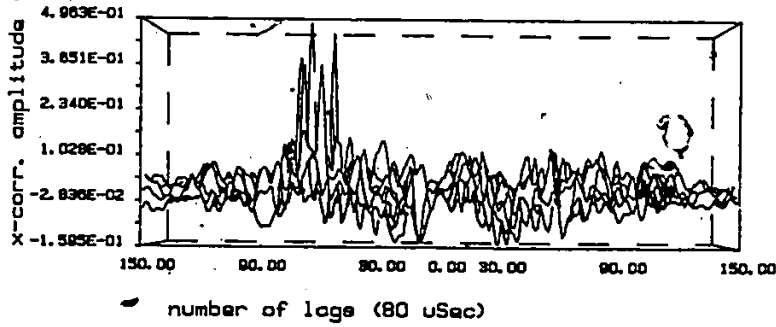
DOG #2987

DAY 60



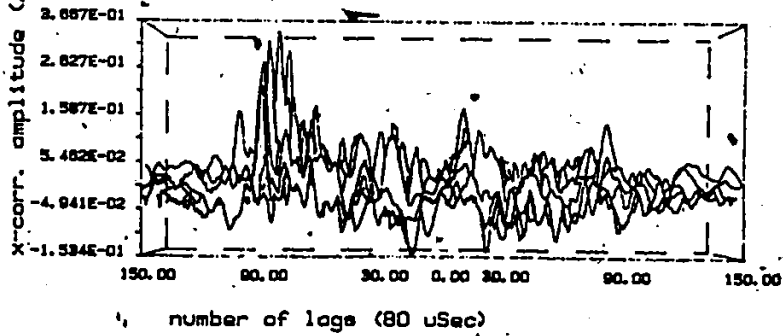
DOG #2901

DAY 75



DOG #3817

DAY 90



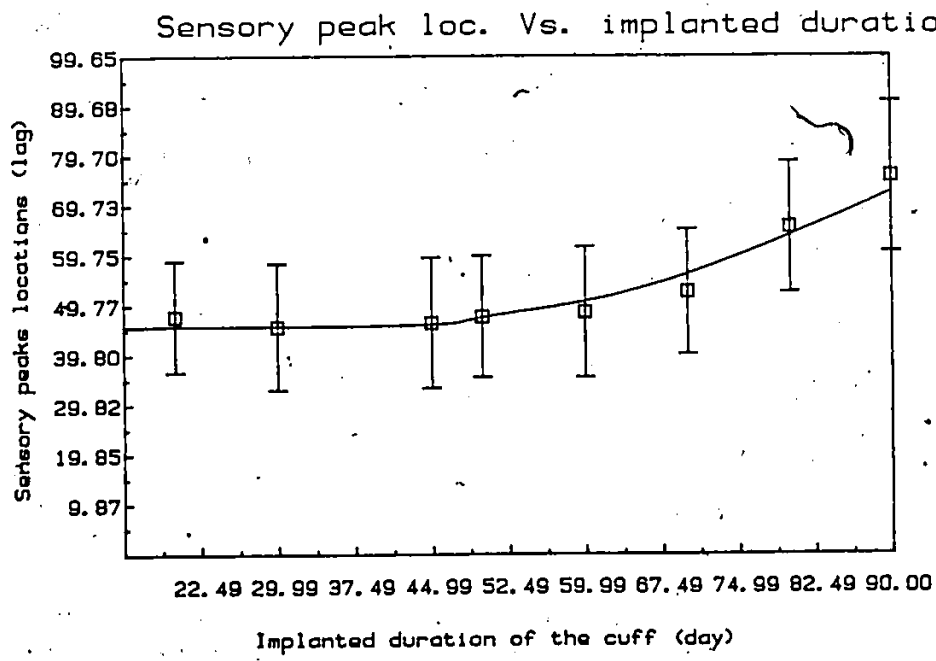


Fig 6.12 Average sensory peak location vs. the implanted duration of the nerve cuff.

6.5 RESULTS OF STIMULATING THE NERVE OF LатарJET WITH CUFF ELECTRODE

The objective of this part of the study was to show that the nerve cuff can be used to stimulate the nerve of Latarjet and consequently affect the GI motility. Two different sets of parameters were used in stimulating one of the nerve cuff: 10v, 6 pulse per second (pps) and 5v, 3 pps, both of 1msec duration. Stimulations were performed approximately 50 days after electrode implantation.

An example of stimulating N2 with the stronger stimulant (10v, 6pps) is shown in Fig 6.14. Approximately 20 seconds after N2 was stimulated, the antrum (S2) relaxed and the contractile activities of the duodenum (S1) increased. About 1 minute after the stimulation has ceased, the contractile patterns of both the antrum (S2) and duodenum (S1) areas returned to their pre-stimulation patterns.

When N2 was stimulated with the weaker stimulus (5 volts, 3 pps) (Fig 6.14), the antrum relaxed more gradually as compared with the stronger stimulant (Fig 6.13). However, as with the stronger stimulation, about 1 minute after the stimulation has ceased, the contractile patterns of both the antrum and duodenum areas appeared to return to the pre-stimulation patterns.

Note that there are almost negligible artifacts caused by the stimulation recorded in the EMG pin electrode. This suggests that the cuff electrode is well insulated such that the electrical activities inside the cuff are well insulated from the outside environment.

Fig 6.13 Results of stimulating the nerve of Latarjet using cuff N2 with stimulus parameters of 10V, 6 pps, and 1 msec in duration. Traces N11 and N12 are neural signals from cuff N1, traces (E2, S2) and (E1, S1) are the EMG and contractions of the antrum and duodenum areas respectively. Approximately 20 seconds after N2 was stimulated, the antrum (S2) exhibits relaxation, but the contractile activities of the duodenal area (S1) increased. Approximately one minute after the stimulation has ceased, the contractile pattern of both antrum (S2) and duodenum (S1) areas returned to their pre-stimulation patterns.

483

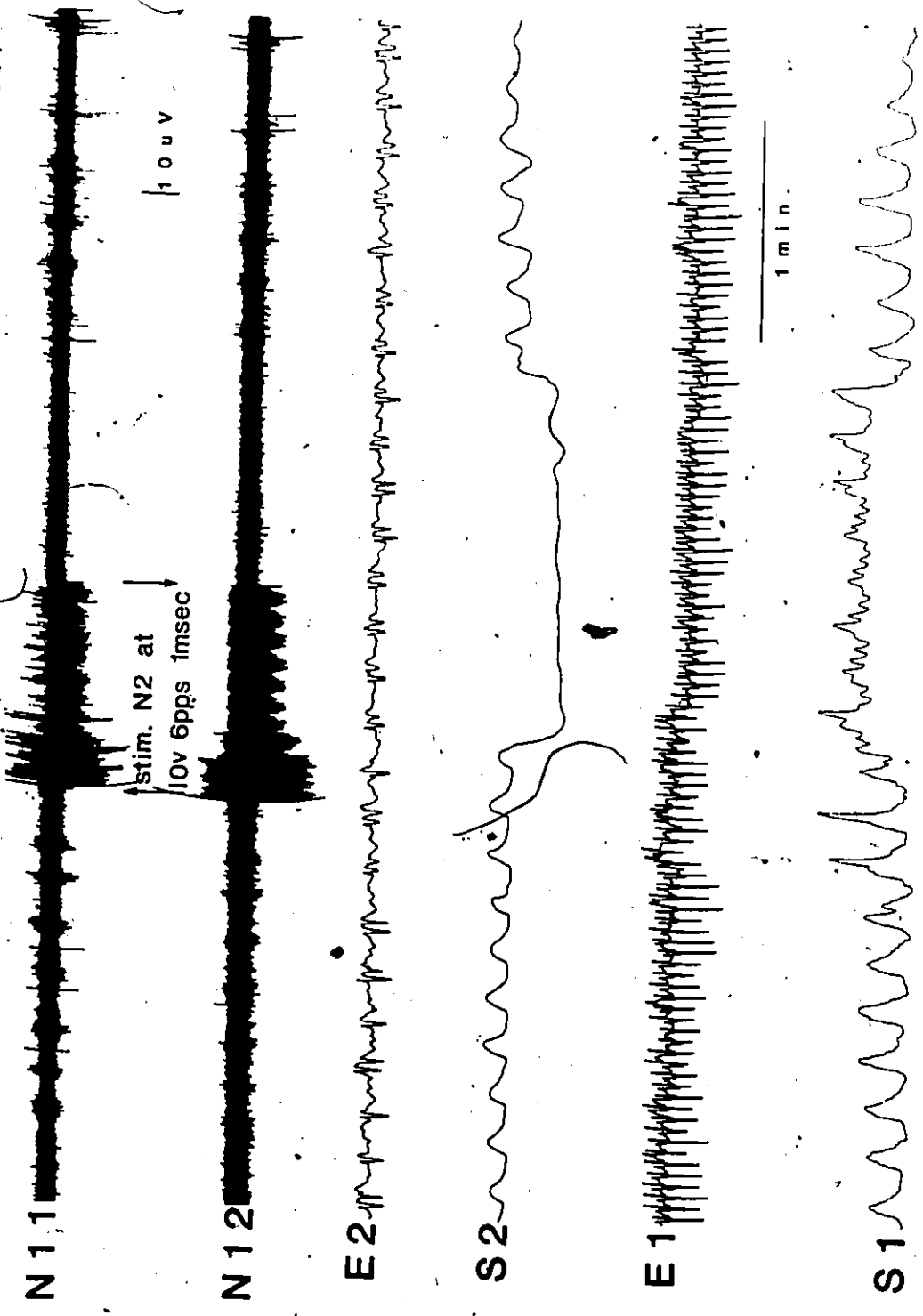
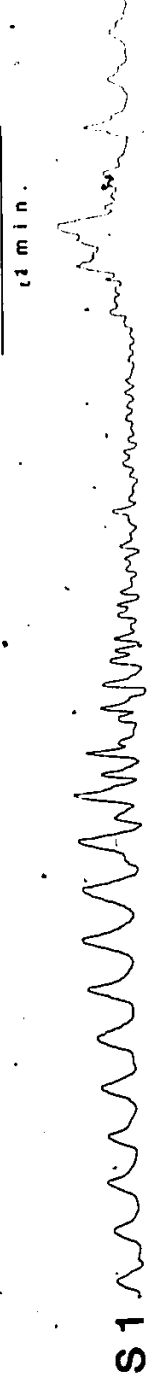
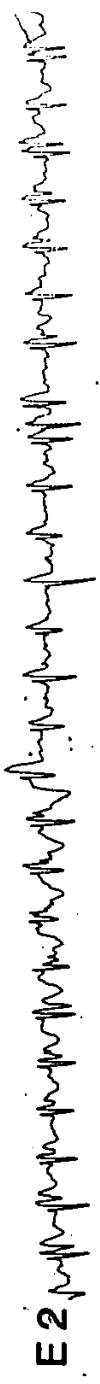
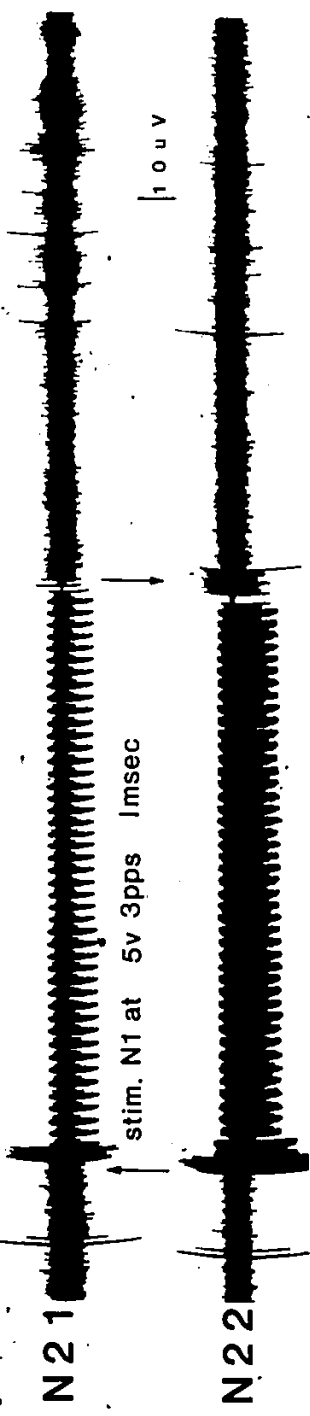


Fig 6.14 Results of stimulating the Nerve of Latarjet using cuff N1 with a parameter of 5 V, 3 pps, and 1 msec of the stimulation. The duodenum on the other hand is characterized by an increase in contractile activity (S1) about 2 minutes after the onset of the stimulation. About 1 minute after the stimulation ceased, the contractile patterns of both antrum and duodenum areas appear to return to their pre-stimulation patterns.

735



6.6 RESULTS OF STIMULATING CERVIC VAGAL NERVE WITH UNITARY IMPULSES

Neural signals normally recorded from the cuff electrode are summations of both sensory and motor nerve impulses firing asynchronously (see Section 2.3). By stimulating the cervical vagal nerve with unitary impulses, synchronized neural impulses from motor fibres can be recorded. This stimulation also should provide further proof that signals from the brain travelling along the vagal nerve to the gastric system can be recorded by the cuff electrode.

The procedure for the preparation of stimulating the cervical nerve and record with the cuff electrode from the nerve of Latarjet is given in the Appendix A. A Hewlett Packard Signal Analyzer System (Model 5480A) operated in the summation averaging mode was used to average the impulses recorded from the cuff electrode. The stimulation impulses from the stimulator (Grass S88, Section 4.4) were used to trigger the averager. Each occurrence of the stimulation impulse triggered the sweep for the averager. An example of an average impulse obtained from 64 sweeps is shown in Fig 6.16. The traces labelled N11 and N12 were obtained from the two recording cuff separated by 10 mm. The time interval (t) between the two impulses was 3.5 msec. (Fig 6.16). Hence the conduction velocity of the motor impulse was $10 \text{ mm}/3.5 \text{ msec}$ i.e. 2.9 M/sec which is approximately the same as found in the cross-correlation methods (Section 6.3.1).

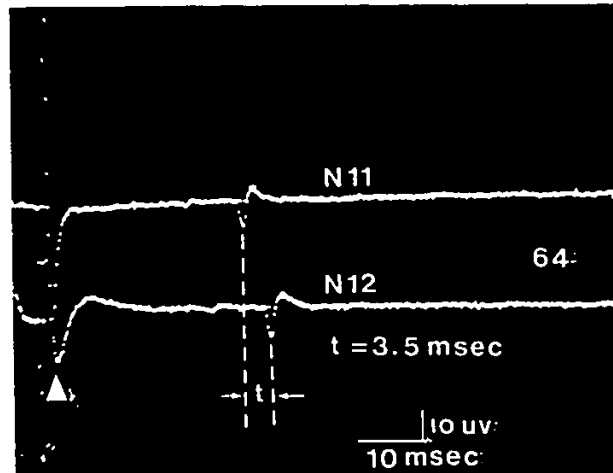


Fig 6.15 Averaged impulse obtained from 64 stimulation impulses from the Cervical vagal nerve. The traces labelled N11 and N12 were obtained from the two recording cuffs separated by 10 mm. The time interval (t) between the two impulses was 3.5 msec, hence the conduction velocity of the impulse from N11 to N12 is $10 \text{ mm} / 3.5 \text{ msec} = 2.9 \text{ m/sec}$.

6:7 ELECTRON MICROSCOPY (EM) STUDIES

The physical condition of the nerve trunk implanted inside the cuff electrode was examined by means of electron microscopy, and compared with that of the control normal nerve trunk of the nerve of Latarjet. The procedure for the preparation of the nerve trunk for the electron microscopy study is given in Section 4.4.2.

The EM studies of the control nerve trunk show that the majority of the axons are grouped in the form of bundles enclosed by Schwann cells. Some axons are individually embedded with Schwann cells; however, the axons are closely packed together, and hence the density of axon is high. Results also show that approximately 1% - 5% of the axons are myelinated and that 95% - 99% of the axons are unmyelinated. The low and high magnification micrograph of the cross-section of a control vagus nerve are shown in Fig 6.17 and 6.19 respectively.

The EM of the nerve trunk enclosed in the cuff electrode after a period of 90 days shown that there is a complete loss of myelinated nerves. Although the majority of the axons are still grouped together in the form of bundles enclosed by Schwann cells, some axons contained within the bundle are damaged. The diameter of the axons are generally smaller, and the intercellular spaces between the axons are greater. Hence, the density of the nerve fibres is lower than that of the control nerve trunk. These results suggest that axons of larger diameters may be selectively damaged or were destroyed. The low and high magnification micrograph of the cross-section of a nerve trunk enclosed within a nerve cuff over a period of 90 days is shown in Fig 6.18 , 6.20

and 6.21 respectively.

The EM of a highly damaged nerve trunk enclosed in the cuff electrode is shown in Fig 6.22. Results show that for a highly damaged nerve trunk, the diameters of the surviving axons are much smaller. It appears that most of the nerve fibres are replaced by loose connective tissue and/or fluids. The density of the nerve fibres is much lower than the less damaged nerve trunks. The nerve signals generated by this nerve trunk are too low to carry out cross-correlation analysis (Section 6.4)

The results of the EM studies also tend to agree with the electrode impedance findings through out the recording period as discussed in the following section.

Fig 6.16 Low magnification micrograph of a cross-section of the vagal nerve (nerve of Lartarjet) from a control dog. The majority of axons (A) are grouped into bundles, which are enclosed by a common Schwann cell (Sc). Some axons are individually embedded with each Schwann cell. Note two myelinated axons (MN). Control vagus from the stomach area contains approximately 1-5% myelinated axons and 95-99% of unmyelinated axons. N - nucleus of Schwann cell x 37300.

Fig 6.17 Low magnification micrograph of a cross section taken from nerve which had been encased in a nerve cuff over a period of 3 months. All axons (A) are grouped into nerve bundles which are enclosed by Schwann cell (Sc). Many nerve bundles contain damaged axons (asterisk). Note a complete absence of myelinated fibres. N - nucleus of Schwann cell x 48600.

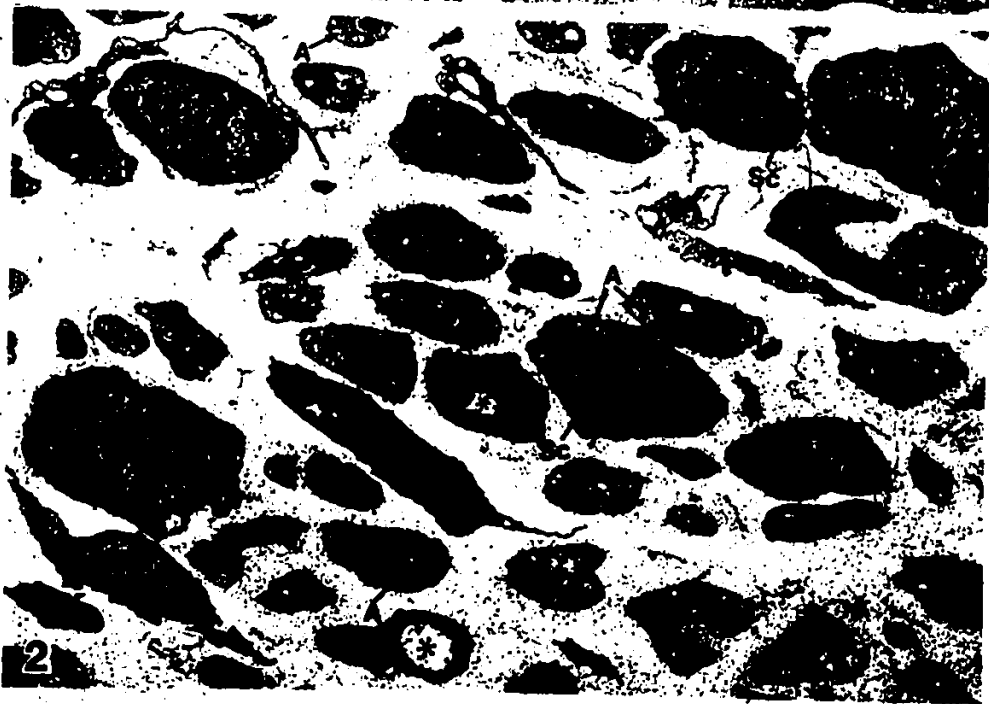


Fig 6.18 High magnification micrograph of a cross-section of a control vagus. All axons (A) are enclosed by the cytoplasm of the Schwann cells (Sc), M-mitochondria, lgv- large granular vesicles. x15800

Fig 6.19 High magnification of a cross-section taken from nerve which had been enclosed in a nerve cuff over a period of 3 months. All axons (A) are grouped into nerve bundles. Majority of the bundle contain damaged axons (asterisk). Note the axons sizes are smaller in comparison with the control axons (figure 6.18). lgv - large granular vesticles. X15800.

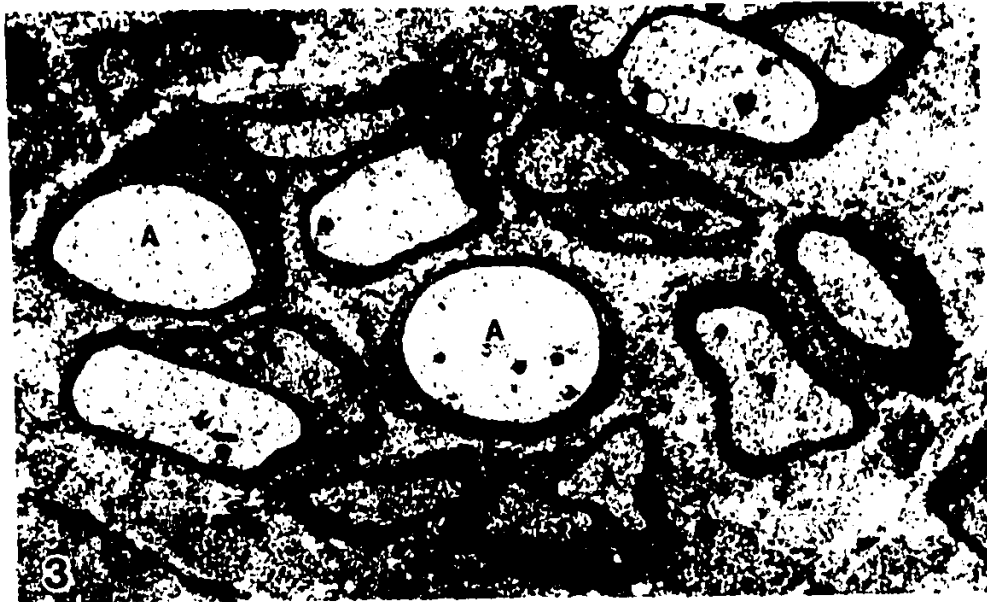
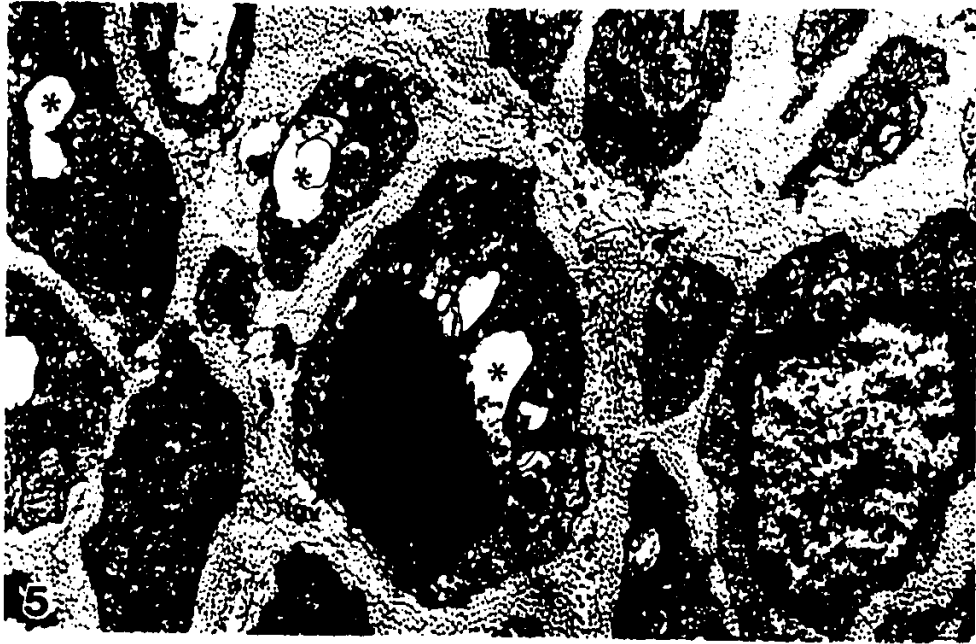


Fig 6.20 Cross section of a nerve which had been enclosed in the nerve cuff over a period of 3 months. Note the aggregation of large granular vesticles (lgy) in the central nerve bundle. Schwann cell, A-axon, N-nucleus of Schwann cell, asterisk- damaged nerve fibre. X169000

Fig 6.21 Cross section through severely damaged vagus, which had been enclosed in a nerve cuff over a period of 3 months. Note a low density of nerve bundles which consists of a small number of axons (A). Some Schwann cells (Sc) contain no axons. X66800



6.8 IMPEDANCE MEASUREMENT OF THE CUFF ELECTRODE

The impedance of the cuff electrode was measured between the center and the outside rings of the cuff (Section 4.4.1) for a frequency range of 1Q to 5 KHz using a Hawlett Packard Vector Impedance meter (Model 4800A). The measured impedances were plotted in 3-dimensions with the impedance as a function of the frequencies and the number of days after the nerve cuff implantation. The impedance measurements for the average normal cuffs and cuffs with highly damaged nerve trunk are shown in the following.

6.8.1 IMPEDANCE OF AVERAGE NORMAL CUFF ELECTRODES

The average impedances of six cuff electrodes as a function of frequency and days is shown in Fig 6.23. During the initial period after the cuff implantation, the impedance at the low frequency range (10 - 100 Hz) was high (about 47 k Ω at 10 Hz) but decreased gradually until about 14 days after the implantation, then the impedance remained steady throughout the recording periods (about 17 k Ω at 10 Hz). The impedance for the higher frequency range (500 - 5 KHz) increased approximately 20% about 50 days after the implantation, but began to decrease after then. This can possibly be explained in conjunction with the findings in the EM studies (Section 6.7) and the cross-correlation studies (Section 6.4). During the initial recording period (before 50 days), there is probably some growth of connective tissue in the nerve cuff, hence the impedance at the high frequency range increases

somewhat. Approximately 50 days after the cuff implantation, the higher impedance myelinated axons and axons of larger diameters probably begin to be damaged or destroyed and replaced with lower impedance tissue or fluids (Section 6.7).

6.8.2 IMPEDANCE OF CUFF ELECTRODES WITH HIGHLY DAMAGED NERVE TRUNKS

The average impedance of three cuff electrodes with the indication of highly damaged nerve trunk are shown in Fig 6.24. Results show that immediately after the implantation (for about 30 days), the impedance measurements were similar to those of the normal cuffs (see above Section). After approximately 30 days the impedance at the low frequency (10 Hz) decrease slowly, while the impedance at higher frequency range decline sharply. From day 35 to day 80, the average impedance at 1 KHz decreased from approximately $2K\Omega$ to 700Ω .

This result is consistent with the finding from the EM study of the nerve trunk and the cross-correlation of the neural signals generated, that only a few nerve fibres may have survived in the nerve trunk.

The discussion of this Chapter is given in the following Chapter.

IMPEDANCE MEASUREMENT OF A CUFF ELECTRODE

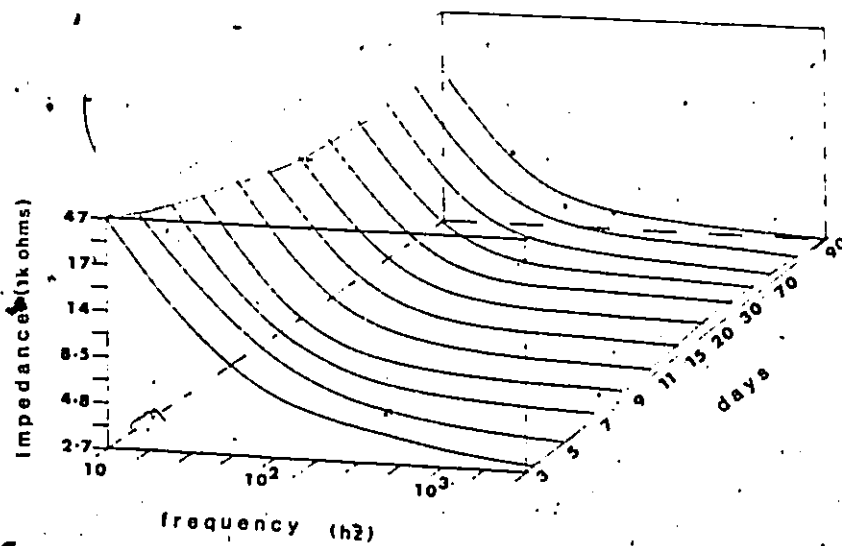


Fig 6.22 The average impedance of 6 cuff electrode as function of frequency and days.

IMPEDANCE MEASUREMENT OF A CUFF ELECTRODE

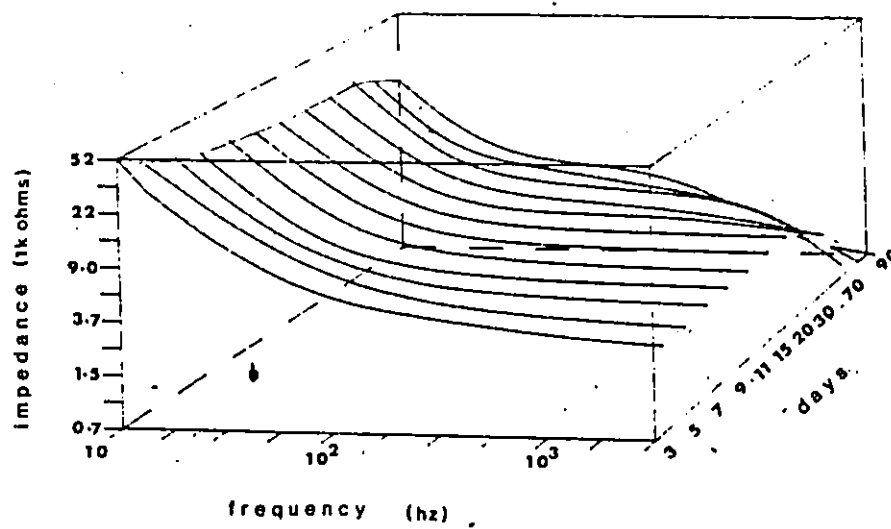


Fig 6.23 The average impedance of three cuff electrodes with highly damaged nerve trunks.

CHAPTER VII

DISCUSSIONS

7.1 INTRODUCTION

The performances of the three algorithms in estimating the cross-correlation functions and the delay times have been shown in Chapter V, the applications of the three algorithms in analyzing neural signals have been shown in Chapter VI. In this chapter a discussion of the simulation results and the analysis of the neural signals are given.

7.2 SIMULATION OF THE ALGORITHMS

The simulated results show that with the three types of simulated data (i.e., GWN, sinewave, and impulses) as inputs to the sensory $s(t)$, and motor $m(t)$ terminals (Fig. 3.5b), the simple GCC cross-correlation algorithm can estimate the peak locations as well as the SCOT and ML methods when the SNR is greater than approximately -3 dB. However, the cross-correlation peaks in SCOT and ML methods are sharper and narrower than those of the GCC method. When the SNR is approximately between -3 dB and -12 dB, the performance of the algorithms depends on the nature of the input data ($s(i)$ and $m(i)$): When

the data sequences are GWN, the SCOT and ML methods do not have significant advantage over the GCC method in estimating the peak locations (Fig. 5.3). For the SCOT method, although the peak values of the cross-correlation function are greater than by the ML method (Fig. 5.2), the standard deviation of the estimation increases as the SNR decreases (Fig. 5.1). When the data contains tonal components, such as simulation with the SINE or IMP, both SCOT and ML methods perform better than the GCC method in estimating the peak locations (Fig. 5.11 and Fig. 5.19). As the SNR decreases to below approximately -12 dB, both SCOT and ML show no any significant advantage over the GCC method. These factors are discussed in more detail below.

7.2.1 GCC Method:

It is known that smoothed power spectral estimates are more precise when the signal is Gaussian i.e., when it exhibits a flat spectrum. Any large peak in such a spectrum for example, due to a periodic component, will be distorted during computation because of the effect of a spectral window spreading the power from the large peaks into adjacent frequency components [Jenkins and Watts, 1968]. Reciprocally, the cross-correlation using the GCC method will exhibit distortions. These distortions can be minimized by passing the data through a filter to reduce the amplitude of these dominant frequencies. Such a procedure is known as pre-whitening [Bendat and Piersol, 1971]. The SCOT method can be interpreted as a pre-whitening filter that divided the estimated cross-spectrum, $G_{xy}(f)$ with the estimated PSDs of

$x(i)$ and $y(i)$ (Eq. 3.46, and Eq. 4.25). The ML method can also be termed as a pre-whitening filter but weighted with the signal-to-noise ratio at each frequency. These are discussed in more detail below.

7.2.2 SCOT Method:

The weighting function for SCOT is the reciprocal of the square root of the sum of the PSD of $x(i)$, $G(f)$ and PSD of $y(i)$, that is

$$\Omega_{\text{gSCOT}}(f) = \frac{1}{\sqrt{G_{xx}(f) + G_{yy}(f)}} \quad 7.1$$

from Eq. 3.46. Substituting the expressions for $G_{xx}(f)$ and $G_{yy}(f)$ into Eq. 7.1, then

$$\Omega_{\text{gSCOT}}(f) = \frac{1}{\sqrt{(G_{ss}(f) + G_{mm}(f) + G_{n1n1}(f))(G_{ss}(f) + G_{mm}(f) + G_{n2n2}(f))}} \quad 7.2$$

where $G_{ss}(f)$ and $G_{mm}(f)$ are the power spectra of the sources $s(i)$ and $m(i)$ respectively;

$G_{n1n1}(f)$ and $G_{n2n2}(f)$ are power spectra of the noises $n1(i)$ and $n2(i)$ for $s(i)$ and $m(i)$ respectively.

If the power spectra of the noises $n1(i)$ and $n2(i)$, ($G_{n1n1}(f)$ and $G_{n2n2}(f)$) are much greater than $G_{ss}(f) + G_{mm}(f)$ at all frequencies except at a few frequencies where $G_{ss}(f)$ and $G_{mm}(f)$ are at maximum then, from Eq. 7.2, the SCOT weighting function is approximately the reciprocal of the square root of the product of the two noise spectra, i.e.

$$\Omega_{\text{gSCOT}}(f) = \frac{1}{\sqrt{(G_{n1n1}(f)G_{n2n2}(f))}} \quad 7.3$$

Consequently, the weighting function at these frequencies is much less than 1, hence the estimated cross-correlation function at these frequencies is low. However at those frequencies where $G_{ss}(f)$ and $G_{mm}(f)$ are maximum and greater than the noise spectra, from Eq. 3.47 and 7.2, the square root of the coherence function is approximately

$$C(f) = \exp(j2\pi f\tau_m) + \exp(-j2\pi f\tau_s) \quad 7.4$$

Hence the cross-correlation functions using the SCOT method, which is the inverse Fourier Transform of the square root of the coherence function (Eq. 7.4), yields two narrow pulses at the locations τ_m and τ_s of the +lag and -lag of the cross-correlation function (Figs. 5.4 - 5.6, 5.12 - 5.14, and 5.20 - 5.22). Note that when the noise spectrum is much larger than $G_{ss}(f)$ and $G_{mm}(f)$ at their maximum, the phase information of Eq. 7.4 is no longer useful, and hence the SCOT method provides no advantage over the GCC method.

7.2.3 ML Method:

For the ML method, the weighting function $\Omega_{\text{gML}}(f)$ is given in Eq. 3.49. From the definition of the coherence function (eq 3.47) and its re-arrangement, the ML weighting function can be expressed as

$$\Omega_{\text{gML}}(f) = \frac{|G_{xy}(f)|^2}{G_{xx}(f)G_{yy}(f) - |G_{xy}(f)|^2} \cdot \frac{1}{|G_{xy}(f)|} \quad 7.5$$

By substituting the power spectra $G_{xx}(f)$, $G_{yy}(f)$, and the cross spectrum $G_{xy}(f)$ of the denominator of the above expression (Eq. 7.5) with their corresponding compositions (Eq. 3.49), the weighting function can be expressed as

$$\Omega_{\text{gML}}(f) = \frac{|G_{xy}(f)|}{(G_{ss}(f) + G_{mm}(f) + G_{n1n1}(f))(G_{ss}(f) + G_{ss}(f) + G_{n2n2}(f)) - G_{ss}^2(f) - G_{mm}^2(f) - 2G_{ss}(f)G_{mm}(f)\cos(\tau_m + \tau_s)} \quad 7.6$$

By expanding the denominator and dividing both the numerator and denominator by the product of the noise spectra $G_{n1n1}(f)$ and $G_{n2n2}(f)$, Eq. 7.6 can be expressed as

$$\Omega_{\text{gML}}(f) = \frac{|G_{xy}(f)|}{G_{n1n1}(f)G_{n2n2}(f)} \cdot \frac{1}{1 + \frac{(G_{ss}(f) + G_{mm}(f))}{G_{n1n1}(f)} + \frac{(G_{ss}(f) + G_{mm}(f))}{G_{n2n2}(f)} - \frac{2G_{ss}(f)G_{mm}(f)\cos(\tau + \tau)}{G_{n1n1}(f)G_{n2n2}(f)}} \quad 7.7$$

For low SNR conditions, the noise power spectrum is much greater than

the source spectra $G_{ss}(f)$ and $G_{mm}(f)$; the above expression can be simplified to

$$\Omega_{gML}(f) = \frac{|G_{xy}(f)|}{G_{n1n1}(f)G_{n2n2}(f)} \quad 7.8$$

Note that in Eq. 7.3 the weighting function for the SCOT is approximately the reciprocal of the square root of the product of the two noise power spectra. Hence for low SNR the ML weighting functions can be interpreted as the SCOT weighting function with additional SNR weighting, that is

$$\Omega_{gML}(f) = \frac{\sqrt{(G_{ss}^2(f) + G_{mm}^2(f) + 2G_{ss}(f)G_{mm}(f)\cos(\tau_m + \tau_s))}}{\sqrt{(G_{n1n1}(f)G_{n2n2}(f))}} \Omega_{gSCOT}(f) \quad 7.9$$

For the GWN, SINE, and IMP inputs, the ML method results exhibit two extra smaller peaks at the $2\tau_m + \tau_s$ and $2\tau_s + \tau_m$ locations on the +lags and -lags sides of the cross-correlation function. Since these two smaller peaks occur only when analyzing with the ML method, the problem is clearly due to the ML weighting function $\Omega_{gML}(f)$ (Eq. 3.49). As shown above, the ML weighting function can be re-expressed as Eq. 7.5.

This can further be simplified to

$$\Omega_{gML}(f) = \frac{|G_{xy}(f)|}{G_{xx}(f)G_{yy}(f) - |G_{xy}(f)|^2} \quad 7.10$$

The absolute value of the cross-spectrum between $G_{xy}(f)$ can be expressed as

$$|G_{xy}(f)| = \sqrt{G_{ss}^2(f) + G_{mm}^2(f) + 2G_{ss}(f)G_{mm}(f)\cos(\tau_m + \tau_s)} \quad 7.11$$

Hence, besides the power spectrum of the sensory components, $G_{ss}(f)$, and the motor components, $G_{mm}(f)$, there is a cross-multiplication term, $2G_{ss}(f)G_{mm}(f)\cos(\tau_m + \tau_s)$. Consequently the cross-correlation functions using the ML method, which is the inverse Fourier Transform of the ML weighting function (Eq. 7.5) multiply by the cross spectrum, $G_{xy}(f)$, yields two extra smaller peaks at locations $2\tau_m + \tau_s$ and $2\tau_s + \tau_m$. These two extra smaller peaks are not noticeable when the SNR is less than 0 dB (Fig. 5.6, 5.14, 5.22). In the case of neural signals, the SNR is usually much less than 0 dB, hence ML method should not introduce any ambiguity problem in determining the cross-correlation peaks.

7.3 ANALYSIS OF THE NEURAL SIGNALS

Results of the neural signals (Chapter VI) illustrate that the cannula system can be used to stimulate as well as record the extrinsic neural signals together with myoelectric and contractile activities. The sensory and motor patterns can be recognized from the measured compound neural signals using the cross-correlation algorithms. The condition of the nerve cuff electrode and the enclosed nerve can be monitored with the impedance measurement. The amount of damage to the

nerve trunk caused by the nerve cuff can be evaluated by electron microscopic studies.

In order for the cuff electrode to be able to record neural activities chronically, the cuff electrode must be stable and bio-compatible. The stability of the cuff electrode and the conditions of the enclosed nerve trunk can be monitored by measuring the impedance of the electrode through out the recording period [Polak, 1974; and Stein, 1978]. The cuff impedance at the low frequency range is mainly due to the the Pt-Ir wire electrode to tissue and fluid interface which is mainly capacitive in nature. The impedance at the high frequency range is mainly due to the resistance of the tissue and fluid across the Pt-Ir electrodes within the nerve cuff (Section 4.4.1). Changes in the impedances generally reflect changes in the nerve diameter and/or growth of connective tissue within the nerve cuff [Dymond, 1976]. In this study, the three dimensional display of the impedance measurements provides a more informative view of the trend of changes in cuff impedance with respect to the implanted duration.

The results of the impedance measurement of the normal (section 6.8.1) and highly damaged (section 6.8.2) nerve trunk can possibly be explained in conjunction with the findings in the EM studies (Section 6.7) and the cross-correlation studies (Section 6.4). During the initial recording period (before 50 days), there is probably some growth of connective tissue in the nerve cuff, hence the impedance at the high frequency range increase somewhat. Approximately 50 days after the cuff implantation, the higher impedance myelinated axons and axons of larger diameters probably begin to be affected, damaged, or destroyed and

replaced with lower impedance tissue or fluids (Section 6.7). Results of the impedance measurement of highly damaged nerve trunk (see Section 6.8.2) provide another indication of nerve trunk damage: the impedance measurement at the high frequency decreases sharply with respect to the implanted duration (Fig. 6.23) reflecting the possibility of the replacement of the higher impedance axons with lower impedance connective tissue and fluids.

Results from the EM studies suggest that axons of larger diameter may be selectively damaged or destroyed. Other investigators (Ochoa et al, 1972; Weiss and Hiscoe, 1948; and, Stein and Olsen, 1975) found that when a nerve trunk was compressed, nerves of larger diameter were selectively damaged or injured. This possibly explains the loss of myelinated axons and axons of larger diameter. These EM study results also suggest that the size of the cuff electrode is important in recording neural signals. If the cuff is too tight, majority of the nerve fibres could be destroyed. If the cuff electrode is too loose, connective tissue could grow between the electrode wires and the nerve trunk and decrease the amplitude of the recorded neural signals.

Results from the cross-correlation patterns show that both SCOT and ML methods are better estimators than the GCC method in analyzing the compound neural signals. This is also true in the case of tonal components (see Sections 5.4 and 5.5). The performance of the SCOT and ML methods are similar, except that the amplitudes of the cross-correlation from the ML method are significantly lower and the variance of the cross-correlation from the ML method is also lower. It was shown in Section 7.2.3 that when the SNR is low, the performance of the ML

method approaches that of the SCOT method weighted with the signal-to-noise ratio. In this study with low SNR conditions, the cross-correlation peaks from the SCOT method are higher than those by the ML method. Even though the variance of estimated cross-correlation from the ML method is lower than the SCOT method, it is less ambiguous in locating the peak in the SCOT than the ML method. If the SNR can be improved by improving the data acquisition methods (discussed in the next chapter), then the ML method should be better than the other two methods, because the cross-correlation peak values would be higher, and hence more accurate in estimating the cross-correlation peak locations.

It is known that the major motility functions of the gastric system are storage, mixing, and/or propulsion. In order to facilitate these functions, information from all the involved control systems, i.e. myogenic, hormonal, and neural (both extrinsic and intrinsic) control systems, must somehow be integrated. It is unlikely that the extrinsic neural system or other control system is the sole controller of gastric motility.

During the onset of the contractile activities, there are consistent neural burst activities involving motor and sensory impulses with the former usually preceding the latter (see Fig 6.1 and 6.5 for example). These bursts at 5 per minutes are synchronized with the EMG (ECA and ERA) activities of the corpus and antral areas. These bursts of activities, however, also occur when there are no contractile activities recorded (Figs 6.1, and 6.2). However, the possibility that the nerves are "driving" contractile activity at an unrecorded site cannot be ruled out. Sarna and Daniel (1975) showed that there was a

segmental arrangement of the innervation of intrinsic nerves by branches of the nerve of Latarjet and that the arrangement affects anterior and posterior faces of the stomach. The strain gauges in this study recorded only the anterior face. Since the recorded neural activities are the combination of both motor and sensory activities, the extrinsic neural activities reflect not only the contractile activities but also other activities such as the chemical properties of gastric contents or of the hormonal levels. Thus another possibility is that this activity represents primarily sensory activity.

The alternate burst patterns in the adjacent nerve trunk suggests that the neural activities also relate to the propagation of the EMG activities aborally. These results also suggested that in order to study the relationships of the various nerve trunks regulating or affecting their corresponding regions, it is necessary to monitor different nerve trunks innervating the corresponding regions of the gastric system. Most of the components with the compound neural signals are probably sensory corresponding to the gastric condition from the corpus to the antrum (Fig 6.3).

The results in sensory and motor neural patterns show that the motor activities reach maximum before the peak of the contractile activities, whereas the sensory activities are at the highest during the peak of the contractile activities (Fig 6.5). Also during quiescent periods, the cross-correlation algorithms cannot detect motor activities. These results suggest that the initiation of contractile activities may be due, directly and/or indirectly, to the motor impulses from the CNS. The sensory activities generated by the mechanoreceptor

corresponding to the muscle contraction may provide a feedback limitation to contraction. Roman and Milan (1980), in their indirect nerve suture study also found that before a contraction in the corpus there is a sharp rise in motor activity. Hall et al (1981), in their cervical vagus nerve cooling studies show that by blocking the nerve traffics between the CNS and the gastric system, the normal gastric contractile patterns are completely abolished. They, therefore, concluded that the vagus was the controller for the gastric contractile activities. Glystone et al (1985), however, disagree with Hall's findings that the vagus was the controller of the gastric contractile activities. Instead of blocking the vagal nerve traffic at the cervical level, they blocked the traffic at the thoracic level and observed that the gastric contractile pattern persists. They hence concluded that signals from the CNS travelling down vagal nerve cannot be the controller for the gastric contractile activities. However they did not carry out ultrastructural studies of the nerve trunk on which the cooling devices were implanted. Thus it is possible that they were dealing with a kind of vagotomy caused by selective loss of large nerve fibres and that adaptation might have occurred [Wilbur and Kelly, 1973; Kelly and Codes, 1969; Hall et al 1970]. If signals from the CNS are not the controller of the gastric contractile activities, then how does the CNS influence the gastric contractile activities via the vagal nerve pathways? In order to answer the above question, one must investigate the distribution of the sensory and motor activities from the Nerve of Latarjet within a period of gastric motility pattern known as gastric cycle during fasting. In a dog this cycle lasts for approximately 90

minutes [Hall et al, 1982]. Although the results of this study do not show the distributions of the sensory and motor neural activities from the nerve of Latarjet in controlling the gastric contractile patterns within a gastric cycle, the results shown in this thesis demonstrate that the technique can be used to investigate such problems.

The increase in the cross-correlation peak locations (lags) with respect to the implanted duration is somewhat puzzling. This can possibly be explained in conjunction with the results obtained in the EM study and the impedance measurement (see Sections 6.7 and 6.8). It is known that nerve-fibres of larger diameter can propagate faster than the smaller diameter nerve fibres [Waxman, 1980; Rushton, 1951; Moore, 1978]. Results from the EM studies shown that after a period of cuff implantation, the majority of the nerve fibres damaged or destroyed appear to have been those of the large diameters. Also the overall density of nerves decreases per unit area. Results from the impedance measurement suggested that after a period of cuff implantation, some of the higher impedance nerve fibres are replaced by the connective tissue or fluid of lower impedance. Hence as the cuff implantation duration increases, the contribution of the signals generated by the larger nerve fibres decrease, and hence the recorded compounded nerve signals are probably due to the fibres of smaller diameter. This possibly explain the increase of the cross-correlation peaks location, i.e. the decrease in conduction velocity.

The results of stimulating the Nerve of Latarjet is contrasted with the findings by Daniel et al (1978). Their results show that stimulation of the nerve of Latarjet caused contractions. The

stimulation parameters and experimental conditions, however, are different between our methods. Daniel et al used impulses of 5 msec. duration in an acute situation as compared with impulses of 1 msec. duration in a chronic environment in this study. In Daniel's study the nerves just proximal to the stimulation were ligated to prevent afferent stimulation. In this study, stimulation from the nerve cuff causes both efferent and afferent stimulations. Unless more control experiments can be implemented in a chronic environment; e.g. blocking the afferent nerve traffic at the cervical vagal nerve by cooling [Hall et al, 1982], it is difficult to compare the differences between our results. Another possible explanation for the antral relaxation after stimulation of the nerve of Latarjet is that the majority of the excitatory fibre in the cuff electrode responsible for the antral contraction may be destroyed and stimulation of the nerve excite the inhibitory nerve or sensory nerves and produce relaxation type of motility. It is known that the nerve of Latarjet consists of both inhibitory and excitatory types of nerve [McSwiney, 1931, and Martinson, 1963], and the diameter of the inhibitory fibres is generally smaller than the excitatory fibres [Martinson, 1965]. Results from the EM studies of the nerve trunk inside the nerve cuff showed that all the myelinated nerves are abolished and the damaged or destroyed nerve fibres were mostly of larger diameters. Together with the condition that stimulation is performed 60 days after the cuff implantation, this possibly explains why the stimulation of the nerve of Latarjet resulted in antral relaxation.

Conclusion and suggestion for the further studies are discussed in the following chapter.

CHAPTER VIII

CONCLUSION AND SUGGESTIONS FOR FURTHER STUDIES

8.1 CONCLUSIONS

This thesis demonstrates that the cannula system developed here can be used to simultaneously monitor the vagal nerve, myoelectric, and contractile activities in chronic dogs. The nerve cuff electrode can be used to stimulate as well as to record nerve activities. Three cross-correlation algorithms were implemented and studied for their performance characteristics with different types of simulated data. GI neural signals were also analyzed with the algorithms.

The application of the cross-correlation algorithms to simulated results indicated that:

- 1) with GWN type of inputs, the GCC method could locate the cross-correlation peaks as well as the SCOT and ML methods, however the peaks obtained from the SCOT and ML methods were much narrower
- 2) with SINE and IMP types of inputs, both SCOT and ML methods were superior compared to the GCC method in locating the cross-correlation peaks; and,
- 3) in low signal-to-noise conditions, the performance of the ML method approached that of the SCOT method with an signal-to-noise ratio as an additional weighting factor.

The animal experiments provided results including:

- 1) synchronized nerve activities that corresponded with antral EMG and contractile activities;
- 2) nerve activities that appeared to alternate between adjacent nerves;
- 3) changes in contractile and nerve patterns upon nerve stimulation as compared to those before stimulation;
- 4) sensory and motor patterns in the compound nerve signals;
- 5) approximately constant impedance of cuff electrodes 14 days after cannula implantation; and,
- 6) cuff electrodes caused complete loss of myelinated axons and selective loss of unmyelinated axons of larger diameter within the enclosed nerve trunk approximately 90 days after the cuff implantation.

Based on this thesis work and the subsequent analysis, it can be concluded that :

- 1) the cannula system can simultaneously monitor the vagal neural, the myoelectric, and contractile activities in chronic dogs;
- 2) the microcomputer system (IBM PC/XT) is efficient and economical in processing the biological signals;
- 3) the cross-correlation algorithms can be used to study sensory and motor patterns of the compound nerve signals with the SCOT and ML methods providing superior results than the GCC method;
- 4) the condition of the implanted cuff can be monitored with impedance measurement throughout the recording period;
- 5) the amount of nerve damage caused by the cuff electrode can be

- gauged with impedance measurement and EM studies;
- 6) the cannula system makes it possible to explore crucial topics on nerve traffics associated with normal and abnormal gastrointestinal motility patterns; and,
 - 7) further development is needed to improve the design of the cuff-electrode to minimize the nerve damage and, therefore, increase the signal-to-noise ratio.

8.2 SUGGESTIONS OF FURTHER STUDIES

There are two areas that require further studies: 1) data acquisition and 2) physiological significance as discussed below.

8.2.1 IMPROVEMENT IN DATA ACQUISITION

The following suggestions deal with improving data acquisition and reducing cost.

- (1) **Eliminating the Transformer:** The purpose of the transformer is to match the amplifier noise impedance and passively step-up the source voltage. The transformer (see Section 4.5) however is bulky, heavy, and costly (\$72.00 each). An alternative is to implant a low noise amplifier module in the abdominal cavity. The design of the amplifier is given in Appendix B. The noise level of the amplifier is 3 μV pp with the frequency range of 100-5K Hz. With an amplifier gain of 50, the neural signal after the implanted amplifier will be in the range of 0.1-0.5 mV. This range

- should be less susceptible to environmental noise.
- (2) Improvement of The Nerve Cuff Electrode Design and Use on Smaller Animals: An ideal nerve cuff electrode should be light weight, perfectly fitting the nerve trunk diameter, and smooth surface. Such an ideal electrode can possibly be fabricated after more experience is gained in their design. One of the major costs of this study is the cost of animal (dogs) and cost of surgery for the electrode implantation. These costs can be reduced by reducing the dimensions of the cuff electrode and used on smaller animal, such as rats.
- (3) Recording with Analog Multiplexer and Demultiplexer: In order to monitor the gastric motility, a large number of electrodes for neural, EMG and contractile activities are required. However, at present, the number of channels of signals that can be recorded on the tape recorder is eight (see Section 4.4). Because of the low frequency nature of the EMG and contractile activities, these signals can be multiplexed then recorded on the tape recorder; demultiplexing upon playback from the tape recorder will provide the recorded signals. The design and circuit for a multiplexer and demultiplexer have been developed and implemented (Appendix C). The circuit is capable of multiplexing signals of 8 channels into 2 with a maximum frequency of 1k hz. This will further reduce the cost of such studies and the system can be applied to other biological signal recordings.

8.2.2 PHYSIOLOGICAL SIGNIFICANCE

Some physiological significant projects, as per this thesis work, are mentioned below:

(1) Pattern of Sensory and Motor Activities with Respect to Physiological Conditions :

(i) Vagal control in the cyclic motor activity of the stomach and small intestine: The contribution of vagal activities in the control of Migrating Myoelectric Complex (MMC) of the stomach and small intestine has been a controversial topic [Hall et al, 1982; and Gleysteen et al, 1985]. A study of sensory and motor patterns should provide a clear illustration of the distribution of the vagal activities associated with the initiation of various phases of the Migrating Myogenic Complex.

(ii) Feeding Patterns: The distribution of sensory and motor activities during fed and fasted states remains unclear. Such studies should help in understanding the contribution of the neural activities during the digestive process.

(iii) Stress Patterns : It is known that stress can affect GI motility and alter its GI function. This is probably an important adaptive response to stress in humans [Almy, 1973; Thompson and Heaton, 1980]. Again, the distribution of sensory and motor patterns under stress can help to explain the disordered GI motility caused by abnormal neural activities.

(2) Patterns of Sensory and Motor Activities in Control Conditions:

- (i) Local distension: neural activities associated with distension at various locations of the GI system (e.g. esophagus, fundus, antrum, and duodenum) can be studied by distending the corresponding area with a balloon;
- (ii) Nerve Blocking: Using cooling technique, proximal and distal to the nerve cuff electrode, the sensory and motor activities can be blocked respectively. This should help isolate the signals from the nerve cuff as either sensory or motor responses.

Finally, after the sensory and motor activities are well understood, these nerve cuff electrodes can be used to emulate the natural nerve activities by stimulating the nerve trunk at the appropriate moment and, therefore, regulate the gastrointestinal motility.

REFERENCES

- Alvarez, W.C., "Early studies of the movements of the stomach and bowel", In: Handbook of Physiology, section 6, volume 4: Motility, ed. By C.F. Code, Williams & Wilkins, Baltimore, p.1573-1578, 1968.
- Almy T.P. : "The gastrointestinal tract in man under stress", In: Gastrointestinal Disease, Eds. by Sleisenger M, Fordtran J. Philadelphia, Saunders, 1973
- Abrahamsson H. : "Studies on the inhibitory nervous control of gastric motility", ACTA Physiol. Scand. Suppl. 390:1-38, 1973
- Agostini E, Chinnock J.E., Daly M.deBurgh, and Murray J.G.: "Functional and histological studies of the vagus nerve and its branches to the heart, lungs and abdominal viscera in the cat", J. Physiol 135:182-205, 1957
- Bass P., and Wiley J. N.: "contractile force transducer for recording muscle activity in unanesthetized animals", J. Appl. Physiol. 32, 567-570, 1972
- Bendat J.S. : "Statistical errors in measurement of coherence functions and input/output quantities", J. Sound and Vibration 59(3):405-421, 1978
- Bendat J.S. and Piersol A.G. : Random Data: Analysis and Measurement Procedures, New York: John Wiley and Sons, Inc., 1971
- Bendat J.S. and Piersol A.G. : Engineering Applications of Correlation and Spectral Analysis, New York: John Wiley and Sons, Inc., 1980
- Blackman R.B. and Tukey J.W. : The Measurement of Power Spectra, New York: Dover, 1958
- Bortoff A.: "Myogenic control of intestinal motility", Physiol. Review 56: 418-434, 1976
- Bortoff A.: "Electric activity of gastrointestinal muscle", In: Freidman M. H. P. (ed) Functions of the Stomach and Intestine, Baltimore, Maryland, University Park Press, pp. 17-29, 1975
- Bortoff A.: "Recording of extracellular electrical activities". In: Daniel E. E. and Paton D. M. (ed.) Methods in Pharmacology Vol. 3. New York, Plenum Press, pp185-199, 1975
- Bozler E. "The relation of the action potentials to mechanical activity in intestinal muscle", Am. J. Physiol. 146, 496-501, 1946

- Burnstock G.: "Autonomic innervation and transmission", Brit. Med. Bull. vol 35(3), pp 255-262, 1979
- Cannon W. B. : "The mechanical factors of digestion", In: Hill L. and Bulloch W. (ed) International Medical Monographs, New York, Longmans, Green & Co. 1911
- Carter G.C., Nuttall A.H., and Cable P.G. : "The smoothed coherence transform", Proc. IEEE, vol.61, pp. 1497-1498, Oct. 1973
- Carter G.C., Knapp C.H., and Nuttall A.H. : "Estimation of the magnitude-squared coherence function via overlapped fast Fourier transform processing", IEEE Trans. on Audio Electroacoustics, vol.Au-21, pp. 337-344, 1973
- Code C.F., Szurzewski J.H., Kelly K.A. et al: "A concept of control gastrointestinal motility", In: Code C.F., and Heidel W. (ed) Handbook of Physiology, Section 6, Alimentary Canal, Vol. V. Washington D.C., American Physiology Society, pp 2881-2896, 1968
- Cragg B.G. and Thomas P.K. : "The relationships between conduction velocity and the diameter and internodal length of peripheral nerve fibres", J. Physiol (Lond.) 136:606-614, 1957
- Daniel E.E. and Chapman K.M.: "Electrical activity of the gastrointestinal tract as an indications of mechanical activity", Am. J. Dig. Dis. 8:54-102, 1963
- Daniel E.E. and Irwin J. : "Electrical activity of the gastric musculature", In: Code C.F., and Heidel W. (ed) Handbook of Physiology, Section 6, Alimentary Canal, Vol. IV. Motility. Washington D.C., American Physiology Society, pp 1969-1984, 1968
- Daniel E.E. And Sarna S.K.: "Organization of vagal fibres to control gastric motility", Gastroenterology 68, Part 2:A-22/879, 1975
- Daniel E.E. and Sarna S.K.: "Distribution of excitatory vagal fibres in canine gastric wall to control motility", Gastroenterology 71:608-613, 1976
- Daniel E.E. : "Nerve and motor activity of the gut", In: Nerves and the Gut, Edited by F.P. Brooks and P.W. Evers, pp154-196. C.B.Slack, Inc. Thorofare, 1977
- Daniel E.E., Fox J.E.T., Oki M, Domoto T., Sakai Y., Yanaihara N., and Track N.S. : "Study of peptides in control of motility", In: Functional Disorders of the digestive tract, chapter 11, ed. by Chey W.Y., Raven Press, New York, 1983
- Daniel E.E., Walter B., Honour A.J., and Bogoch.: "The relationship between electrical and mechanical activity of small intestinal of dog and man", Can. J. Biochem. Physiol. 38:777-791, 1960

- Davison J.S. and Grundy D.: "Modulation of single vagal efferent fibre discharge by gastrointestinal afferents in the rat", J. Physiol. (Lond.) 284:69-82, 1978
- Davison J.S.: "Innervation of the gastrointestinal tract" : In a guide to gastrointestinal motility; ed. by Christensen J. and Wingate D., pp 1-47 Weight. PSG, 1983.
- Davenport W.B.Jr. : Probability and Random Processes, New York: McGraw-Hill, 1970
- Debas H.T., Yamagishi Y., and Dryburgh J.R.: "Motilin enhances gastric emptying of liquids in dogs", Gastroenterology 73:777-782, 1977
- Debas H.T., Farooq O. and Grossman M.I.: "inhibition of gastric emptying is a physiology action of cholecystokinin", Gastroenterology 68:1211-1217, 1975
- DeLuca C.J. And Gilmore L.D.: "Voluntary nerve signals from severed mammalian nerves: long-term recordings", Science, 191:193-195, 1976
- Ducker T.B. And Hayes G.T.: "Experimental improvements in the use of silastic cuffs for peripheral nerve repair", J. Neurosurg., 28:582-587, 1968
- Dymond A.M. : "Characteristics of the metal-tissue interface of stimulation electrodes", IEEE Trans. Bio. Med. Eng. BME vol.23, pp274-280, 1976
- Fisher R.A. : "Tests of significance in harmonic analysis", Proc. Roy. Soc. London, Ser. A125:54-59, 1920
- Fox J.E.T., Jury J., Daniel E.E., and Track N.S.: "Gastrointestinal motility and regulatory peptide concentration", In Gut Hormones, ed. by Bloom S.R. and Polak J.M., pp504-508. Churchill-Livingstone. Edinburgh.
- Fox J.E.T., Daniel E.E., Jury J., Fox A.G., and Collins S.M.: "Sites and mechanisms of action and neuropeptides on canine gastric motility differ in-vivo and in-vitro", Life Sciences 33:817-825, 1983
- French A.S. and Holden A.V. : "Frequency domain analysis of neurophysiological data". Comp. Prog. Bio-med. 1:219-234, 1971
- Furness J.B., and Costa M.: "Types of nerves in the enteric nervous system", Neuroscience 5:1-20, 1980
- Gershon M.D., and Erde S.M. : "The nervous system of the gut", Gastroenterology 80:1571-1594, 1981

- Gordon T.: "Sensory modulation and motor patterns during locomotion in normal and denervated hindlimbs", Can. Physiol. 4:161 1979.
- Grundy D., Salih A.A., and Scratchard T.: "Modulation of vagal efferent fibre discharge by mechanoreceptors in the stomach, duodenum, and colon of the ferret", J. Physiol. 319:43-52, 1981
- Glass G.B.J.: "Gastrointestinal Hormones",: In Comprehensive endocrinology, Raven Press. 1980
- Hall W. H. and Read R. C.: "Effect of vagotomy on gastric emptying", Am. J. Dig. Dis. 15. 1047-1052, 1970
- Hall K.E., El-SHarkawy T.Y., and Diamant N.E.: "Vagal control of migrating motor complex in the dog", Am. J. Physiol., 243:G276-G284, 1982
- Hannan E.J. : Time Series Analysis, John Wiley and Sons, New York, 1960
- Hannan E.J. and Thomson P.J. : "the estimation of coherence and group delay", iometrika, Vol.58, pp.469-481, 1971
- Hassab J.C. and Boucher R.E.: "Optimal estimation of time delay by a generalized correlator," IEEE Trans. Acoust, Speech, Signal Processing, vol. ASSP-27, pp373-380, 1979
- Hodgkin A.L. : The conduction of nerve impulses, Springfield, IL., Charles C. Thomas, 1964
- Hodgkin A. L. and Huxley A. F.: "A quantitative description of membrane current and its application of conduction and excitation in nerve," J. Physiol. (Lond.), 117, 500-544, 1952
- Hodgkin A. L. and Huxley A. F.: "Measurement of current-voltage relations in the membrane of the giant axon of Loligo," J. Physiol. (Lond.) 116, 424-448, 1952
- Hoffer J.A., Stein R.B., and Gordon T.: "Differential atrophy of sensory and motor fibres following section of cat peripheral nerves," Brain Res. 178:347-361, 1979
- Holden A.V. : Models of the Stochastic Activity of Neurones, Springer-Verlag, New York, 1976
- Hunt J. N. and Spurrell W. R.: "The pattern of emptying the human stomach," J. Physiol. (London) 113, 157-168, 1951
- Hursh J.B.: "Conduction velocity and diameter of nerve fibres," Am. J. Physiol. 127:131-139, 1939

- Jahnberg T., Abrahamsson H., Jansson G. et al: "vagal gastric relaxation in the dog," Scand. J. Gastroenterol. 12,221-224, 1977
- Jenkins G.M. and Watts D.G. :Spectral analysis and its applications, San Francisco, CA : Holden-Day, 1968
- Katz B. : Nerve, muscle, and synapse, McGraw-hill Book Co., 1966
- Kelly K.A., and Code C.F.: "Effect of transthoracic vagotomy on canine gastric electric activities," Gastroenterology, 57:51-58, 1969
- Kelly K.A.: "Canine gastric motility and emptying: electric, neural and hormonal controls," Pro Fourth Internat Symp on Gastrointestinal Motility, E.E. Daniel et. Al. (eds.), Mitchell Press, Vancouver, pp.463-470, 1974
- Kosterlitz H.W. : "Intrinsic and extrinsic nervous control of motility of the stomach and the intestines," In : Handbook of physiology, section 6, Alimentary Canal, vol. 4. Ed. by Code C>F> p2147-2171, American Physiological Society. Washington D.C. 1968
- Knapp C.H. and Carter G.C.: "The generalized correlation method for estimation of time delay," IEEE Trans. Acoust., Speech, Signal Processing, Vol ASSP-24 pp 320-307, Aug. 1976
- Milon J.P., and Roman C. : "Discharge of efferent vagal fibres supplying gastric antrum: indirect study by nerve suture technique," Am. J. Physiol., 235:E366-E373, 1978
- Martinson J., and Muren A.: "Excitatory and inhibitory effects of vagus stimulation on gastric motility in cat," Acta Physiol. Scand., 57:309-316, 1963
- Martinson J.: "Study on the efferent vagal control of the stomach," Acta Physiol. Scand., [Suppl. 255], 65:1-23, 1965
- Mendel C., Pousse A., Lambert A. et al.: "Recording of canine intestinal chronic longitudinal movements," In: Christensen J. (ed.) Gastrointestinal Motility, New York, Raven Press, pp323-330, 1979
- Moore J.W, Joyner R.W., Brill M.H, Waxman S.G., Najar-Joam : "Simulations of conduction in uniform myelinated fibres. Relative sensitivity to changes in nodal and internodal parameters," Biophys J. 21:147-160, 1978
- Nuttall A.H. and Carter G.C. : "A generalized framework for power spectral estimation," IEEE Trans. Acoust., Speech, Signal Processing, vol. ASSP-28, no.3 pp. 334-335, June 1980
- Ochoa J., Fowler T.J., and Gilliatt R.W. : "The anatomical changes in peripheral nerves compressed by a pneumatic tourniquet," J. Anat. 113:433-455, 1972

- Oppenheim A.V. and Schaffer R.W.: Digital Signal Processing, Englewood Cliffs, N.J.: Prentice-Hall, 1975
- Otnes R.K. and Enochson L. : Digital Time Series Analysis, New York: Wiley, 1972
- Papoulis A. : Probability, Random Variables, and Stochastic Processes, McGraw-Hill series in System Science, 1965
- Papazova M. and Atanassova : "Changes in the bioelectric activities of the stomach after bilateral transthoracic vagotomy," Bull. Inst. Physiol. 14:121-133, 1972
- Pollak V. : "Impedance measurements on metal needle electrodes," Medical and Biological Engineering, 12:606-612, 1974
- Rector R. and Alexy G. : The 8086 Book, Osborne/McGraw-Hill, Berkeley, California, 1980
- Reddy S.N., Daniel E.E., Yu J.J.L, and Belback L. : "Processing of gastrointestinal EMG for contractile signals", Proceeding of 35th ACEMB conference, Philadelphia (1982).
- Reddy S.N., Daniel E.E., Yu J.J.L, Waterfall W.E., and Belback L., "Processing of GI spike activity for contractile signals," Dig. Dis and Sc. V.27-7, 1982
- Robinson E.A.: "A historical perspective of spectrum estimation", Proc.IEEE. vol 70, no.9 pp. 885-907, Sept. 1982
- Roman, C., "Nervous control of esophageal and gastric motility," In: Mediators and Drugs' in Gastrointestinal Motility I: Morphological Basic and Neurophysiological control., Edited by G. Bertaccini, Springer-Verlag, Berlin, pp.223-278, 1982.
- Roth P.R.: "Effective measurements using digital signal analysis", IEEE Spectrum, vol.8, pp 62-70, Apr.1971
- Ruch T.C. and Patton H.D. : Physiology and Biophysics, Philadelphia & London, Saunders, 1965
- Rushton WAH : "A theory of the effects of fibre size in medullated nerve," J Physiol (Lond) 115:101-121, 1951
- Sarna S.K., Daniel, E.E., and Kingma, Y.J., "Simulation of slow wave electrical activity of small intestine," Am. J. Physiol., 221:166-175, 1971.
- Sarna S.K., Daniel E.E., and Kingma, Y.J., "Simulation of the control activity of the stomach by an array of relaxation oscillators," Am. J. Dig. Dis., 17:299-310, 1972

- Sarna S.K., and Daniel, E.E. : "Vagal control of gastric electrical control activity and motility", Gastroenterology 68:301-308, 1975
- Scarborough K, Ahmed N. and Carter G.C. : "on the simulation of a class of time delay estimation algorithms," IEEE Trans. Acoust., Speech, Signal Processing, vol. ASSP-29, no.3 pp.534-539, June, 1981
- Shannon C.E. : "A mathematical theory of communication," Bell Syst. Tech. J. 27:623-656, 1948
- Szurszewski J. H.: "Electrical basic for gastrointestinal motility," In: Johnson L.R. (ed.) Physiology of The gastrointestinal Tract Vol. 6. New York, Raven Press, pp. 1435-1466 1981
- Stein R.B. : "A theoretical analysis of neuronal variability," Biophys. J. 5:173, 1965
- Stein R.B. : Nerve and Muscle Membranes, Cells, and Systems, Plenum Press, 1980
- Stein R.B., Charles D., Davis L., Jhamandas J., Mannard A., and Nichols T.R.: "Principles underlying new methods for chronic neural recording," The Canadian Journal of Neurological Sciences, 2:235-244, Aug. 1975
- Stein R.B., Charles D., Gordon T., Hoffer J., and Jhamandas J.: "Impedance properties of metal electrodes for chronic recording from mammalian nerves," IEEE Trans. On Biomed. Eng., vol. BME-25, no.6, pp.532-537, Nov. 1978
- Stein R.B., and Olson W.H. : "Selective damage of large diameter peripheral nerve fibres by compression: An application of Laplace's Law, Exp.," Neurology 47:68-80, 1975
- Takeuchi A. : In: Handbook of Physiology, The Nervous System, Kandel E.R. (ed.) Vol 1, pp.39-97, Bethesda, Maryland: American Physiology Society.
- Thompson W.U., Heaton K.W. : "Functional bowel disorders in apparently healthy people," Gastroenterology, 79:283-288, 1980
- Tick L.J. : "Estimation of coherency," in Spectral Analysis of Time Series, B. Harris, Ed. New York:Wiley, pp133-152, 1967
- Tomita T.: "Electrical activity (spikes and slow waves) in gastrointestinal smooth muscle," In: Bulbring E., Brading A.F., Jones A. W. et al. (ed) smooth Muscle: An Assessment of Current Knowledge, Austin, Texas, University of Texas Press, 1981

Van Trees H.L. : Detection, Estimation, and Modulation theory, part I,
New York: Wiley, 1968

Waxman S.G., and Bennett M.V.L.: "Relative conduction velocity of small myelinated and non-myelinated fibres in the central nervous system," J Neurol Sci. 19:357-362, 1973

Waxman S.G. : "Determinants of conduction velocity in myelinated nerve fibres," Muscle & Nerve 3:141-150, 1980

Wilbur B.G. and Kelly K. A.: "Effect of proximal gastric, complete gastric and truncal vagotomy on canine gastric electric activity, motility, and emptying," Ann. Surg. 178, 295-303, 1973

Wilbur W.J. and Rinzel J.: "A theoretical basis for large coefficient of variation and bimodality in neuronal interspike interval distributions," J. Theor. Biol. 105:345-368, 1983

Weiss P. and Hiscoe H.B. : "Experiments on the mechanism of nerve growth," J. Exp. Biol. 107:323-324, 1948

Wood J.D. : "Physiology of the enteric nervous system," In: Physiology of the Gastrointestinal tract. Ed. by L.R. Johnson, Raven Press, New York, P1-37, 1981

Wozencraft J.M. and Jacobs I.M. : Principles of communication Engineering, New York: Wiley, 1965

Yu J.J.L, Reddy S.N., Daniel E.E., Berezin I., Sinha N.K., and Belbeck L., "In-vivo gastroduodenal nerve activities in chronic dogs;" Tenth International Symposium on Gastrointestinal Motility, Rochester, Minnesota, 1985.

APPENDIX A

PROCEDURES FOR THE PREPARATION OF STIMULATING THE CERVICAL VAGAL NERVE

After a 24-hour fast, the dog was anesthetized with 3ml/kg solution of chloralase (2%), Urethane (10%), and subsequently with 70 mg of sodium pentobarbital given intravenously. Incision was made just dorsal the external jugular vein and extended for about 5 cm. Blunt dissection was made throughout the operation to avoid damage to the nerve trunk. After locating the nerve trunk and dissected off the carotid artery, the nerve trunk was lifted up gently with a soft thread. Gauze soaked with paraffin oil was tucked underneath the nerve trunk to provide a isolation. A cuff electrode with appropriate size was slit longitudinally and the nerve trunk was placed carefully inside. The whole cuff was then covered with another paraffin oil soaked gauze. The cuff electrode terminals were then connected to the nerve pulse stimulator. A diagram for the preparation is given Fig A.1.

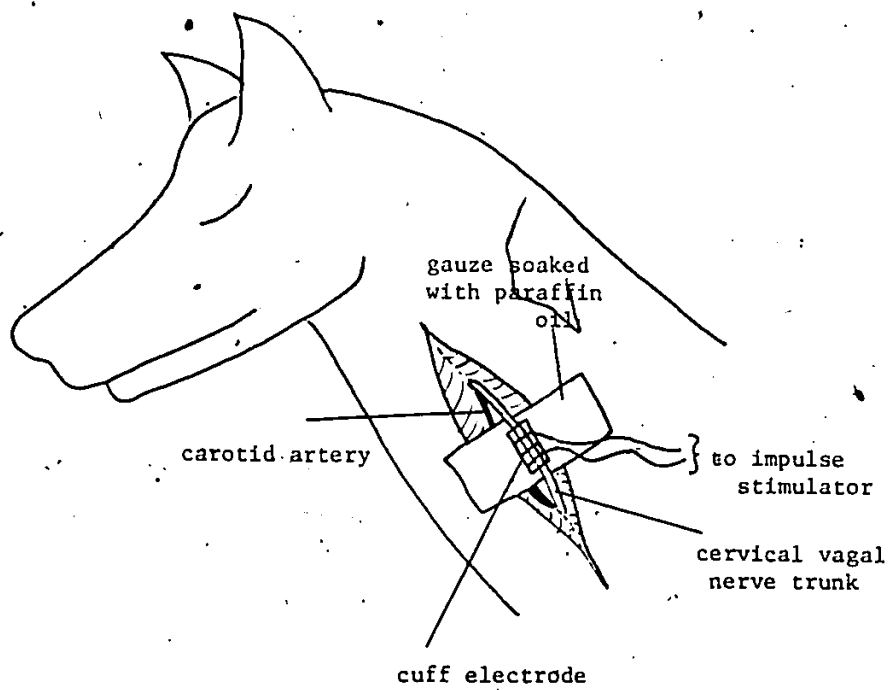
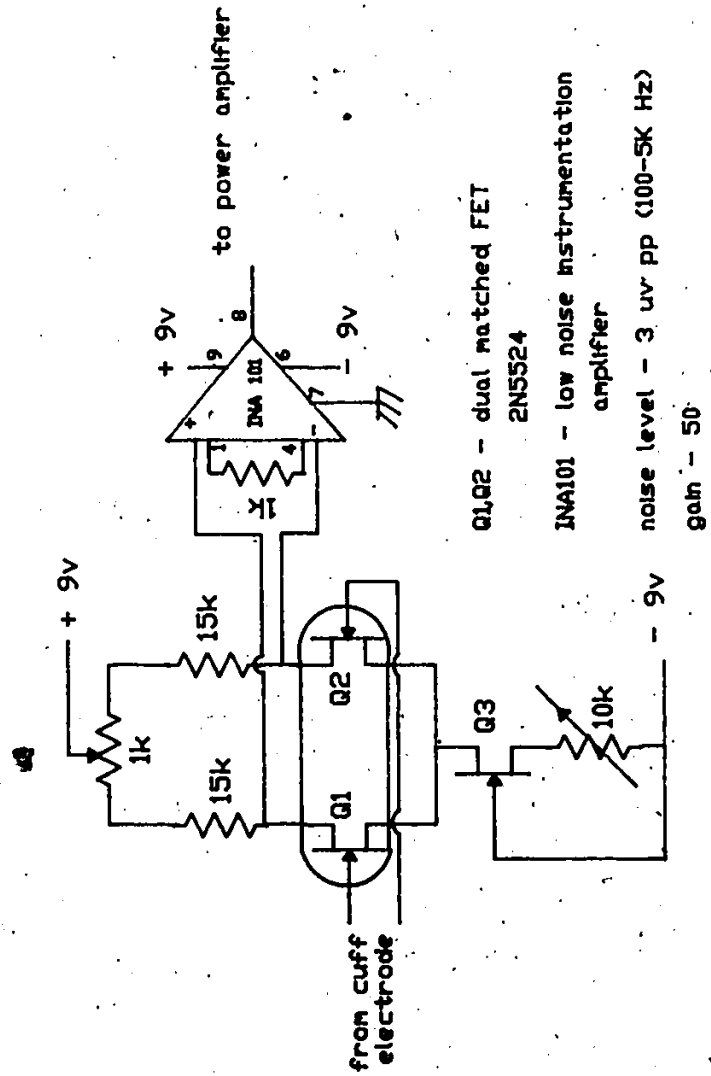
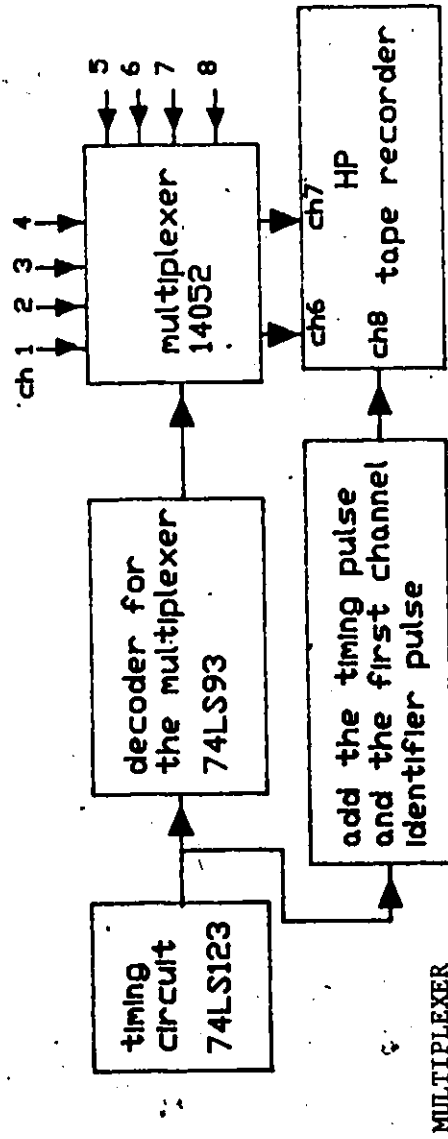


Fig. A.1. Diagram of preparation of stimulating the cervical vagal nerve.



APPENDIX B CIRCUIT DIAGRAM FOR A LOW NOISE PRE-AMPLIFIER



APPENDIX C CIRCUIT DIAGRAM FOR AN ANALOG MULTIPLEXER AND DEMULTIPLEXER

